Imperial College London

Department of Mathematics

Quantum and semiclassical aspects of Lindblad dynamics

Author:
Bradley Longstaff

Supervisor:
Dr Eva-Maria Graefe

Dissertation for the degree of Doctor of Philosophy

February 2020

I certify that this thesis, and the research to which it refers, are the product of my own work, and that any ideas or quotations from the work of other people, published or otherwise, are fully acknowledged in accordance with the standard referencing practices of the discipline.

The copyright of this thesis rests with the author and is made available under a Creative Commons Attribution Non-Commercial No Derivatives licence. Researchers are free to copy, distribute or transmit the thesis on the condition that they attribute it, that they do not use it for commercial purposes and that they do not alter, transform or build upon it. For any reuse or redistribution, researchers must make clear to others the licence terms of this work.

Acknowledgements

First and foremost, I would like to thank my supervisor Eva-Maria Graefe for her invaluable insight, advice and guidance throughout my PhD. I am also grateful to Dorje Brody, with whom I collaborated on the evolution speed of open quantum systems, and to Roman Schubert and Tom Plastow for their collaboration on the semiclassical limit of the Lindblad equation. This project has been supported by an EPSRC Doctoral Training Partnership award, without which this work would not have been possible. Finally, many thanks to my family and partner for their unwavering encouragement and patience.

Abstract

The Lindblad equation is commonly used to model dissipation and decoherence in open quantum systems. Yet many of the properties of Lindblad dynamics are still little understood. This thesis explores various aspects of the Lindblad equation and its connections with non-Hermitian quantum theories. The evolution speed of Lindblad dynamics is investigated and an explicit expression for the speed is derived. The radial component, connected to the rate at which the purity of the state changes, is shown to be determined by the modified skew information of the Lindblad operators. The semiclassical time evolution of Gaussian states under Lindblad dynamics is then considered and a new type of phase-space dynamics is derived for the centre of a Gaussian Wigner function. By viewing the phase-space Lindblad equation as a Schrödinger equation with a non-Hermitian Hamiltonian, a further set of semiclassical equations are derived. These can describe the interference terms in Wigner functions. Further, a PT-symmetric two-level system driven through two consecutive exceptional points at finite speed is considered and an analytical expression for the probability of a non-adiabatic transition is derived. It is shown that the transition through the exceptional points can be experimentally addressed in a PT-symmetric lattice using Bloch oscillations. Finally, a quantum implementation of this PT-symmetric system using ultracold atoms in an optical lattice with single-particle losses is investigated.

Contents

Acknowledgements iv

Abstract vi

List of Figures x

1 Introduction 1
- 1.1 Open quantum systems . . . 2
- 1.2 Lindblad dynamics . . . 4
  - 1.2.1 The Lindblad equation . . . 4
  - 1.2.2 Simulation methods and connections to non-Hermitian Hamiltonians 6
- 1.3 Non-Hermitian Hamiltonians . . . 8
  - 1.3.1 Biorthogonal eigenstates . . . 9
  - 1.3.2 Dynamics . . . 10
  - 1.3.3 Exceptional points . . . 11
  - 1.3.4 PT-symmetry . . . 12
- 1.4 The Bose-Hubbard model . . . 14
- 1.5 Outline . . . 17

2 Evolution speed of Markovian open quantum systems 21
- 2.1 Introduction . . . 21
- 2.2 Generalised Bloch vector . . . 24
- 2.3 Speed of evolution . . . 26
- 2.4 Examples . . . 29
  - 2.4.1 Pure dephasing of a two-level system . . . 29
  - 2.4.2 A dissipative Bose-Einstein condensate . . . 34
- 2.5 Summary . . . 36

3 Lindblad dynamics of Gaussian states in the semiclassical limit 39
- 3.1 Introduction . . . 39
- 3.2 Lindblad equation on phase space . . . 40
- 3.3 Gaussian evolution in the semiclassical limit . . . 42
  - 3.3.1 Deriving semiclassical equations of motion . . . 42
  - 3.3.2 Geometric interpretation of the Lindblad terms . . . 45

3.3.3 Formulation in creation and annihilation operators 48
3.4 Examples and applications 50
3.4.1 Harmonic oscillator with nonlinear damping and amplification . . 50
3.4.2 The dissipative Bose-Hubbard model 52
3.4.3 Ensemble averaged mean-field dynamics 55
3.5 Lindblad dynamics as Schrödinger dynamics with a non-Hermitian Hamiltonian 57
3.6 Summary 65

4 Non-adiabatic transitions through exceptional points in the band structure of a PT-symmetric lattice 67
4.1 Introduction 67
4.2 Adiabatic transitions in a two-mode system 68
4.3 Imperfect time reversal and the Loschmidt echo 72
4.4 Non-adiabatic transitions in a two-mode system 76
4.5 The two-mode model as the Bloch Hamiltonian of a PT-symmetric tight-binding lattice 78
4.6 Summary 90

5 Bloch oscillations in a Bose-Hubbard chain with single-particle losses 91
5.1 Single-particle system 93
5.1.1 State evolution 93
5.1.2 Spectral properties 94
5.1.3 Bloch oscillations of a broad Gaussian state 98
5.2 Mean-field limit of a many-particle system 102
5.2.1 Nonlinear Bloch bands 103
5.2.2 Stability analysis 106
5.2.3 Mean-field and two-particle dynamics 110
5.3 Summary 112

A The quantum jump method 113

B Asymptotic expressions for the Weber function 117

C The single-band tight-binding Hamiltonian 119

Bibliography 123

List of Figures

2.1 The behaviour of the evolution speed v as a function of time is shown here (top left) when the system is initialised in the spin-z up state. The radial v_R (top right) and tangential v_T (bottom left) components are also shown. Results for the decay rates $\gamma = 0.2, 1, 4$, corresponding to the broken, critical and unbroken PT-symmetry phases, are shown in each plot when $g = 1$. The components of the Bloch vector in the broken phase are pictured on the bottom right. Time is measured in units of the period $\tau = \pi/\sqrt{g^2 - \gamma^2}$ with $\gamma = 0.2$. 32

2.2 (Top left) The EP2 boundary in (g, ϵ) parameter space with $\gamma = 1$ fixed. Inside the boundary (yellow) the eigenvalues of the Liouvillian are real, outside this region the eigenvalues are complex. The behaviour of the evolution speed v (top right) is shown for a system initialised in a spin-z up state for three different (g, ϵ) parameter values and $\gamma = 1$. The corresponding radial v_R (bottom left) and tangential v_T (bottom right) components are also shown. 34

2.3 The evolution speed v, together with the radial v_R and tangential v_T components, is shown (top left) for an initial BEC state with the parameters $\theta = \pi/2, \phi = \pi$ and $N = 50$. The purity $\mathrm{Tr}(\hat{\rho}^2)$ of the state and the phase coherence C between the two sites are shown (top right). The Husimi function of the state at $\Omega t \approx 5$ and $\Omega t \approx 10$ is depicted on the bottom left and right, respectively. In each plot time is measured in units of the inverse tunneling rate, $UN = 0.8\Omega$ and $\gamma N = 0.8\Omega$. 37

3.1 Phase-space portraits for the semiclassical dynamics (3.44) with $\omega = 1$, $\gamma_1 = 0.1$, $\gamma_2 = 0.01$, $A = 0.01$ (left) and $A = 0.15$ (right). In the left frame the origin is a stable fixed point. In the right frame there is a stable limit cycle at $|a|^2 = 2.5$, indicated by the blue circle, and the origin is an unstable fixed point. 51

3.2 Comparison of the quantum (top row) and semiclassical (bottom row) dynamics of an initial Glauber coherent state with $\sqrt{2}\,\mathrm{Re}\,a = 4$ and $\sqrt{2}\,\mathrm{Im}\,a = 4$. The harmonic oscillator frequency $\omega = 1$, while the linear damping rate, nonlinear damping rate and amplification rate are $\gamma_1 = 0.1$, $\gamma_2 = 0.01$ and $A = 0.15$ respectively. Times $t = 13$, 50, 150 are shown left to right. 52

3.3 The long-time evolution of the covariance element $\alpha = \langle \hat{a}^\dagger \hat{a} + \hat{a}\hat{a}^\dagger \rangle - 2\langle \hat{a}^\dagger \rangle \langle \hat{a} \rangle$ is plotted on the left. A close up of the dynamics at early times is shown on the right. The quantum dynamics (black) are compared to the semiclassical results (red dashed), with the same initial conditions and parameters as Figure 3.2. 52

3.4 The left hand frame compares the quantum (solid lines) and semiclassical (dashed lines) dynamics of the total particle number (black), as well as the populations of site 1 (blue) and site 2 (red). The quantum (solid line) and semiclassical (dashed line) population imbalance is plotted in the right frame. In both cases the initial average particle number $N_0 = 20$, $UN_0 = 1J$, $\gamma N_0 = 0.8J$, and the initial coherent state parameters are $\alpha_1 = \sqrt{10}e^{i\pi/2}$ and $\alpha_2 = \sqrt{10}$. 54

3.5 The quantum (black) and semiclassical (red dashed) dynamics of the phase coherence C between the two traps, for a closed system (left) and open system with $\gamma N_0 = 0.8J$ (right). In both cases $N_0 = 20$ and $UN_0 = 1J$. The initial coherent state parameters are the same as in Figure 3.4. . . . 55

3.6 Comparison of the quantum (black), ensemble average (red dashed) and mean-field (blue small dashed) population imbalance $S_z = \langle \hat{N}_1 - \hat{N}_2 \rangle / 2$. In both cases $N_0 = 20$, the two-body decay rate $\gamma N_0 = 0.1J$ and the initial coherent state parameters are $\alpha_1 = \sqrt{10}e^{i\pi/2}$ and $\alpha_2 = \sqrt{10}$. In the left frame $UN_0 = 1J$ and on the right $UN_0 = 5J$. 56

3.7 The quantum (top) and semiclassical (bottom) dynamics of an initial cat state in an anharmonic potential with $\beta = 0.1$ and damping at a rate $\gamma = 0.3$. Times $t = 0,\ 0.5,\ 1.5,\ 2.5$ are shown from left to right. 64

3.8 Time evolution of the position (left) and momentum (right) expectation values of the cat state above. The quantum dynamics (black) are compared to the semiclassical results (red dashed). The anharmonic parameter $\beta = 0.1$ and the damping rate $\gamma = 0.3$. 65

4.1 Eigenvalues and overlap of the eigenstates of the model Hamiltonian (4.1). The left panel shows the real (solid black line) and imaginary (dashed red line) parts of the eigenvalues, the right panel shows the overlap of the eigenstates, both in dependence on the coupling strength v for a fixed value of $\gamma = 1$. 70

4.2 Dynamics generated by the Hamiltonian (4.1). v is varied linearly in time as $v = \alpha t$ from $v_i = -5$ to $v_f = 5$ with $\alpha = 0.5$ and $\gamma = 1$. The initial state is one of the instantaneous eigenstates (top) and a randomly selected state (bottom). The left panel shows the population in the two instantaneous eigenstates, the right panel shows the overall norm of the wave function. 71

4.3 (Top left) The Loschmidt echo as a function of the parameter T for the initial state $\psi_i = (0, 1)$, with $\alpha = 2/T$ for each value of T. The remaining frames show the population imbalance p as a function of time for the forwards (black solid) and backwards (red dashed) time evolution with $T = 10$ (top right), $T = 17$ (bottom left) and $T = 30$ (bottom right). In each plot, $\gamma = 1$ in the forwards-time Hamiltonian and $\gamma = 1 + 10^{-14}$ in the backwards-time Hamiltonian. 74

4.4 As in Figure 4.3, with a random initial state ψ_i. The random initial state is the same as in Figure 4.2. 75
4.5 Transmission probability (4.24) as a function of the driving parameter. The left panel shows the variation with γ, the right panel focuses on small driving parameter values for $\gamma = 0.1$. 79
4.6 Top row: Real (left) and imaginary (right) parts of the dispersion relation (4.30) for $\Gamma = 0.2$. The red dashed line depicts the same quantities for the Taylor expansion of the Bloch Hamiltonian (4.29) around $k = \pi/2$. Bottom row: Modulus squared of the components of the eigenstates $\phi_\pm$ associated with $E_\pm(k)$. 81
4.7 Modulus squared of the components of the eigenstates $\phi_\pm$ associated with $E_\pm(k)$ for $\Gamma = 0.8$. 82
4.8 The modulus squared of the k-space representation of a Gaussian beam converges towards the 2π-periodic delta function as the width parameter σ increases. In both plots $q_0 = 0$, $\sigma_1 = \sqrt{0.5}$, $\sigma_2 = \sqrt{20}$ and $\sigma_3 = \sqrt{100}$. On the left $k_0 = 0$ and on the right $k_0 = -0.8\pi$. 82
4.9 Time evolution of the renormalised density $|\psi_j|^2/|\psi|^2$ for an initial Gaussian wave packet in position space such that the two-component function $\Psi(k, 0)$ is approximately a Bloch state (left) and is far from a Bloch state (right). The Gaussian parameters are $x_0 = 10$, $\sigma^2 = 20$, $k_0 = 0$ (left) and $k_0 = 0.3\pi$ (right). In both cases $F = 0.1$, with $\Gamma = 0.2$ (left) and $\Gamma = 0.8$ (right). 84
4.10 Time evolution of the renormalised density for an initial Gaussian wave packet in position space with centre $x_0 = -15$, momentum $k_0 = \pi$ and width $\sigma^2 = 20$, for $\Gamma = 0.2$ and different values of F ($F = 0.02$ top left, $F = 0.1$ top right, and $F = 0.2$ bottom left). The bottom right panel shows the transmission probability for $\Gamma = 0.2$ as a function of F (red). The crosses are numerical values of the transmitted fraction, obtained by evaluating the population in the upper branch of the beam in position space at $t = T/2$, where the Bloch period $T = 2\pi/F$. 87

5.1 Real (left) and imaginary (right) parts of the eigenvalues of the effective Hamiltonian as a function of the decay rate γ for a fixed static tilt $F = 0.3$ (top row) and $F = 1$ (bottom row). 97
5.2 The renormalised density is plotted as a function of time for a single particle initialised on the central lattice site $j = 0$, with a static tilt $F = 0.3$ (top row) and $F = 1$ (bottom row). The unitary dynamics $\gamma = 0$ are plotted in the left column. The dissipative dynamics with $\gamma = 0.2$ and $\gamma = 0.4$ are shown in the middle column of the top and bottom rows respectively. The particle number expectation value dynamics are depicted in the right column for the dissipative cases. 98
5.3 (Top row) Real (left) and imaginary (right) parts of the dispersion relation (5.31) for $\gamma = 0.05$. (Bottom row) The band structure is purely imaginary for $\gamma \geq 2$. On the left $\gamma = 2$ and on the right $\gamma = 10$. 100

5.4 The renormalised number density is plotted as a function of time for an initial Gaussian wave packet in position space with $q_0 = 0$, $k_0 = 0$, $\sigma = \sqrt{20}$ and $F = 0.2$. Results are shown for $\gamma = 0.05$ (left) and γ_j randomly chosen from the interval $(0.025, 0.125)$ (middle). The right frame shows the total particle number dynamics for $\gamma = 0.05$ (black solid) and the randomised decay rates (red dashed). 101

5.5 (Left) Particle number expectation value dynamics for an initial Gaussian wave packet in position space with $q_0 = 0$, $k_0 = 0$ and $\sigma = \sqrt{20}$. Several different values of γ are shown with $F = 0.2$. (Right) The renormalised number density for the case $\gamma = 10$. 101

5.6 Real (left column) and imaginary (right column) parts of the nonlinear Bloch bands for $g = 0$ (top row), $g = 2$ (middle row) and $g = 7$ (bottom row) when $\gamma = 0.1$. 107

5.7 Eigenvalues ω of the stability matrix M corresponding to different stationary states for $\gamma = 0.1$, $g = 2$ (top row) and $g = 7$ (bottom row). The columns show results for different values of the quasimomentum, with $k = 0$ (left), $k = -0.4\pi$ (middle) and $k = -0.8\pi$ (right). 109

5.8 (Top row) The renormalised number density is plotted as a function of time for an initial pure BEC in the lower band (left) and the upper band (middle), with $k = 0$, $x_0 = 0$ and $\sigma = \sqrt{20}$. The right frame shows the total particle number expectation value dynamics for both the initial states (lower band - black; upper band - red dashed). The system parameters are $g = 2$, $\gamma = 0.1$ and $F = 0.2$. (Bottom row) As in the top row, with $g = 7$. 110

5.9 As in Figure 5.8 but for $N = 2$ particles, with $U = 1$ (top row) and $U = 7$ (bottom row). 111

C.1 (Left) The dispersion relation (C.4) with $J = 1$. (Right) Time evolution of the density for an initial broad Gaussian wave packet in position space with $x_0 = 20$, $k_0 = 0$ and $\sigma = \sqrt{50}$. The parameters $J = 1$, $F = 0.1$ and the Bloch period $T = 2\pi/F$. 120

Chapter 1

Introduction

Realistic quantum systems are always coupled to an uncontrollable environment to some degree, which can lead to the destruction of the fragile quantum properties that we would like to harness for application. For instance, the process of decoherence presents a major barrier towards reliable and scalable quantum computing. Recent years have seen a rapid growth of interest in open quantum systems, motivated in part by the drive towards engineering quantum effects into new technologies. While dissipation and decoherence were once viewed solely as unwanted features, the possibilities of engineered environments have opened up new opportunities for the control of quantum systems, such as: dissipative pure state preparation [1]; effecting controlled particle losses from optical lattices [2]; and driving systems towards noiseless subspaces [3].

In standard quantum mechanics the time evolution of the combined system and environment is generated by a Hamiltonian, where the total state evolves unitarily according to the Schrödinger equation. Such a description is typically extremely complicated. However, a complete account of all the environmental degrees of freedom is not necessary, and one can develop approximations by focusing on the dynamics of the reduced state of the system alone. In general, the time evolution of the reduced state of the system is also complicated, due to non-trivial memory effects resulting from interactions between the system and the environment. The situation is greatly simplified if the environment is assumed to be memoryless (a Markovian approximation), in which case the dynamics of the system can be described by an approximate master equation known as the Lindblad

equation [4]. In contrast to the state of the combined system and environment, the time evolution of the reduced state of the system is generally non-unitary. Markovian open quantum systems play an important role in various branches of quantum physics. In particular in the fields of atomic physics and quantum optics, where the physical conditions under which the Lindblad equation is valid are often fulfilled [5].

From a mathematical perspective, the field of open quantum systems is rich and provides a number of new problems and interesting theoretical avenues to explore. For instance, non-Hermitian Hamiltonians appear naturally in models of open quantum systems. In stark contrast to their familiar Hermitian counterparts, non-Hermitian Hamiltonians do not necessarily have real eigenvalues. Moreover, for certain parameter values two or more eigenvalues and their corresponding eigenstates can coalesce. At these so-called exceptional points the Hamiltonian is no longer diagonalisable [6]. On account of their intriguing properties non-Hermitian quantum theories are currently a subject of intensive research, in particular the class of parity-time (PT) symmetric Hamiltonians [7, 8].

In this thesis we shall study various aspects of the Lindblad equation. Many properties that are well understood for unitarily evolving (closed) systems are still to be worked out for Lindblad dynamics. For example, in Chapter 2 we consider the evolution speed of a quantum state evolving under the Lindblad equation. Semiclassical techniques that are invaluable for simulating large dimensional closed systems are yet to be fully generalised to open quantum systems. Chapter 3 presents results that could be used as a basis for developing such methods. Throughout this thesis we shall make connections between the Lindblad equation and non-Hermitian quantum theories. This is perhaps most apparent in Chapter 5, where the Lindblad equation is used to simulate the PT-symmetric system analysed in Chapter 4. The remainder of this introductory chapter presents background material on open quantum systems and concludes with an outline of the thesis.

1.1 Open quantum systems

In this section we present the basics of the formalism of quantum operations in order to introduce the notion of an open quantum system. Throughout this thesis we shall

assume that $\hbar = 1$, except in Chapter 3 when we consider the semiclassical limit of the Lindblad equation.

Quantum operations describe the different physical processes that can be performed on a quantum state $\hat{\rho}$[1] such as dynamics, or measurement and interactions with an environment. Let $\mathcal{H}_S$ denote the Hilbert space of the system of interest and $\mathcal{B}(\mathcal{H}_S)$ be the space of bounded operators acting on $\mathcal{H}_S$. A quantum operation is a map $\mathcal{E} : \mathcal{B}(\mathcal{H}_S) \to \mathcal{B}(\mathcal{H}_S)$ that satisfies the three conditions [9]:

1. $\mathcal{E}$ is trace preserving or decreasing, that is $0 \leq \mathrm{Tr}(\mathcal{E}\hat{\rho}) \leq 1$ for any $\hat{\rho}$.
2. $\mathcal{E}$ is a convex-linear map. For an ensemble of states $\{\hat{\rho}_i\}$ and probabilities $\{p_i\}$ we have that $\mathcal{E}(\sum_i p_i \hat{\rho}_i) = \sum_i p_i \mathcal{E}\hat{\rho}_i$.
3. $\mathcal{E}$ is completely positive. Given an arbitrary second system E with Hilbert space $\mathcal{H}_E$, the map $\mathcal{E} \otimes \mathcal{I}$ takes positive operators on the composite system to positive operators, where $\mathcal{I}$ is the identity map on $\mathcal{B}(\mathcal{H}_E)$.

The probability that the process represented by $\mathcal{E}$ occurs is given by $\mathrm{Tr}(\mathcal{E}\hat{\rho})$. Kraus' theorem [10] states that $\mathcal{E}$ is an operation if and only if it has a representation $\mathcal{E}\hat{\rho} = \sum_j \hat{K}_j \hat{\rho} \hat{K}_j^\dagger$, where the Kraus operators $\hat{K}_j$ satisfy $\hat{I} - \sum_j \hat{K}_j^\dagger \hat{K}_j \geq 0$. A familiar example of a quantum operation is the unitary evolution $\mathcal{E}\hat{\rho} = \hat{U}\hat{\rho}\hat{U}^\dagger$, where $\hat{U}$ is a unitary operator. This is an example of a trace-preserving operation, which are often referred to as completely positive trace-preserving (CPTP) maps.

An open quantum system is a quantum system S that is coupled to an environment E and is thus a subsystem of the total system $\mathcal{H}_S \otimes \mathcal{H}_E$. While the total system evolves unitarily, interactions between the system and environment typically lead to system-environment correlations and prevent a unitary description of the dynamics of S. Following [4] we now show that the evolution of the system S can be described by a CPTP map. Suppose that the initial state of the total system is $\hat{\rho}_{SE}(0)$ and that the state evolves unitarily with $\hat{U}(t,0)$. Then the reduced state of system S at time t is

$$\hat{\rho}_S(t) = \mathrm{Tr}_E \left[\hat{U}(t,0) \hat{\rho}_{SE}(0) \hat{U}^\dagger(t,0) \right], \tag{1.1}$$

[1] A physical quantum state $\hat{\rho}$ is a positive semidefinite operator with unit trace.

where Tr_E denotes the partial trace over the environment. For simplicity it is now assumed that the initial system state is uncorrelated with the environment $\hat{\rho}_{SE}(0) = \hat{\rho}_S(0) \otimes \rho_E$. Making use of the spectral decomposition of the environment state $\hat{\rho}_E = \sum_i \lambda_i |i\rangle\langle i|$, it is straightforward to convert (1.1) into the form

$$\hat{\rho}_S(t) = \sum_{i,j} \hat{K}_{ij}(t)\hat{\rho}_S(0)\hat{K}_{ij}^\dagger(t), \tag{1.2}$$

where the Kraus operators $\hat{K}_{ij}(t) = \sqrt{\lambda_i}\langle j|\hat{U}(t,0)|i\rangle$ act on the Hilbert space $\mathcal{H}_S$; $\{|i\rangle\}$ is an orthonormal basis for $\mathcal{H}_E$; and λ_i are positive real numbers such that $\sum_i \lambda_i = 1$. The Kraus operators satisfy $\sum_{ij} \hat{K}_{ij}^\dagger(t)\hat{K}_{ij}(t) = \hat{I}_S$ and so the evolution of the subsystem is described by a CPTP map. By denoting this map as $V(t)$ (1.2) may be written in the form $\hat{\rho}_S(t) = V(t)\hat{\rho}_S(0)$. The entire time evolution of the open system is described by the one-parameter family of maps $\{V(t) : t \geq 0\}$ and is typically complicated. However, in many applications the family of maps forms a quantum dynamical semigroup [11] and one can obtain a differential equation for the time evolution of the open system.

1.2 Lindblad dynamics

1.2.1 The Lindblad equation

A quantum dynamical semigroup is a family of CPTP maps satisfying the semigroup property $V(t_1)V(t_2) = V(t_1 + t_2)$ for $t_1, t_2 \geq 0$, and $\lim_{t\to 0^+} V(t)\hat{\rho} = \hat{\rho}$ for any state $\hat{\rho}$. It was shown by Lindblad [12], Gorini, Kossakowski and Sudarshan [13] that if the family of maps $\{V(t) : t \geq 0\}$ forms a quantum dynamical semigroup then there exists a linear map $\mathcal{L}$ such that $V(t) = \exp(\mathcal{L}t)$. This leads to the first-order differential equation for the open system

$$\frac{d}{dt}\hat{\rho}_S(t) = \mathcal{L}\hat{\rho}_S(t). \tag{1.3}$$

The map $\mathcal{L}$, often called the Liouvillian, is said to be the generator of the map $V(t)$ and it has the Lindblad form

$$\mathcal{L}\hat{\rho}_S = -i\left[\hat{H}, \hat{\rho}_S\right] + \sum_j \hat{L}_j \hat{\rho}_S \hat{L}_j^\dagger - \frac{1}{2}\hat{L}_j^\dagger \hat{L}_j \hat{\rho}_S - \frac{1}{2}\hat{\rho}_S \hat{L}_j^\dagger \hat{L}_j. \tag{1.4}$$

Here $\hat{H}$ is Hermitian and $\{\hat{L}_j\}$ are arbitrary operators referred to as Lindblad operators, which characterise the interactions between the system and the environment. Note that both the unitary contribution to the dynamics $\hat{H}$ and the Lindblad operators $\{\hat{L}_j\}$ are time independent. Roughly speaking, the Lindblad equation applies when the system is weakly coupled to a Markovian environment. Full details on the physical conditions required of the interaction between the system and the environment can be found in [4] and the review paper [5].

The Lindblad equation (1.4) may also be written in the form

$$\frac{d}{dt}\hat{\rho}_S = -i\left(\hat{H}_{\text{eff}}\hat{\rho}_S - \hat{\rho}_S \hat{H}_{\text{eff}}^\dagger\right) + \sum_j \hat{L}_j \hat{\rho}_S \hat{L}_j^\dagger \tag{1.5}$$

with the non-Hermitian effective Hamiltonian $\hat{H}_{\text{eff}}$ defined as

$$\hat{H}_{\text{eff}} = \hat{H} - \frac{i}{2}\sum_j \hat{L}_j^\dagger \hat{L}_j. \tag{1.6}$$

Thus, the time evolution of the state consists of a non-Hermitian dynamics generated by the effective Hamiltonian $\hat{H}_{\text{eff}}$, together with the so-called jump term $\sum_j \hat{L}_j \hat{\rho}_S \hat{L}_j^\dagger$ that introduces an irreversible component to the dynamics. Together they ensure that $\hat{\rho}_S$ remains a physical state for all time. Due to the presence of the jump term, the Lindblad equation does not necessarily preserve the purity of $\hat{\rho}_S$. Thus, an initial pure state may become mixed and vice versa. From here onwards we shall only be concerned with the dynamics of $\hat{\rho}_S$ and operators acting on $\mathcal{H}_\mathcal{S}$. Therefore, in order to simplify notation, the subscript S on $\hat{\rho}_S$, Tr_S and $\mathcal{H}_S$ will now be dropped.

The eigenvalues and eigenoperators of the Liouvillian $\mathcal{L}$ are obtained by solving the eigenvalue equation $\mathcal{L}\hat{\sigma} = \lambda\hat{\sigma}$. The term 'eigenoperators' is favoured over 'eigenstates' as not all eigenoperators of the Liouvillian correspond to physical quantum states. For

example, it can be the case that $\mathrm{Tr}\,(\hat{\sigma}) < 1$. We first note that the eigenvalues λ always come in complex conjugate pairs. Suppose that $\mathcal{L}\hat{\sigma} = \lambda\hat{\sigma}$, it then follows directly from the definition of $\mathcal{L}$ (1.4) that $\mathcal{L}\hat{\sigma}^\dagger = \bar{\lambda}\hat{\sigma}^\dagger$. Thus, if $\hat{\sigma}$ is an eigenoperator of $\mathcal{L}$ corresponding to the eigenvalue λ, then $\hat{\sigma}^\dagger$ is an eigenoperator of $\mathcal{L}$ corresponding to the eigenvalue $\bar{\lambda}$. It can further be shown [14] that all the eigenvalues satisfy $\mathrm{Re}\lambda \leq 0$ and that there always exists at least one zero eigenvalue $\lambda = 0$.

The eigenoperators that are most often of interest are those with $\lambda = 0$. These operators are referred to as steady states since $\mathcal{L}\hat{\sigma} = 0$, and are said to form a decoherence-free subspace [15], in view of the fact that they are unaffected by the action of the Liouvillian. On the other hand, eigenoperators with $\mathrm{Re}\lambda < 0$ will experience an exponential decay in time, where the decay is purely exponential if $\mathrm{Im}\lambda = 0$ and is superimposed with oscillations if $\mathrm{Im}\lambda \neq 0$. Pure imaginary eigenvalues, referred to as oscillating coherences, are also possible and can lead to non-trivial dynamics, such as initial states that converge to unitarily evolving states (see the appendix of [3] and the references therein for further details). The decoherence-free subspace is dynamically isolated by the Liouvillian gap, $\delta = \max_{\lambda\neq 0} |\mathrm{Re}\lambda|$, which defines a minimum timescale of relaxation of the rest of the system $\tau = 1/\delta$ [16]. If the gap is large, for example, then the states in the decoherence-free subspace quickly become the dominant states dynamically.

1.2.2 Simulation methods and connections to non-Hermitian Hamiltonians

For most problems of interest an analytic solution of the Lindblad equation is out of reach and numerical methods are needed. In this subsection we outline two numerical methods that are used in this thesis to solve the Lindblad equation. The first is the method of 'vec-ing' the quantum state [17], which can be used to directly solve the Lindblad equation provided that the dimension of the Hilbert space is not too large. Consider a finite-dimensional Hilbert space $\mathcal{H}$ of dimension n. The vec-ing process represents the $n \times n$ state matrix ρ as the $n^2 \times 1$ column vector $|\rho\rangle\rangle = (\rho_{1,1}, \ldots, \rho_{1,n}, \ldots, \rho_{n,1}, \ldots, \rho_{n,n})^T$. As

left and right matrix multiplication is equivalent to a multiplication on the vector $|\rho\rangle\!\rangle$,

$$A\rho B \leftrightarrow \left(A \otimes B^T\right) |\rho\rangle\!\rangle, \tag{1.7}$$

the Lindblad equation (1.4) can be converted into the differential equation

$$\frac{d}{dt}|\rho\rangle\!\rangle = K|\rho\rangle\!\rangle. \tag{1.8}$$

Here K is the $n^2 \times n^2$ non-Hermitian matrix

$$K = -i\left(H \otimes I - I \otimes H^T\right) + \sum_j L_j \otimes \bar{L}_j - \frac{1}{2} L_j^\dagger L_j \otimes I - \frac{1}{2} I \otimes \left(L_j^\dagger L_j\right)^T, \tag{1.9}$$

where I is the $n \times n$ identity matrix and the bar on $\bar{L}_j$ denotes complex conjugation. The solution to (1.8) is then given by the matrix exponential

$$|\rho(t)\rangle\!\rangle = \mathrm{e}^{Kt}|\rho(0)\rangle\!\rangle. \tag{1.10}$$

If we define $K = -i\tilde{K}$ equation (1.8) is converted into a Schrödinger equation, with the non-Hermitian matrix $\tilde{K}$ playing the role of the Hamiltonian. In Chapter 3 we start from the phase-space representation of the Lindblad equation and find another way to view the Lindblad equation in terms of a non-Hermitian Hamiltonian.

For low dimensional systems the vec-ing method is a simple way of obtaining numerical solutions to the Lindblad equation. However, for an n-dimensional Hilbert space this requires calculating the matrix exponential of an $n^2 \times n^2$ matrix, which quickly becomes unfeasible for large n. An alternative method, known as the quantum jump or quantum Monte-Carlo wave function method [18–20], allows one to work with $n \times n$ matrices instead, opening up the possibility of simulating higher dimensional systems. Here the Lindblad equation is reformulated as a stochastic average over many pure state trajectories. Each trajectory consists of smooth dynamics generated by the effective Hamiltonian (1.6), interrupted by irreversible transformations due to the jump term. The price to be paid for the reduction in the effective Hilbert space dimension (from n^2 to n) is the need to sample over many realisations. For large n the method is expected to be more efficient

than integrating the Lindblad equation, provided that the number of samples needed for convergence does not increase too strongly with n [4]. Full details of the algorithm are presented in Appendix A.

In this section we have seen two examples of non-Hermitian Hamiltonians arising naturally from the Lindblad equation: in the reformulation of the master equation as a Schrödinger equation with a non-Hermitian Hamiltonian (1.9); and the prominent role of the effective Hamiltonian (1.6) in the quantum jump method. Non-Hermitian quantum theories are the topic of an active research area. In the next section we highlight some properties of non-Hermitian Hamiltonians that will be useful throughout this thesis.

1.3 Non-Hermitian Hamiltonians

In the context of pure state evolution non-Hermitian Hamiltonians have long been used to tackle problems that are difficult to solve within the textbook Hermitian formalism of quantum mechanics and are increasingly used to model open quantum systems [6]. However, models of open quantum systems described by non-Hermitian Hamiltonians generally differ from the view presented in the previous section. For instance, if the pure state $|\psi\rangle$ evolves according to the Schrödinger equation

$$i\frac{d}{dt}|\psi\rangle = \hat{H}|\psi\rangle, \tag{1.11}$$

then in general the state $\hat{\rho} = |\psi\rangle\langle\psi|$ will not remain a bona fide quantum state under the time evolution generated by a non-Hermitian Hamiltonian $\hat{H}$. Nevertheless, their applications are broad and range from optics, where they appear in the study of absorbing or optically active materials [21], to modelling the backaction of quantum measurement on ultracold atoms [22]. Furthermore, the class of non-Hermitian PT-symmetric Hamiltonians, the eigenvalues of which are real or appear in complex conjugate pairs, have been proposed as a generalisation of textbook Hermitian quantum mechanics [23, 24]. New areas of investigation were recently opened up by the realisation of PT-symmetric dynamics in optical experiments [25, 26], stimulating further interest in the field.

1.3.1 Biorthogonal eigenstates

In standard quantum mechanics the Hamiltonian is a Hermitian operator and thus the eigenstates form an orthonormal basis. In contrast, the eigenstates of non-Hermitian operators are generally nonorthogonal. Let $\hat{H}$ be a non-Hermitian Hamiltonian with right $\{|\phi_n\rangle\}$ and left $\{|\chi_n\rangle\}$ eigenstates defined as

$$\hat{H}|\phi_n\rangle = \lambda_n|\phi_n\rangle, \quad \hat{H}^\dagger|\chi_n\rangle = \bar{\lambda}_n|\chi_n\rangle. \tag{1.12}$$

The normalisation convention $\langle\chi_n|\phi_n\rangle = 1$ is adopted, however, with this definition eigenstates are no longer normalised to unity, i.e., $\langle\phi_n|\phi_n\rangle \neq 1$. While the sets $\{|\phi_n\rangle\}$ and $\{|\chi_n\rangle\}$ are generally nonorthogonal, away from degeneracies the left and right eigenstates form a biorthogonal basis with $\langle\chi_n|\phi_m\rangle = \delta_{nm}$ [27]. Furthermore, the set of right eigenstates is complete and, in a finite-dimensional Hilbert space, this implies the completeness of the set of left eigenstates. Given a fixed biorthogonal basis $\{|\phi_n\rangle, |\chi_n\rangle\}$ an arbitrary pure state $|\psi\rangle$ can then be expressed as

$$|\psi\rangle = \sum_n c_n|\phi_n\rangle \tag{1.13}$$

with coefficients $c_n = \langle\chi_n|\psi\rangle$.

It turns out that when one works with biorthogonal bases many of the familiar rules of standard quantum theory, such as the assignment of probabilities to the outcomes of measurements, must be revised [27]. For instance, consider the transition probability between the two states $|\psi\rangle$ and $|\varphi\rangle$. In standard quantum mechanics this is given by

$$p = \frac{\langle\psi|\varphi\rangle\langle\varphi|\psi\rangle}{\langle\psi|\psi\rangle\langle\varphi|\varphi\rangle}. \tag{1.14}$$

However, a consistent probabilistic interpretation of this quantity cannot be maintained when we use the normalisation convention $\langle\chi_n|\phi_n\rangle = 1$. For example, if the system starts in an eigenstate $|\phi_n\rangle$ of the non-Hermitian Hamiltonian $\hat{H}$, there can be no transition into another eigenstate $|\phi_{m\neq n}\rangle$. Yet, due to the nonorthogonality of $\langle\phi_m|\phi_n\rangle$, the conventional

definition of the transition probability (1.14) predicts that there is a non-zero probability for a transition to occur.

This problem can be alleviated by introducing an alternative inner product for biorthogonal systems [27]. However, in this thesis the quantum state is always expanded in an *orthonormal* basis $\{|\phi_n\rangle\}$ (normalised according to $\langle\phi_n|\phi_m\rangle = \delta_{nm}$) and the well-known rules from standard quantum theory can be applied without modification. For instance, the expectation value of the operator $\hat{A}$ in the pure state $|\psi\rangle$ is given by the usual expression

$$\langle\hat{A}\rangle = \frac{\langle\psi|\hat{A}|\psi\rangle}{\langle\psi|\psi\rangle}. \tag{1.15}$$

The term $\langle\psi|\psi\rangle$ in the denominator is important, as the norm of $|\psi\rangle$ is generally not conserved when the Hamiltonian is non-Hermitian.

1.3.2 Dynamics

In complete analogy with standard quantum mechanics the time-independent Schrödinger equation

$$i\frac{d}{dt}|\psi(t)\rangle = \hat{H}|\psi(t)\rangle, \tag{1.16}$$

with non-Hermitian Hamiltonian $\hat{H}$, is formally solved by

$$|\psi(t)\rangle = \hat{U}(t)|\psi(0)\rangle, \tag{1.17}$$

where the time-evolution operator $\hat{U}(t) = \mathrm{e}^{-i\hat{H}t}$ is in general no longer unitary. The time evolution generated by a non-Hermitian Hamiltonian typically does not conserve the norm of the wave function. In order see this, we can write the Hamiltonian in the form $\hat{H} = \hat{h} - i\hat{\Gamma}$ with $\hat{h} = \hat{h}^\dagger$ and $\hat{\Gamma} = \hat{\Gamma}^\dagger$. It then follows from the Schrödinger equation that the norm changes in time according to

$$\frac{d}{dt}\langle\psi(t)|\psi(t)\rangle = -2\langle\psi(t)|\hat{\Gamma}|\psi(t)\rangle. \tag{1.18}$$

Thus, the norm may grow or decay depending on the form of the operator $\hat{\Gamma}$. As an example, consider a pure state $|\psi\rangle$ evolving under the effective Hamiltonian (1.6) appearing

in the Lindblad equation. In this case the norm of the state monotonically decreases in time

$$\frac{d}{dt}\langle\psi(t)|\psi(t)\rangle = -\sum_k \|\hat{L}_k|\psi(t)\rangle\|^2. \tag{1.19}$$

As this time evolution applies to all states, we can conclude that the eigenvalues of $\hat{H}_{\text{eff}}$ must have imaginary parts less than or equal to zero.

1.3.3 Exceptional points

Non-Hermitian Hamiltonians typically have a complex spectrum, with eigenstates that are not necessarily orthogonal. Furthermore, in stark contrast to Hermitian Hamiltonians, the eigenstates of a non-Hermitian Hamiltonian may not even form a basis. This occurs when two or more eigenvalues and the corresponding eigenstates coalesce. At these points, known as exceptional points, the Hamiltonian is no longer diagonalisable and the left and right Jordan chains are needed to form a basis for the Hilbert space [28]. If the eigenvalue λ is d-fold degenerate with only one linearly independent eigenvector $|\phi_0\rangle$, then there exist $d-1$ associated eigenvectors that form the (right) Jordan chain

$$\left(\hat{H}-\lambda\right)|\phi_0\rangle = 0, \quad \left(\hat{H}-\lambda\right)|\phi_j\rangle = |\phi_{j-1}\rangle, \tag{1.20}$$

with $1 \leq j \leq d$. Not unlike the definition of the left eigenstates (1.12), the left Jordan chain is defined as the Jordan chain of $\hat{H}^\dagger$,

$$\left(\hat{H}^\dagger-\bar{\lambda}\right)|\chi_0\rangle = 0, \quad \left(\hat{H}^\dagger-\bar{\lambda}\right)|\chi_j\rangle = |\chi_{j-1}\rangle. \tag{1.21}$$

Although the Hamiltonian cannot be diagonalised at an exceptional point it can be brought into Jordan normal form via a similarity transformation $H = SJS^{-1}$, where H is the matrix representation of $\hat{H}$ and J is block diagonal, with Jordan blocks J_n

corresponding to the eigenvalues λ_n:

$$J_n = \begin{pmatrix} \lambda_n & 1 & 0 & \cdots & 0 \\ 0 & \lambda_n & 1 & \cdots & 0 \\ \vdots & \vdots & \vdots & \ddots & \vdots \\ 0 & 0 & 0 & \cdots & 1 \\ 0 & 0 & 0 & \cdots & \lambda_n \end{pmatrix}. \tag{1.22}$$

Exceptional points have no analogue in Hermitian systems. They have been shown to play an important role in phenomena such as quantum phase transitions and quantum chaos in many-body systems [29]. However, they are yet to be experimentally observed in a genuine quantum system, although several experimental implementations have been proposed [30, 31]. In Chapter 4 we analyse a PT-symmetric system driven directly through a pair of exceptional points and show that this transition can be experimentally addressed in a PT-symmetric lattice using Bloch oscillations.

1.3.4 PT-symmetry

A Hamiltonian $\hat{H}$ is said to be PT-symmetric if it is invariant under the combined action of a parity operator $\mathcal{P}$ and the time-reversal operator $\mathcal{T}$, that is $[\mathcal{PT}, \hat{H}] = 0$ [7]. The time-reversal operator $\mathcal{T}$ maps the complex unit $i \to -i$. Parity $\mathcal{P}$ is a linear operator that squares to the identity operator $\mathcal{P}^2 = \hat{I}$ and commutes with time reversal, $[\mathcal{P}, \mathcal{T}] = 0$ [32]. PT-symmetric Hamiltonians have attracted much attention, both experimentally and theoretically [7, 8], in part due to the remarkable fact that a non-Hermitian Hamiltonian that is PT-symmetric may have real eigenvalues. Indeed, when every eigenstate of $\hat{H}$ is a simultaneous eigenstate of $\mathcal{PT}$ all of the eigenvalues of $\hat{H}$ are real and the PT-symmetry is said to be unbroken. On the other hand, when the eigenstates of $\hat{H}$ and $\mathcal{PT}$ differ, the eigenvalues come in complex conjugate pairs and the PT-symmetry is said to be broken. To see this, suppose that $\hat{H}|\psi\rangle = \lambda|\psi\rangle$, then PT-symmetry $\left[\hat{H}, \mathcal{PT}\right] = 0$ implies that

$$0 = \left[\hat{H}, \mathcal{PT}\right]|\psi\rangle = \hat{H}\mathcal{PT}|\psi\rangle - \bar{\lambda}\mathcal{PT}|\psi\rangle. \tag{1.23}$$

If $|\psi\rangle$ is also an eigenstate of $\mathcal{PT}$ then we immediately see that $\lambda = \bar{\lambda}$. Otherwise, $\mathcal{PT}|\psi\rangle$ is an eigenstate of $\hat{H}$ corresponding to the eigenvalue $\bar{\lambda}$. Because $|\psi\rangle$ is not an eigenstate of $\mathcal{PT}$, the eigenvalue λ must be complex. These complex conjugate eigenvalues have been used to model balanced gain and loss with PT-symmetric Hamiltonians.

PT-symmetric quantum mechanics requires a modification to the axioms of standard quantum theory, viz. the Hamiltonian may be non-Hermitian. Furthermore, experimentally implementing PT-symmetric quantum systems using balanced gain and loss would require a sharply defined energy at a sharply defined time, thus violating Heisenberg's uncertainty principle. In fact, similar conclusions can be drawn for (classical) optical realisations of PT-symmetric systems, owing to the frequency-time uncertainty that results from an application of Fourier analysis and classical electrodynamics [33]. This raises an interesting question: what role, if any, does PT-symmetry play in standard quantum theory when one considers the non-unitary time evolution of open quantum systems? Prosen has explored this to some extent by analysing the symmetries of the Liouvillian [34]. Adopting a different approach, a series of recent articles [35, 36] have sought to understand the significance of PT-symmetry in Markovian open quantum systems by analysing the semiclassical limit. The effective Hamiltonian $\hat{H}_{\text{eff}}$ appearing in the Lindblad equation is another promising place to look for aspects of PT-symmetry. While $\hat{H}_{\text{eff}}$ cannot be PT-symmetric (see the comment under (1.19)) it can have passive PT-symmetry[1] and thus exhibit features of a PT-symmetric system.

The non-Hermitian matrix K (1.9), appearing in the formulation of the Lindblad equation as a Schrödinger equation, provides an interesting example of a PT-symmetric Hamiltonian. Let us define the parity operator $\mathcal{P}$ as

$$\mathcal{P} = \sum_{i=1}^{n} e_i^T \otimes I_n \otimes e_i, \tag{1.24}$$

where I_n is an $n \times n$ identity matrix and e_i is the matrix representation of the i^{th} basis vector. This operator, sometimes referred to as a perfect shuffle, switches the order of

[1] An operator is said have passive PT-symmetry if it can be made PT-symmetric by the addition of a pure imaginary multiple of the identity operator.

the Kronecker product

$$B \otimes A = \mathcal{P}\,(A \otimes B)\,\mathcal{P}. \tag{1.25}$$

If the time-reversal operator $\mathcal{T}$ performs the complex conjugation $i \to -i$ it can readily be checked that $[K, \mathcal{PT}] = 0$, so that K is PT-symmetric. The process of vec-ing the quantum state is closely related to the non-equilibrium formulation of thermo-field dynamics [37, 38]. Therefore, this framework could provide a good starting point to further understand the role of PT-symmetry in Markovian open quantum systems. We leave this problem open for future work.

1.4 The Bose-Hubbard model

Many of the examples in this thesis are models of ultracold atoms in an optical lattice, subject to some form of dissipation described by the Lindblad equation. Therefore, we now introduce a few concepts that will appear throughout this work.

The ability to trap cold atoms, and in particular Bose-Einstein condensates (BECs), in an optical lattice has revolutionised atomic physics and quantum optics. A BEC forms when a gas of bosons is cooled to near absolute zero, so that the ground state occupation becomes macroscopically large [39]. Because all the particles in the BEC are in the ground state, the BEC can be described by a single macroscopic wave function. This characteristic means that a BEC is a highly coherent source of atoms. Owing to the precise experimental control available over both lattice and particles, BECs in optical lattices have great potential for application, such as quantum metrology [40] and quantum information processing [41], as well as foundational tests of quantum mechanics [42]. Furthermore, due to the macroscopic nature of the condensate wave function, cold atoms in optical lattices provide an ideal platform in which to experimentally and theoretically investigate the elusive quantum-classical correspondence.

For low energies the M-mode Bose-Hubbard Hamiltonian

$$\hat{H} = -J \sum_{j=1}^{M-1} (\hat{a}_j^\dagger \hat{a}_{j+1} + \hat{a}_{j+1}^\dagger \hat{a}_j) + \frac{U}{2} \sum_{j=1}^{M} \hat{a}_j^\dagger \hat{a}_j^\dagger \hat{a}_j \hat{a}_j \tag{1.26}$$

describes the unitary dynamics of ultracold atoms in an M-site optical lattice [39]. The $\hat{a}_j$ ($\hat{a}_j^\dagger$) annihilate (create) particles in the ground state of the i^{th} site and satisfy the canonical commutation relations

$$[\hat{a}_j, \hat{a}_k^\dagger] = \delta_{jk}, \quad [\hat{a}_j, \hat{a}_k] = 0; \tag{1.27}$$

J is a positive coupling constant; and U describes pairwise on-site interactions. Here we consider repulsive interactions with $U > 0$. The two-body interaction is valid for cold dilute gases in which s-wave scattering dominates and higher order interactions can be ignored.

In this model a pure BEC is the ground state of the non-interacting ($U = 0$) Bose-Hubbard Hamiltonian,

$$|\Psi(0)\rangle = \frac{1}{\sqrt{N_0!}} \left(\sum_{j=1}^{M} \psi_j \hat{a}_j^\dagger \right)^{N_0} |v\rangle, \tag{1.28}$$

where $|v\rangle$ is the vacuum state, N_0 is the number of particles and the coefficients ψ_j are not necessarily normalised to unity,

$$\sum_{j=-L}^{L} |\psi_j|^2 = \mathcal{N}. \tag{1.29}$$

The many-body state (1.28) is then normalised to $\langle\Psi(0)|\Psi(0)\rangle = \mathcal{N}^{N_0}$. For unitary time evolution it is well known that the mean-field dynamics provide a good approximation, provided that the state remains close to a pure BEC for all time [43].

One way to construct the mean-field approximation is by working with the elements of the single-particle density matrix (SPDM) $\sigma_{ij} = \langle \hat{a}_i^\dagger \hat{a}_j \rangle / N_0$ (see, e.g., [44]). Due to the interaction term, the equations of motion for the SPDM elements do not form a closed system of equations. Rather, they form the so-called Bogoliubov-Born-Green-Kirkwood-Yvon hierarchy. In the mean-field approximation the hierarchy is truncated by approximating the four-point correlation functions as

$$\langle \hat{a}_i^\dagger \hat{a}_j \hat{a}_k^\dagger \hat{a}_l \rangle \approx \langle \hat{a}_i^\dagger \hat{a}_j \rangle \langle \hat{a}_k^\dagger \hat{a}_l \rangle. \tag{1.30}$$

The mean-field evolution of the SPDM elements is then found to be

$$i\dot{\sigma}_{ij} = J\left(\sigma_{i+1j} + \sigma_{i-1j} - \sigma_{ij+1} - \sigma_{ij-1}\right) + g\left(\sigma_{jj} - \sigma_{ii}\right)\sigma_{ij}, \tag{1.31}$$

where $g = UN_0$ is fixed as $N_0 \to \infty$. By identifying $\sigma_{ij} = \bar{\psi}_i\psi_j$ the mean-field equations may equivalently be described by the discrete nonlinear Schrödinger equation

$$i\dot{\psi}_j = -J\left(\psi_{j+1} + \psi_{j-1}\right) + g|\psi_j|^2\psi_j. \tag{1.32}$$

In [44] it has been shown that the same method can be applied to obtain the mean-field dynamics of a dissipative system evolving under the Lindblad equation. However, with this method the mean-field dynamics must be derived on a case-by-case basis for a given set of Lindblad operators $\{\hat{L}_k\}$. In Chapter 3 we derive a general equation of motion for the dissipative mean-field dynamics, valid for arbitrary $\{\hat{L}_k\}$, which has the form of a complex discrete nonlinear Schrödinger equation.

Several different types of Lindblad operator are considered throughout the course of this thesis. We shall discuss them as they are introduced. As an illustration, however, we now briefly examine Lindblad operators of the form $\hat{L}_j = \sqrt{\gamma_j}\hat{a}_j$, which describe localised single-particle losses from lattice site j at a rate γ_j. In particular, let us calculate the time evolution of the total particle number expectation value $\langle\hat{N}\rangle = \sum_j\langle\hat{n}_j\rangle$, where $\hat{n}_j = \hat{a}_j^\dagger\hat{a}_j$ is the particle-number operator on lattice site j. It is straightforward to verify that $\hat{N}$ commutes with the Bose-Hubbard Hamiltonian (1.26). Therefore, only the dissipative part of the Lindblad equation (1.4) contributes to the dynamics,

$$\frac{d}{dt}\langle\hat{N}\rangle = \sum_j \gamma_j\langle\hat{a}_j^\dagger\hat{N}\hat{a}_j - \hat{N}\hat{n}_j\rangle. \tag{1.33}$$

After inserting $\hat{N} = \sum_j \hat{n}_j$, and making use of the commutation relations (1.27), we find that the total particle number decays as

$$\frac{d}{dt}\langle\hat{N}\rangle = -\sum_j \gamma_j\langle\hat{n}_j\rangle. \tag{1.34}$$

Therefore, if the decay rate is the same on each site $\gamma_j = \gamma$ then the total particle number decays exponentially.

Despite their apparent simplicity, Lindblad operators of this form can lead to a range of intriguing effects and may even be used to control many-body quantum systems (see, e.g., [44] and the references therein). In Chapter 5 we demonstrate that ultracold atoms in an optical lattice with single-particle losses from the odd lattice sites can be used to realise a (passive) PT-symmetric quantum system.

1.5 Outline

The outline of the thesis is as follows. We begin with an investigation of the speed of Lindblad evolution. A knowledge of the speed of evolution of the quantum state is crucial for understanding fundamental quantum limits to implementing quantum processes in realistic environments. In Chapter 2 the space of quantum states is embedded in a Euclidean space to deduce the dynamical equation satisfied by the state of an open quantum system evolving under the Lindblad equation. The Euclidean norm is used to obtain an explicit expression for the speed of the evolution of the state. The unitary contribution to the evolution speed is given by the modified skew information of the Hamiltonian, while the radial component of the evolution speed, connected to the rate at which the purity of the state changes, is shown to be determined by the modified skew information of the Lindblad operators. An open-system analogue of the quantum navigation problem is posed and a perturbative analysis is presented to identify the amount of change on the speed. Properties of the evolution speed are examined further through example systems, showing that the evolution speed need not be a decreasing function of time.

In Chapter 3 the semiclassical time evolution of the Wigner function of Gaussian states under Lindblad dynamics is investigated. As we have discussed, typically the Lindblad equation cannot be solved analytically and one must turn to numerical methods. For closed systems there is a large literature on the development of semiclassical approximations that can simulate quantum effects in systems with many degrees of freedom. The

semiclassical time evolution of Gaussian wave packets is at the heart of many of these propagation methods [45–48], including the famous Herman-Kluk propagator [49, 50]. Powerful simulation techniques based on the coherent state semiclassical propagator have been developed alongside these methods [51] and can treat high-dimensional complex problems [52]. However, many of these methods cannot be directly applied to open quantum systems, so that new semiclassical techniques must be developed. Here we derive a new type of phase-space dynamics for the centre of a Gaussian Wigner function, where the Lindblad terms generally introduce a non-Hamiltonian flow. In addition to this, the Gaussian approximation yields dynamical equations for the covariances. By viewing the Wigner function as a wave function on a coordinate space of doubled dimension, and the phase-space Lindblad equation as a Schrödinger equation with a non-Hermitian Hamiltonian, a further set of semiclassical equations are derived. These can describe the interference terms in Wigner functions arising in superpositions of Gaussian states.

In Chapter 4 we analytically derive the probability of a non-adiabatic transition in a two-level system driven through two consecutive exceptional points at finite speed. Exceptional points can lead to surprising physical effects. In particular, the behaviour of a system under parameter variation can differ significantly from the familiar Hermitian case in the presence of exceptional points. In the adiabatic limit an equal redistribution between the states coalescing in the exceptional point is observed, which can be interpreted as a loss of information when passing through the exceptional point. For finite parameter variation this is modified. We demonstrate how the transition through the exceptional points can be experimentally addressed in a PT-symmetric lattice using Bloch oscillations.

In Chapter 5 we investigate Bloch oscillations of ultracold atoms in an optical lattice modelled by the Bose-Hubbard Hamiltonian, with single-particle losses from the odd lattice sites described by the Lindblad equation. For a single particle the time evolution of the state is completely determined by the non-Hermitian effective Hamiltonian $\hat{H}_{\text{eff}}$. This system may, therefore, be viewed as a quantum implementation of the PT-symmetric Hamiltonian discussed in Chapter 4. We analyse the spectral properties of $\hat{H}_{\text{eff}}$ for an infinite lattice and link features of the spectrum to observable dynamical

effects. We then consider the mean-field limit of a many-particle system. Analytic expressions are derived for the generalised nonlinear stationary states and the nonlinear Bloch bands. The interplay of nonlinearity and particle losses leads to peculiar features in the nonlinear Bloch bands, such as the vanishing of solutions and the formation of additional exceptional points. The stability of the stationary states is determined via the Bogoliubov-de Gennes equation and is shown to strongly influence the mean-field dynamics. Remarkably, even far from the mean-field limit, the stability of the nonlinear Bloch bands appears to effect the quantum dynamics. This is demonstrated numerically for a two-particle system.

Chapter 2

Evolution speed of Markovian open quantum systems

2.1 Introduction

Understanding the speed of the evolution of a quantum state is important for a variety of reasons. As well as being of interest in its own right [53, 54], the speed determines the sensitivity of quantum states against time evolution. This information can be used, for example, to determine error bounds on quantum state estimation [55], which is increasingly important in the development quantum information technologies [56]. In the field of quantum information, the evolution speed also determines how fast a given task can be processed, such as implementing quantum algorithms for establishing communication and performing computation. Thus, it is desirable to maximise the speed in various circumstances. The foundational question of how fast a quantum state can evolve (of obtaining quantum speed limits) is also crucial in many applications, from obtaining precision bounds in quantum metrology [57] to enhancing the charging power of quantum batteries [58].

In the case of unitary time evolution, the evolution speed of a pure state in Hilbert space was identified by Anandan and Aharonov as twice the energy uncertainty of the system [59]. In the case of a mixed state, the squared speed v^2 of evolution in Hilbert space is

found to be twice the so-called Wigner-Yanase skew information [60, 61]

$$v^2 = 2\left[\mathrm{Tr}\left(\hat{H}^2\hat{\rho}\right) - \mathrm{Tr}\left(\hat{H}\sqrt{\hat{\rho}}\hat{H}\sqrt{\hat{\rho}}\right)\right] = 2I_\rho, \tag{2.1}$$

where $\hat{\rho}$ is the quantum state and $\hat{H}$ is the Hamiltonian. Wigner and Yanase originally introduced the quantity I_ρ as an a priori measure of the information contained in the state regarding difficult to measure observables, which do not commute with an additive conserved quantity [62]. Research into the evolution speed in the context of quantum-state estimation intensified following the establishment of a connection between the estimation problem and the geometry of the quantum state space [63]. There is now a large body of literature detailing various aspects of the speed of unitary time evolution (see, e.g., [64] and references therein).

Recent years have seen a rapid increase in studies of the evolution speed of open quantum systems (see [65] and the references therein), inspired in part by the desire to understand fundamental quantum limits to implementing quantum processes in more realistic environments. At this point it is worth noting that the notion of speed, which is the ratio of distance and time, crucially depends on the choice of the metric on the space of quantum states. For pure states, there is little ambiguity on account of the existence of a unique unitarily-invariant Fubini-Study metric on the space of pure states [66]. However, for mixed states the structure of the state space is more intricate and there is a range of different metrics one can impose, the merits of which are dependant on the particular application one might consider.

For instance, in [67] the authors consider the parameter sensitivity of the state by examining the Fisher information associated with an open system dynamics. The trace norm of the difference of two density matrices is considered in [68] to define distance, which is used to bound the evolution speed of an open-system dynamics. In [69] the purity of the state is used to define distance and an upper bound for the speed of evolution is obtained. In [70], Uhlmann's fidelity [71, 72] between a pure initial state and the terminal state is taken to define distance to obtain a bound on the evolution speed for general open dynamics. The fidelity-based measure is also considered in [73] where the minimum evolution time for general open-system dynamics is investigated and it is shown that the

closely-related work of [74] does not reproduce their results. This is natural because in [74] the relative purity is used to define distance and hence one does not a priori expect the results to coincide. In [75] the evolution speed of the state under the influence of a non-Hermitian Hamiltonian is worked out.

In this chapter the quantum state $\hat{\rho}$ is viewed as a vector in a Euclidean space and the natural Euclidean metric is taken to define the distance measure[1]. An explicit expression for the evolution speed is worked out for a state evolving via the Lindblad equation and is found to consist of three terms: one associated with the unitary time evolution, given by the modified skew information of the Hamiltonian; a second with the environmental influences generated by Lindblad operators; and a third with the competition between the two. The radial component of the speed is shown to be related to the speed of the change of the purity $\mathrm{Tr}(\hat{\rho}^2)$ of the state. This, in turn, is determined by the modified skew information of the Lindblad operators. We then calculate the changes to the speed induced by a small perturbation of the Hamiltonian when the ambient environmental influences, characterised by the Lindblad operators, cannot be controlled (an analogue of the Zermelo navigation problem [77] for open quantum systems). Quantum control under an open environment is a subject of much recent activity [65, 78] and the navigation problem introduced here offers a new class of problems to explore.

The behaviours of the evolution speed are then studied in example systems. For a two-level system subject to pure dephasing we show that the existence of a PT-symmetric phase transition leads to qualitatively different behaviours of the speed. While in a Bose-Hubbard system coupled to a reservoir we show that the evolution speed need not be decreasing in time, contrary to what other studies have suggested. The results of this chapter have been published in [79].

[1] Various merits in the use of the Euclidean norm are also discussed in the closely related work [76], where the Euclidean norm is used to investigate bounds on the evolution time for general open systems.

2.2 Generalised Bloch vector

We begin by remarking that the space of quantum states $\hat{\rho}$ in a Hilbert space $\mathcal{H}^n$ of dimension n forms a subset of the interior of a sphere S^{n^2-2} in a Euclidean space $\mathbb{R}^{n^2-1}$ [66]. Thus every $\hat{\rho}$ can be thought of as being represented by a vector $\boldsymbol{r} \in \mathbb{R}^{n^2-1}$. There are various ways in which we can choose a system of coordinates for $\mathbb{R}^{n^2-1}$ but here we consider the generalisation of the Bloch vector representation [80]. For this purpose we let $\{\hat{\sigma}_j\}_{j=0,\ldots,n^2-1}$ be an orthonormal basis for the linear space of bounded operators on $\mathcal{H}^n$ equipped with the Hilbert-Schmidt inner product $\langle \hat{\sigma}, \hat{\tau} \rangle = \mathrm{Tr}\left(\hat{\sigma}^\dagger \hat{\tau}\right)$. We set $\hat{\sigma}_0 = n^{-1/2}\mathbb{1}$, hence the operators $\{\hat{\sigma}_j\}_{j=1,\ldots,n^2-1}$ are trace free, and together they satisfy the orthonormality condition $\langle \hat{\sigma}_i, \hat{\sigma}_j \rangle = \delta_{ij}$. For $n = 2$ we may set $\{\hat{\sigma}_j\}_{j=1,\ldots,3}$ to $1/\sqrt{2}$ times the Pauli matrices; for $n = 3$ we may set $\{\hat{\sigma}_j\}_{j=1,\ldots,8}$ to $1/\sqrt{2}$ times the Gell-Mann matrices; and so on. An arbitrary density matrix $\hat{\rho}$ can then be expressed in the form

$$\hat{\rho} = \frac{1}{\sqrt{n}}\,\hat{\sigma}_0 + \sum_{j=1}^{n^2-1} r_j\,\hat{\sigma}_j, \tag{2.2}$$

where $r_j = \mathrm{Tr}(\hat{\rho}\hat{\sigma}_j)$, $j = 1, \ldots, n^2 - 1$, are the components of the vector $\boldsymbol{r} \in \mathbb{R}^{n^2-1}$. For a pure state we have

$$1 = \mathrm{Tr}(\hat{\rho}^2) = \frac{1}{n} + \sum_{j=1}^{n^2-1} r_j^2, \tag{2.3}$$

from which it follows that the squared radius of the sphere S^{n^2-2} in $\mathbb{R}^{n^2-1}$ is given by $1 - n^{-1}$.

We now consider states that evolve via the Lindblad equation

$$\frac{d}{dt}\hat{\rho} = -i[\hat{H}, \hat{\rho}] + \sum_k \hat{L}_k \hat{\rho} \hat{L}_k^\dagger - \frac{1}{2}\left(\hat{L}_k^\dagger \hat{L}_k \hat{\rho} + \hat{\rho}\hat{L}_k^\dagger \hat{L}_k\right). \tag{2.4}$$

Our strategy is to identify the linear differential equation satisfied by the state $\boldsymbol{r}$ that corresponds to the evolution equation (2.4). For this purpose we substitute (2.2) in (2.4)

to obtain

$$\begin{aligned}\sum_{j=1}^{n^2-1}\dot{r}_j\hat{\sigma}_j &= -i\sum_{j=1}^{n^2-1}[\hat{H},\hat{\sigma}_j]r_j+\frac{1}{n}\sum_k[\hat{L}_k,\hat{L}_k^\dagger]\\ &+\sum_{j=1}^{n^2-1}\sum_k\left[\hat{L}_k\hat{\sigma}_j\hat{L}_k^\dagger-\frac{1}{2}\left(\hat{L}_k^\dagger\hat{L}_k\hat{\sigma}_j+\hat{\sigma}_j\hat{L}_k^\dagger\hat{L}_k\right)\right]r_j.\end{aligned}\tag{2.5}$$

We multiply $\hat{\sigma}_i$ to both sides of (2.5) and take the trace, using the orthonormality relation $\langle\hat{\sigma}_i,\hat{\sigma}_j\rangle=\delta_{ij}$ to deduce that r_j satisfies the differential equation

$$\dot{r}_i=\sum_{j=1}^{n^2-1}\Lambda_{ij}r_j+b_i,\tag{2.6}$$

where

$$\Lambda_{ij}=\mathrm{Tr}\left[-i\left[\hat{\sigma}_j,\hat{\sigma}_i\right]\hat{H}+\sum_k\hat{L}_k\hat{\sigma}_j\hat{L}_k^\dagger\hat{\sigma}_i-\frac{1}{2}\sum_k\left(\hat{L}_k^\dagger\hat{L}_k\hat{\sigma}_j\hat{\sigma}_i+\hat{L}_k^\dagger\hat{L}_k\hat{\sigma}_i\hat{\sigma}_j\right)\right]\tag{2.7}$$

is a real matrix and

$$b_i=\frac{1}{n}\sum_k\mathrm{Tr}\left([\hat{L}_k,\hat{L}_k^\dagger]\hat{\sigma}_i\right)\tag{2.8}$$

is a real vector. If the Lindblad operators are normal operators then $b_j=0$. There are also other circumstances in which $\boldsymbol{b}$ vanishes, an example is a system with two Lindblad operators given by $\hat{L}_1=\hat{\sigma}_+$ and $\hat{L}_2=\hat{\sigma}_-$, where $\hat{\sigma}_\pm=\hat{\sigma}_x\pm i\hat{\sigma}_y$.

In Chapter 1 we saw that the right hand side of (2.4) can be written as the action of the Liouvillian $\mathcal{L}$ on $\hat{\rho}$

$$\frac{d}{dt}\hat{\rho}=\mathcal{L}\hat{\rho},\tag{2.9}$$

where $\hat{\rho}$ may be viewed as a vector on which the linear map $\mathcal{L}$ acts. The components $\mathcal{L}_{ij}$ of $\mathcal{L}$ in the basis $\{\hat{\sigma}_j\}$ are given by $\mathcal{L}_{ij}=\langle\hat{\sigma}_i,\mathcal{L}\hat{\sigma}_j\rangle=\mathrm{Tr}\left(\hat{\sigma}_i\mathcal{L}\hat{\sigma}_j\right)$, and we have $(\mathcal{L}\hat{\rho})_j=\sum_i\mathrm{Tr}(\hat{\sigma}_j\mathcal{L}\hat{\sigma}_i)\,\mathrm{Tr}(\hat{\sigma}_i\hat{\rho})$. It follows that $(\mathcal{L}\hat{\rho})_0=0$, because $\mathrm{Tr}(\mathcal{L}\hat{\xi})=0$ for any $\hat{\xi}$.

Therefore, writing

$$\dot{r}_j = \sum_{i=1}^{n^2-1} \mathcal{L}_{ji} r_i + \frac{1}{\sqrt{n}} \mathcal{L}_{j0} \tag{2.10}$$

we deduce from (2.6) that the matrix elements of the Liouvillian are given by $\mathcal{L}_{ji} = \Lambda_{ji}$ for $i, j \neq 0$ and $\mathcal{L}_{j0} = \sqrt{n}\, b_j$. Thus, in the basis $\{\hat{\sigma}_j\}_{j=0,\ldots,n^2-1}$ the Liouvillian takes the block form

$$\mathcal{L} = \left(\begin{array}{c|ccc} 0 & 0 & \cdots & 0 \\ \hline \sqrt{n}\mathbf{b} & & \Lambda & \end{array}\right). \tag{2.11}$$

The eigenvalues of the Liouvillian consist of the zero eigenvalue and the eigenvalues of the matrix Λ. Because the real matrix Λ is not symmetric, its eigenvalues are either real or else come in complex conjugate pairs. The real parts of the eigenvalues are nonpositive due to the fact that $\mathcal{L}$ generates a completely positive map on the quantum state space [14].

2.3 Speed of evolution

Having obtained the dynamical equation satisfied by the state vector $\boldsymbol{r} \in \mathbb{R}^{n^2-1}$ we are now in the position to determine the squared speed of evolution:

$$v^2(t) = \sum_{j=1}^{n^2-1} \dot{r}_j^2 = \mathrm{Tr}\left[(\mathcal{L}\hat{\rho})^2\right]. \tag{2.12}$$

To proceed let us write the time derivative of the state $\hat{\rho}$ in the form $\mathcal{L}\hat{\rho} = -i[\hat{H}, \hat{\rho}] + \mathcal{D}\hat{\rho}$, thus isolating the dissipator term

$$\mathcal{D}\hat{\rho} = \sum_k \hat{L}_k \hat{\rho} \hat{L}_k^\dagger - \frac{1}{2}\left(\hat{L}_k^\dagger \hat{L}_k \hat{\rho} + \hat{\rho} \hat{L}_k^\dagger \hat{L}_k\right) \tag{2.13}$$

from the unitary part of $\mathcal{L}$. Squaring $\mathcal{L}\hat{\rho}$ and taking the trace, we obtain

$$\begin{aligned} v^2(t) &= 2\left[\mathrm{Tr}\left(\hat{H}^2\hat{\rho}^2\right) - \mathrm{Tr}\left(\hat{H}\hat{\rho}\hat{H}\hat{\rho}\right)\right] \\ &\quad -2i\,\mathrm{Tr}\left(\hat{\rho}\left[\mathcal{D}\hat{\rho},\hat{H}\right]\right) + \mathrm{Tr}\left[\left(\mathcal{D}\hat{\rho}\right)^2\right]. \end{aligned} \tag{2.14}$$

There are three terms contributing to the speed of evolution. The first arising purely from the unitary evolution and the third arising purely from the dissipator term. The second term represents in some sense the competition between the Hamiltonian and the Lindblad operators. To see this we note that the cross term in (2.14) can alternatively be written in the form

$$-2i\,\mathrm{Tr}\left(\hat{\rho}\left[\mathcal{D}\hat{\rho},\hat{H}\right]\right) = -2i\sum_k \mathrm{Tr}\left(\hat{\rho}\left[\hat{L}_k\hat{\rho}\hat{L}_k^\dagger,\hat{H}\right]\right) + \frac{1}{2}\mathrm{Tr}\left(\hat{\rho}^2[\hat{H},\hat{L}_k^\dagger\hat{L}_k]\right), \tag{2.15}$$

which vanishes if $\hat{L}_k^\dagger = \hat{L}_k$ and $[\hat{L}_k,\hat{H}] = 0$, thus representing the lack of compatibility between $\hat{H}$ and $\{\hat{L}_k\}$.

The contribution to the squared speed from the unitary evolution (the first term in (2.14)) has recently been identified in [81] as the speed of the evolution of the state, when the distance is measured with respect to the Euclidean angular separation. This term resembles, but is different from, the Wigner-Yanase skew information I_ρ appearing in (2.1). The apparent discrepancy between this result and (2.1) (derived in [60]) is that here we measure the speed with respect to the Euclidean norm in $\mathbb{R}^{n^2-1}$, whereas in [60] the evolution speed of the state is obtained using the Hilbert space norm. The latter is more useful in the context of state estimation because the Fisher-Rao metric for unitary evolution is given by the skew information. However, the analysis of the evolution speed and time using the Euclidean metric is computationally more effective, as it does not involve taking the square root of the density matrix [81]. We shall refer to

$$S(X) = \mathrm{Tr}(\hat{X}^\dagger\hat{X}\hat{\rho}^2) - \mathrm{Tr}(\hat{X}\hat{\rho}\hat{X}^\dagger\hat{\rho}) \tag{2.16}$$

as the 'modified skew information' for the operator $\hat{X}$, which reduces to the variance $\Delta X^2 = \langle\hat{X}^\dagger\hat{X}\rangle - \langle\hat{X}^\dagger\rangle\langle\hat{X}\rangle$ for a pure state.

In contrast to unitary time evolution, in an open system the velocity will generally obtain a radial component so that the purity $\mathrm{Tr}(\hat{\rho}^2)$ changes. To see this, consider the squared magnitude of the radial velocity

$$v_R^2(t) = \frac{(\boldsymbol{r}\cdot\dot{\boldsymbol{r}})^2}{(\boldsymbol{r}\cdot\boldsymbol{r})} = \frac{[\mathrm{Tr}(\hat{\rho}\mathcal{L}\hat{\rho})]^2}{\mathrm{Tr}[(\hat{\rho}-n^{-1}\mathbb{1})^2]}, \tag{2.17}$$

which vanishes for unitary dynamics. In [69] speed limits are derived based on the rate of change of purity of the state and an upper bound for the numerator term $[\mathrm{Tr}(\hat{\rho}\mathcal{L}\hat{\rho})]^2$ is obtained using the Cauchy-Schwarz inequality. In fact, a short calculation shows that

$$v_R(t) = \sum_k \frac{S(L_k)}{\sqrt{\mathrm{Tr}\left[(\hat{\rho}-n^{-1}\mathbb{1})^2\right]}}. \tag{2.18}$$

In other words, we have shown that the speed of the change of the purity is given by twice the modified skew information associated with the Lindblad operators. Thus, the mathematical structure of the speed of purity change is similar to the speed of unitary evolution. This is quite a surprising result because the unitary flow is linear in the Hamiltonian, whereas the dissipative flow is quadratic in the Lindblad operators.

Let us briefly consider the problem of optimisation. Two scenarios that might arise in the context of open quantum systems are: (i) to maximise the speed over all Liouvillians; and (ii) to maximise the speed over all Hamiltonians for a fixed open environment $\{\hat{L}_k\}$. The latter problem arises when an experimentalist has no control over the environmental influences but can set the Hamiltonian so as to implement a rapid state transportation. This corresponds to an open-system analogue of the quantum navigation problem [77]. Under a unitary evolution, the solution to problem (i) is obtained by maximising the modified skew information. For an open system, finding general solutions to these problems is nontrivial. In part because of the competition between $\hat{H}$ and $\{\hat{L}_k\}$, i.e. the second term in (2.14) can a priori be positive or negative. Nevertheless, progress can be made if we note that the right side of (2.14) is just the squared length of the sum vector of the Hamiltonian flow $-i[\hat{H},\hat{\rho}]$ and the Lindblad flow $\mathcal{D}\hat{\rho}$. This implies that, subject to finite energy considerations, the speed is maximised by minimising the angular separation of these two vectors. Alternatively, we can explore a perturbative analysis. Specifically, for problem (ii) we perturb the Hamiltonian $\hat{H}$ in the direction of $\hat{\Delta}$ by a

small amount ϵ, i.e. we let $\hat{H} \to \hat{H} + \epsilon\hat{\Delta}$, and work out how much the speed changes in the limit $\epsilon \to 0$. A calculation shows that this is given by

$$\begin{aligned} \delta v^2 &= 2\left[\mathrm{Tr}\left((\hat{H}\hat{\Delta} + \hat{\Delta}\hat{H})\hat{\rho}^2\right) - 2\mathrm{Tr}\left(\hat{H}\hat{\rho}\hat{\Delta}\hat{\rho}\right)\right] \\ &\quad -2i\sum_k \mathrm{Tr}\left(\hat{\rho}\,[\hat{L}_k\hat{\rho}\hat{L}_k^\dagger, \hat{\Delta}]\right) + \frac{1}{2}\mathrm{Tr}\left(\hat{\rho}^2[\hat{\Delta}, \hat{L}_k^\dagger\hat{L}_k]\right), \end{aligned} \tag{2.19}$$

which can be used, for example, to numerically explore the optimal way to modify the Hamiltonian under uncontrollable environmental influences.

2.4 Examples

2.4.1 Pure dephasing of a two-level system

We now examine the behaviour of the evolution speed via two illustrative examples. For the first example we take the Hamiltonian to be

$$\hat{H} = \frac{1}{2}\epsilon\hat{\sigma}_z + \frac{1}{2}g\hat{\sigma}_x \tag{2.20}$$

and the Lindblad operator to be $\hat{L} = \sqrt{\gamma}\hat{\sigma}_z$, thus describing pure dephasing of the two-level system with a decay rate γ. In the absence of unitary evolution ($\hat{H} = 0$) it is straightforward to check that the time evolution of the Bloch vector is given by

$$r_x(t) = \mathrm{e}^{-2\gamma t}r_x(0), \quad r_y(0) = \mathrm{e}^{-2\gamma t}r_y(0), \quad r_z(t) = r_z(0). \tag{2.21}$$

Thus, the dephasing exponentially reduces the x and y components of the Bloch vector, and the z-axis forms a decoherence-free subspace. Let us now include the Hamiltonian (2.20) and first focus on the special case $g = 0$, which generates rotations of the Bloch vector around the z-axis. In this case

$$\Lambda = \begin{pmatrix} -2\gamma & -\epsilon & 0 \\ \epsilon & -2\gamma & 0 \\ 0 & 0 & 0 \end{pmatrix} \tag{2.22}$$

and the four eigenvalues of the Liouvillian are 0, 0 and $-2\gamma \pm i\epsilon$. Therefore, the PT-symmetry is always broken.

The dynamics of the Bloch vector are readily found to be

$$r_x(t) = \mathrm{e}^{-2\gamma t}\left[\cos\epsilon t\, r_x(0) - \sin\epsilon t\, r_y(0)\right], \tag{2.23}$$

$$r_y(t) = \mathrm{e}^{-2\gamma t}\left[\sin\epsilon t\, r_x(0) + \cos\epsilon t\, r_y(0)\right], \tag{2.24}$$

$$r_z(t) = r_z(0). \tag{2.25}$$

The x and y components perform an exponentially damped harmonic motion in the (x, y)-plane, and once again the z-axis forms a decoherence-free subspace. In this case it is easy to check that

$$v^2(t) = \mathrm{e}^{-4\gamma t}(4\gamma^2 + \epsilon^2)[r_x^2(0) + r_y^2(0)], \tag{2.26}$$

and hence that $v(t)$ decreases exponentially in time. As expected, the speed is zero for the stationary states on the z-axis.

On the other hand, suppose that $\epsilon = 0$ so that the Hamiltonian $\hat{H} = \frac{1}{2}g\hat{\sigma}_x$ no longer commutes with the Lindblad operator $\hat{L} = \sqrt{\gamma}\hat{\sigma}_z$. In this case we have

$$\Lambda = \begin{pmatrix} -2\gamma & 0 & 0 \\ 0 & -2\gamma & -g \\ 0 & g & 0 \end{pmatrix}, \tag{2.27}$$

and the four eigenvalues of the Liouvillian are 0, -2γ, and $-\gamma \pm \sqrt{\gamma^2 - g^2}$. In contrast to the previous case, this model exhibits unbroken as well as broken PT-symmetry in dependence on the parameters. We see that in the region of unbroken PT-symmetry where $g < \gamma$, all the eigenvalues are real; at the exceptional point $g = \gamma$ the PT-symmetry gets broken; and in the symmetry-broken phase where $g > \gamma$ the eigenvalues are either all real or else come in complex conjugate pairs. We expect to observe different behaviours of the system in each of these phases. Indeed, the solutions to (2.6) are given

by

$$r_x(t) = \mathrm{e}^{-2\gamma t} r_x(0), \tag{2.28}$$

$$r_y(t) = \mathrm{e}^{-\gamma t}[(\cos\omega t - (\gamma/\omega)\sin\omega t)\, r_y(0) - (g/\omega)\sin\omega t\, r_z(0)], \tag{2.29}$$

$$r_z(t) = \mathrm{e}^{-\gamma t}[(g/\omega)\sin\omega t\, r_y(0) + (\cos\omega t + (\gamma/\omega)\sin\omega t)\, r_z(0)], \tag{2.30}$$

with $\omega = \sqrt{g^2 - \gamma^2}$. They are oscillatory in the broken phase $g > \gamma$, whereas in the unbroken phase $g < \gamma$ the oscillations associated with the unitary part are completely suppressed. In the literature on the evolution of pure states generated by non-Hermitian Hamiltonians it is conventional to associate the broken phase with large non-unitary contributions. Based on this, one might expect that the broken phase in this example should correspond to $g < \gamma$. The difference here stems from the form of the Lindblad equation $\dot{\hat{\rho}} = \mathcal{L}\hat{\rho}$, which differs from the form of the Schrödinger equation $|\dot{\psi}\rangle = -i\hat{H}|\psi\rangle$ by a factor of $-i$ on the right hand side. That is, $i\mathcal{L}$ takes the role of the 'Hamiltonian' and thus the roles of broken and unbroken PT-symmetry are reversed.

The speed, and the corresponding radial component, are obtained by inserting the solutions (2.28-2.30) into equations (2.12) and (2.18) respectively. From these, the squared magnitude of the tangential component $v_T^2(t) = v^2(t) - v_R^2(t)$ of the velocity can also be determined. The different components of the speed are shown in Figure 2.1 for a system prepared in the spin-z up state $|\psi(0)\rangle = |\uparrow\rangle$. Because this is an eigenstate of $\hat{L}$, we have $v_R(t) = 0$ at $t = 0$. The behaviour of the speed varies between the broken and unbroken PT phases. In the broken phase, the speed exhibits a decay superimposed with oscillations. Here $v_R(t)$ performs periodic oscillations with the period $\tau = \pi/\sqrt{g^2 - \gamma^2}$, where the minima correspond to the times at which the Bloch vector is aligned with the z-axis, i.e. when $\hat{\rho}$ is an eigenstate of the dissipator $\mathcal{D}$. Moving into the unbroken phase, the speed decays rapidly at short times and the oscillation in $v_T(t)$ is completely damped out. However, in this phase the velocity remains nonzero for a longer duration, with a small nonzero radial component remaining once the tangential component has vanished.

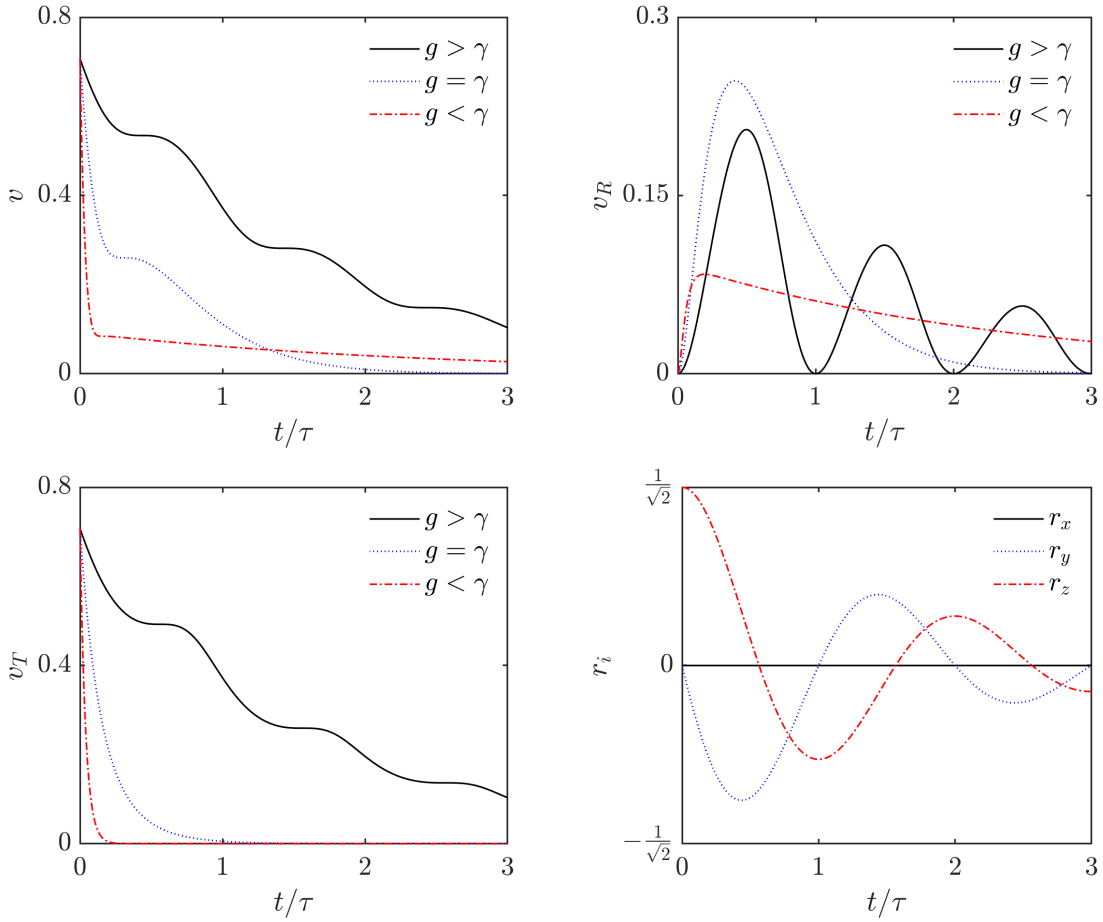


FIGURE 2.1: The behaviour of the evolution speed v as a function of time is shown here (top left) when the system is initialised in the spin-z up state. The radial v_R (top right) and tangential v_T (bottom left) components are also shown. Results for the decay rates $\gamma = 0.2, 1, 4$, corresponding to the broken, critical and unbroken PT-symmetry phases, are shown in each plot when $g = 1$. The components of the Bloch vector in the broken phase are pictured on the bottom right. Time is measured in units of the period $\tau = \pi/\sqrt{g^2 - \gamma^2}$ with $\gamma = 0.2$.

Finally, we consider the situation with parameters $\epsilon \neq 0$ and $g \neq 0$. In this case

$$\Lambda = \begin{pmatrix} -2\gamma & -\epsilon & 0 \\ \epsilon & -2\gamma & -g \\ 0 & g & 0 \end{pmatrix} \tag{2.31}$$

and the eigenvalues of the Liouvillian are obtained from the characteristic polynomial

$$\lambda^4 + 4\gamma\lambda^3 + \left(4\gamma^2 + g^2 + \epsilon^2\right)\lambda^2 + 2\gamma g^2\lambda = 0. \tag{2.32}$$

For fixed γ let us determine the so-called EP2 boundary in (g, ϵ) parameter space, along which two eigenvalues and their corresponding eigenvectors coalesce, corresponding to PT-symmetry breaking. This occurs at solutions of (2.32) that are also extrema [6], that is, solutions of (2.32) and

$$4\lambda^3 + 12\gamma\lambda^2 + 2\left(4\gamma^2 + g^2 + \epsilon^2\right)\lambda + 2\gamma g^2 = 0. \tag{2.33}$$

We see from (2.33) that $\lambda = 0$ is not a possible value at an EP. The conditions (2.32) and (2.33) may thus be written as

$$\lambda^3 + 4\gamma\lambda^2 + \left(4\gamma^2 + g^2 + \epsilon^2\right)\lambda + 2\gamma g^2 = 0, \tag{2.34}$$

$$4\lambda^3 + 12\gamma\lambda^2 + 2\left(4\gamma^2 + g^2 + \epsilon^2\right)\lambda + 2\gamma g^2 = 0. \tag{2.35}$$

Subtracting (2.34) from (2.35) and dividing by λ yields a quadratic for λ, solved by

$$\lambda_\pm = -\frac{4\gamma}{3} \pm \frac{1}{3}\sqrt{4\gamma^2 - 3g^2 - 3\epsilon^2}. \tag{2.36}$$

Inserting the values $\lambda_\pm$ into equation (2.35) defines a function in terms of γ, g and ϵ. With γ fixed, this can be solved to find the EP2 boundary in (g, ϵ) parameter space. A short calculation shows that the condition (2.35) is only satisfied when $4\gamma^2 - 3g^2 - 3\epsilon^2 \geq 0$.

As an example, the EP2 boundary for $\gamma = 1$ is shown in the top left frame of Figure 2.2. The eigenvalues of the Liouvillian are all real for (g, ϵ) values inside the boundary (unbroken PT phase - coloured yellow), whereas outside the boundary (broken PT phase) there are complex eigenvalues that come in complex conjugate pairs. The remaining frames of the same figure depict the different components of the speed for an initial state prepared in a spin-z up state $|\psi(0)\rangle = |\uparrow\rangle$. Each plot shows the dynamics for three different values of the parameters g and ϵ with $\gamma = 1$. Once again a change in the behaviour of the speed is observed as the parameters vary between the broken and unbroken PT phases. The speed v (top right) decays and exhibits oscillations in the broken phase with $(g = 2, \epsilon = 0.2)$. These oscillations are suppressed for the parameter values $(g = 1, \epsilon = 0.2)$ in the unbroken phase. The decay of the speed slows down for parameter values in the broken region where ϵ is the dominant parameter. This can

be seen in Figure 2.2 for the parameter values $(g = 1, \epsilon = 4)$, and is due to the state remaining close to an eigenstate of the dissipator $\mathcal{D}$.

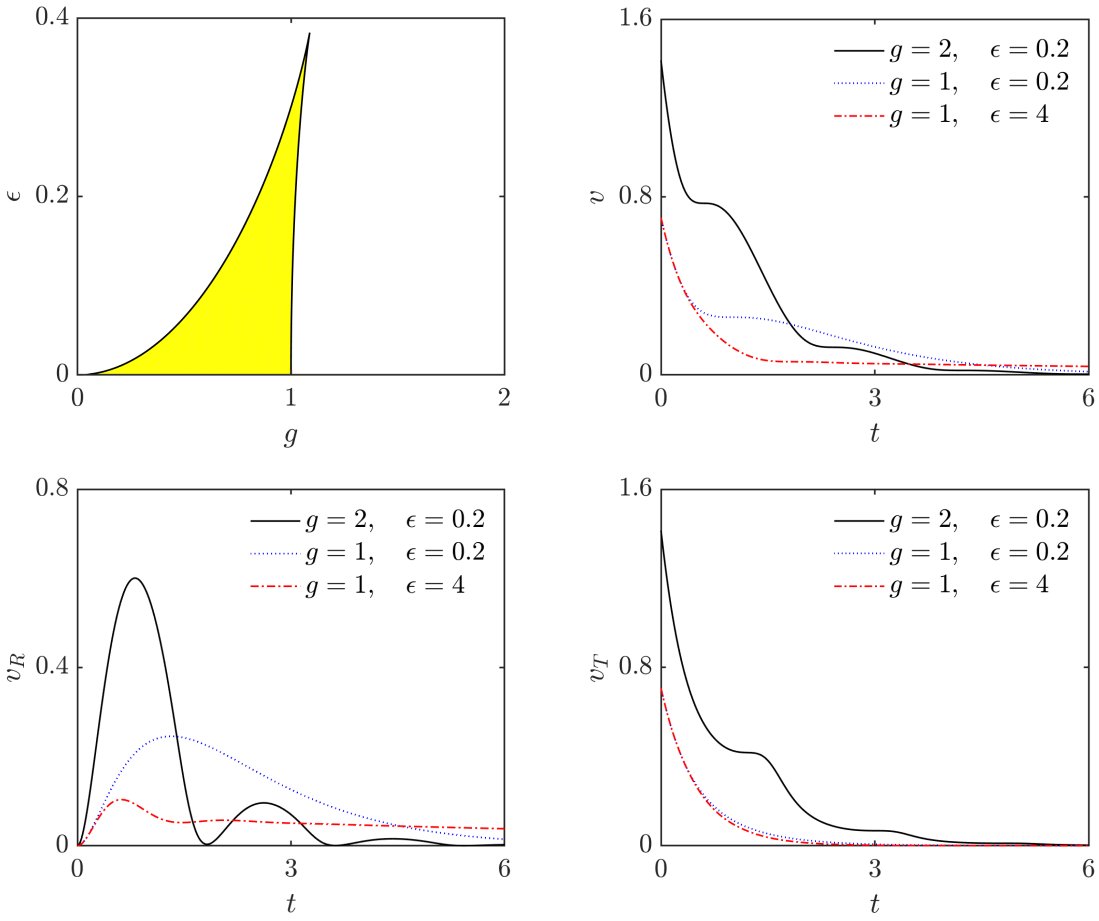


FIGURE 2.2: (Top left) The EP2 boundary in (g, ϵ) parameter space with $\gamma = 1$ fixed. Inside the boundary (yellow) the eigenvalues of the Liouvillian are real, outside this region the eigenvalues are complex. The behaviour of the evolution speed v (top right) is shown for a system initialised in a spin-z up state for three different (g, ϵ) parameter values and $\gamma = 1$. The corresponding radial v_R (bottom left) and tangential v_T (bottom right) components are also shown.

2.4.2 A dissipative Bose-Einstein condensate

In the previous examples the evolution speed is a decreasing function of time. Indeed, in [74] the Cauchy-Schwarz inequality is applied to obtain a bound on the speed of relative purity change. This shows that this speed is decreasing in time and one might conjecture that the evolution speed of the state is also decreasing in time. However, this is not the

case in general. We shall demonstrate this by means of a counterexample based on a driven dissipative Bose-Einstein condensate (BEC) in a two-site optical lattice, previously studied in the context of dissipative state preparation [1].

The unitary dynamics are generated by the two-site Bose-Hubbard Hamiltonian (1.26)

$$\hat{H} = -\Omega(\hat{a}_1^\dagger \hat{a}_2 + \hat{a}_2^\dagger \hat{a}_1) + \frac{U}{2}\left(\hat{a}_1^\dagger \hat{a}_1^\dagger \hat{a}_1 \hat{a}_1 + \hat{a}_2^\dagger \hat{a}_2^\dagger \hat{a}_2 \hat{a}_2\right), \tag{2.37}$$

where we have denoted the coupling constant as Ω to avoid confusion in what follows. In this two-site model it is convenient to introduce the angular momentum operators $\hat{J}_x$, $\hat{J}_y$ and $\hat{J}_z$, according to the Schwinger representation

$$\hat{J}_x = \frac{1}{2}\left(\hat{a}_1^\dagger \hat{a}_2 + \hat{a}_2^\dagger \hat{a}_1\right), \quad \hat{J}_y = \frac{1}{2i}\left(\hat{a}_1^\dagger \hat{a}_2 - \hat{a}_2^\dagger \hat{a}_1\right), \quad \hat{J}_z = \frac{1}{2}\left(\hat{a}_1^\dagger \hat{a}_1 - \hat{a}_2^\dagger \hat{a}_2\right), \tag{2.38}$$

which satisfy the $\mathfrak{su}(2)$ commutation relations

$$[\hat{J}_i, \hat{J}_j] = i\varepsilon_{ijk}\hat{J}_k. \tag{2.39}$$

Up to an overall constant energy shift the Bose-Hubbard Hamiltonian may be written simply as

$$\hat{H} = -\Omega \hat{J}_x + U\hat{J}_z^2. \tag{2.40}$$

Coupling the bosons on the lattice to a reservoir leads to dissipation that can be described by the Lindblad operator $\hat{L} = \sqrt{\gamma}(\hat{J}_z - i\hat{J}_y)$, where γ is a decay rate [1]. As the number operator $\hat{N}$ commutes with each $\hat{J}_i$, the particle number N is conserved and we may thus restrict the analysis to the Hilbert subspace $\mathcal{H}^{N+1}$ of fixed particle number.

Here we calculate the evolution speed of an initial pure BEC state (1.28), represented by the $SU(2)$ coherent state

$$|\theta, \phi\rangle = \exp[i\theta(\hat{J}_x \sin\phi - \hat{J}_y \cos\phi)]|N, 0\rangle, \tag{2.41}$$

where the Fock state $|N, 0\rangle$ corresponds to all N particles in the first lattice site. The result, plotted in Figure 2.3, shows that the speed of evolution can increase. Initially, the Husimi function $Q(\theta, \phi; t) = \langle\theta, \phi|\hat{\rho}(t)|\theta, \phi\rangle$ of the state rapidly delocalises in phase

space (lower left panel) and the speed slows down. However, the distribution then spirals towards the origin (a sink in the semiclassical limit) and, depending on the parameter choice, at the beginning of this localisation the speed can temporarily increase. The speed then decreases towards zero as the state tends towards the steady state.

The initial loss of phase coherence

$$C = \frac{2|\langle \hat{J}_x + i\hat{J}_y \rangle|}{\sqrt{N^2 - 4\langle \hat{J}_z \rangle^2}} \tag{2.42}$$

between the two sites (upper right panel) indicates destruction of the condensate, and the state becomes highly mixed. The revival of the phase coherence can be understood to some extent by expressing the Lindblad operator in terms of creation and annihilation operators, $\hat{L} \propto (\hat{a}_1^\dagger + \hat{a}_2^\dagger)(\hat{a}_1 - \hat{a}_2)$. As discussed in [1], this Lindblad operator attempts to establish a global phase by recycling the anti-symmetric modes into symmetric modes, and, in the noninteracting case, drives the system towards a pure BEC state. The minimum of the phase coherence occurs when the state is most mixed. By writing v_R^2 (2.17) in terms of the purity $p = \mathrm{Tr}(\hat{\rho}^2)$,

$$v_R^2 = \frac{1}{4}\frac{\dot{p}}{p - 1/n}, \tag{2.43}$$

we see that the radial part of the speed v_R is zero when $\dot{p} = 0$. When the state begins to purify under the action of the Lindblad operator v_R increases, before dropping to zero again as the steady state is approached. This explains the behaviour of v_R in the upper left panel.

2.5 Summary

We have derived a closed-form expression for the evolution speed $v(t)$ of a state undergoing Lindblad dynamics and found that it consists of three terms corresponding to the unitary contribution; the Lindblad contribution; and the competition between the two. We also calculated the radial component, connected to the purity change, and found that it is given by the modified skew information for the Lindblad operators. By examining

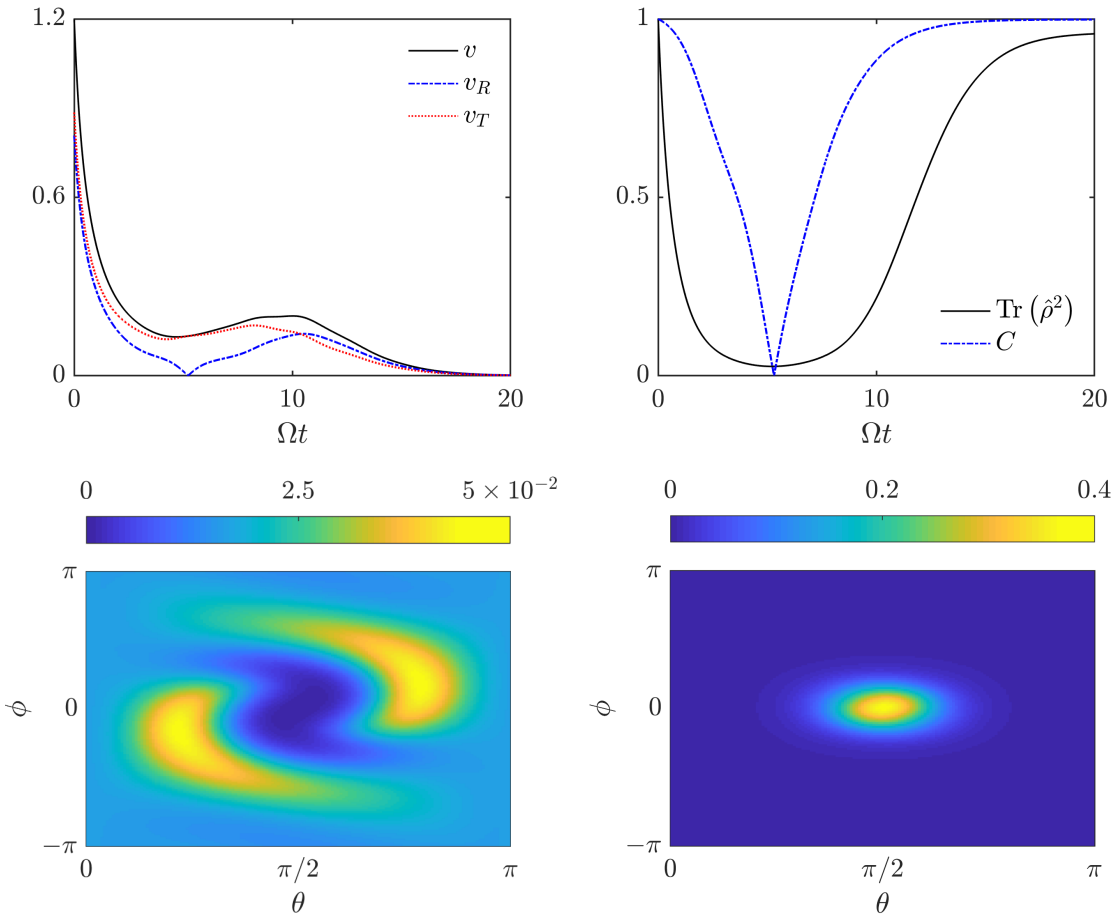


FIGURE 2.3: The evolution speed v, together with the radial v_R and tangential v_T components, is shown (top left) for an initial BEC state with the parameters $\theta = \pi/2, \phi = \pi$ and $N = 50$. The purity $\mathrm{Tr}(\hat{\rho}^2)$ of the state and the phase coherence C between the two sites are shown (top right). The Husimi function of the state at $\Omega t \approx 5$ and $\Omega t \approx 10$ is depicted on the bottom left and right, respectively. In each plot time is measured in units of the inverse tunneling rate, $UN = 0.8\Omega$ and $\gamma N = 0.8\Omega$.

example systems we have shown that the speed of evolution is typically decreasing in time but this need not be the case in general. Our results on the evolution speed open up a new challenge of maximising $v(t)$ over all Liouvillians $\mathcal{L}$, as well as solving the open-system quantum navigation problem.

Chapter 3

Lindblad dynamics of Gaussian states in the semiclassical limit

3.1 Introduction

Since the early days of quantum mechanics, the dynamics of Gaussian wave packets have been considered a natural connection between quantum and classical dynamics [82, 83]. As shown by Heller, Hepp and Littlejohn [84–86], in closed quantum systems the motion of the centre in the semiclassical limit is described by Hamilton's equations of motion. Semiclassical methods based on the time evolution of Gaussian states along classical trajectories provide powerful numerical and analytical tools [46, 87–91].

In this chapter we generalise the approach of Heller and Littlejohn [84, 86] to Lindblad type quantum dynamics. This yields a new type of phase-space dynamics for the position and momentum expectation values, where the Lindblad terms generally introduce non-Hamiltonian flows, which in special cases can take the form of a gradient flow. Furthermore, the semiclassical dynamics provides an approximation of the quantum covariances, which can be useful in various applications. The current study complements previous investigations of the semiclassical limit of Lindblad dynamics, using the framework of path integrals [92], and complex WKB dynamics [93]. In [94] first steps have been made towards applying Heller's wave packet method to Lindblad dynamics for the

case of linear Lindblad operators. There the authors use the framework of chord functions in a doubled phase space. This differs from the approach taken here, which is a more direct application of Heller's method.

This chapter is organised as follows. We first introduce the Lindblad equation on phase space and make a Gaussian ansatz for the state, from which semiclassical equations of motion for the centre and covariance matrix are derived. The resulting semiclassical equations are interpreted and the conditions under which the centre dynamics may be written as a gradient flow are discussed. We then transform our equations of motion to a form that is better suited to many applications, particularly those in quantum optics. Two examples are used to illustrate this. An oscillator with nonlinear losses and amplification, and the dissipative Bose-Hubbard Hamiltonian. Finally, we connect the Lindblad dynamics to non-Hermitian quantum dynamics by viewing the phase-space Lindblad equation as a Schrödinger equation with a non-Hermitian Hamiltonian. The semiclassical limit of the latter has been investigated in detail [95, 96]. Applying results from this context allows us to derive a further set of semiclassical equations for Lindblad dynamics. These can describe the interference terms in Wigner functions arising, for example, in superpositions of Gaussian states. We demonstrate this for a cat state in a damped anharmonic oscillator and conclude with a short summary. Most of the results of this chapter have been published in [97].

3.2 Lindblad equation on phase space

The phase-space representation of quantum mechanics [98] is particularly convenient for analysing the semiclassical limit. In the Wigner-Weyl representation an operator $\hat{f}$ on Hilbert space is mapped to a phase-space function $f(x)$, known as the Weyl symbol of $\hat{f}$, via the Wigner-Weyl transformation

$$f(x) = \int_{\mathbb{R}^n} d\xi \langle q + \frac{\xi}{2} | \hat{f} | q - \frac{\xi}{2} \rangle \mathrm{e}^{-ip\cdot\xi/\hbar}, \tag{3.1}$$

where the canonical coordinates $x = (q, p)$ span the $2n$-dimensional phase space. In this representation the quantum state $\hat{\rho}$ is represented by the Wigner function, which is

defined by the Wigner-Weyl transformation of the operator $\hat{\rho}$ as

$$W(x) = \frac{1}{(2\pi\hbar)^n} \int_{\mathbb{R}^n} d\xi \langle q + \frac{\xi}{2} | \hat{\rho} | q - \frac{\xi}{2} \rangle \mathrm{e}^{-ip\cdot\xi/\hbar}. \tag{3.2}$$

The Weyl symbol of a product of two operators $\hat{f}\hat{g}$ is given by the non-commutative product on phase space $f \star g$, the Moyal product, defined as

$$(f \star g)(x) = f(x) \mathrm{e}^{\frac{i\hbar}{2} \overleftarrow{\nabla} \cdot \Omega \overrightarrow{\nabla}} g(x) = f(x)g(x) + \frac{i\hbar}{2} \{f(x), g(x)\} + \dots . \tag{3.3}$$

Here Ω denotes the symplectic form

$$\Omega = \begin{pmatrix} 0 & I \\ -I & 0 \end{pmatrix}, \tag{3.4}$$

the phase-space gradient is $\nabla := (\partial_q, \partial_p)$ and the arrows over the differential operators in (3.3) indicate whether they act on the function to the left or to the right. The first two terms of the Moyal product are also shown in (3.3), where $\{A, B\} = \nabla A \cdot \Omega \nabla B$ is the usual Poisson bracket.

On the other hand, the Weyl quantisation of a phase-space function $f(x)$ is given by the operator on Hilbert space

$$\hat{f} = \frac{1}{(2\pi\hbar)^{2n}} \int_{\mathbb{R}^{2n}} \int_{\mathbb{R}^{2n}} dx\, dy f(x) \mathrm{e}^{\frac{i}{\hbar} y \cdot (x - \hat{x})}, \tag{3.5}$$

where $\hat{x} = (\hat{q}, \hat{p})$ and $y \in \mathbb{R}^{2n}$. Assuming that the Hamiltonian $\hat{H}$ and the Lindblad operators $\hat{L}_k$ are the Weyl quantisations of sufficiently well-behaved phase-space functions $H(x)$ and $L_k(x)$, the evolution equation for the Wigner function follows immediately from the Lindblad equation (1.4) and is given by

$$i\hbar \partial_t W = H \star W - W \star H + i \sum_k L_k \star W \star \bar{L}_k - \frac{1}{2} \bar{L}_k \star L_k \star W - \frac{1}{2} W \star \bar{L}_k \star L_k. \tag{3.6}$$

Following the work of Heller, Hepp and Littlejohn [84–86] for closed systems, assuming that the initial state is a well-localised Gaussian state, it is justified to approximate the

Hamiltonian and the Lindblad operators by finite Taylor expansions around the centre of the state. We make the ansatz that the time-evolved state remains Gaussian for all times and instantaneously expand the Hamiltonian and the Lindblad operators in Taylor series around the time-dependent centre of the state. For closed quantum systems, in leading orders of $\hbar$ this approximation yields Hamilton's canonical equations of motion for the centre of the state, while the width changes with the linearised classical flow. In what follows we shall investigate how this dynamics generalises in the presence of Lindblad operators.

3.3 Gaussian evolution in the semiclassical limit

3.3.1 Deriving semiclassical equations of motion

The Wigner function of a general Gaussian state is of the form

$$W(x) = \frac{\sqrt{\det G}}{(\pi\hbar)^n} \mathrm{e}^{-(x-X)\cdot G(x-X)/\hbar}, \tag{3.7}$$

where $x = (q, p) \in \mathbb{R}^n \times \mathbb{R}^n$ are canonical phase-space coordinates, X is a vector of the expectation values of the quantum position and momentum operators

$$X_k = \langle \hat{x}_k \rangle \equiv \mathrm{Tr}(\hat{\rho}\hat{x}_k), \tag{3.8}$$

with $\hat{x} = (\hat{q}_1, \ldots, \hat{q}_n, \hat{p}_1, \ldots, \hat{p}_n)$, and G is a real, symmetric and positive definite matrix, encoding the width of the wave packet via the (co)variances of the canonical operators as

$$\hbar \left(G^{-1}\right)_{jk} = \langle \hat{x}_j\hat{x}_k + \hat{x}_k\hat{x}_j \rangle - 2\langle \hat{x}_j \rangle \langle \hat{x}_k \rangle. \tag{3.9}$$

An initial Gaussian state, with time-dependent parameters X and G, remains Gaussian for all times under the quantum dynamics generated by (3.6) if the Hamiltonian is at most quadratic and the Lindblad operators are linear in $\hat{x}$ [94]. We want to show that to leading order in $\hbar$ this remains the case for general Hamiltonians and Lindblad operators.

To do so we must first recall how the semiclassical expansion (3.3) scales with $\hbar$ if we insert a Gaussian (3.7) that is localised in phase space on a scale of $\sqrt{\hbar}$. If we rewrite $W(x) = \hbar^{-n} w_0(\hbar^{-1/2}(x - X))$ with

$$w_0(x) = \frac{\sqrt{\det G}}{\pi^n} \exp(-x \cdot Gx), \tag{3.10}$$

then we find for arbitrary derivatives

$$\partial_x^\alpha W(x) = \hbar^{-|\alpha|/2} \hbar^{-n} w_0^{(\alpha)}(\hbar^{-1/2}(x - X)) \quad \text{with} \quad w_0^{(\alpha)}(y) = \partial_y^\alpha w_0(y) \ . \tag{3.11}$$

Hence, every derivative contributes a factor $1/\sqrt{\hbar}$ and the semiclassical expansion of the Moyal bracket (3.3) effectively becomes an expansion in powers of $\sqrt{\hbar}$ if $g = W$. Furthermore, if we encounter terms of the form $A(x)W(x)$ we can Taylor expand A around $x = X$ and use that for any multi-index β

$$(x - X)^\beta W(x) = \hbar^{|\beta|/2} \hbar^{-n} w_\beta(\hbar^{-1/2}(x - X)) \quad \text{with} \quad w_\beta(y) = y^\beta w_0(y) \ . \tag{3.12}$$

Thus, multiplying by powers of $(x - X)$ reduces the size by powers of $\sqrt{\hbar}$ so that higher order terms in the Taylor expansion contribute to higher orders in semiclassical expansions in powers of $\sqrt{\hbar}$.

We now expand (3.3) in the evolution equation for the Wigner function (3.6) and by (3.11) we need only take the first two terms into account, yielding

$$\begin{aligned} i\hbar \partial_t W = i\hbar \{H, W\} + i\hbar \sum_k \mathrm{Im} \left(L_k \{\bar{L}_k, W\} \right) \\ + \hbar \sum_k \{\bar{L}_k, L_k\} W + \frac{i\hbar^2}{2} \sum_k \mathrm{Re} \left(\{L_k, \{\bar{L}_k, W\}\} \right) + \cdots , \end{aligned} \tag{3.13}$$

where the remaining terms are of order $\hbar^{3/2}$ or higher relative to W. Note that the first two terms on the right-hand side are of order $\sqrt{\hbar}$ whereas the two remaining terms are of order $\hbar$. In the next step we expand H and L_k around the centre X, i.e., in powers of $\delta x := x - X$. By (3.12) we need to expand H and L_k up to second order in the first two terms on the right-hand side, and L_k up to first order in the second two terms in order

to include all terms up to order $\hbar$ in (3.13).

The first two terms on the right-hand side of (3.13) then become

$$2iG\left[\Omega\nabla H + \Omega\sum_k \mathrm{Im}(L_k\nabla\bar{L}_k)\right]\cdot\delta x\, W - 2i\delta x\cdot\Lambda\Omega G\delta x\, W + \cdots \tag{3.14}$$

with

$$\Lambda := H'' + \sum_k \mathrm{Im}\left(L_k\bar{L}_k''\right) + \sum_k \mathrm{Im}\left(\nabla L_k\nabla\bar{L}_k^T\right)\,. \tag{3.15}$$

For the final two terms on the right-hand side of (3.13), we need only expand the Lindblad terms up to first order to obtain

$$\hbar\sum_k\left[\nabla\bar{L}_k\cdot\Omega\nabla L_k + i\nabla L_k\cdot\Omega G\Omega\nabla\bar{L}_k\right]W - 2i\delta x\cdot G\Omega D\Omega G\delta x\, W + \cdots \tag{3.16}$$

where

$$D = \sum_k \mathrm{Re}\left(\nabla L_k\nabla\bar{L}_k^T\right)\,. \tag{3.17}$$

Finally, using

$$i\hbar\partial_t W = \left[\frac{i\hbar}{2}\,\mathrm{Tr}(G^{-1}\dot{G}) + 2iG\dot{X}\cdot\delta x - i\dot{G}\delta x\cdot\delta x\right]W, \tag{3.18}$$

we can separate different powers of δx in (3.13), which leads to the semiclassical equations of motion for the parameters X and G

$$\dot{X} = \Omega\nabla H + \Omega\sum_k \mathrm{Im}\left(L_k\nabla\bar{L}_k\right), \tag{3.19}$$

$$\dot{G} = \Lambda\Omega G - G\Omega\Lambda^T + 2G\Omega D\Omega G. \tag{3.20}$$

To obtain (3.20) the symmetry enforcing convention $G = (G + G^T)/2$ was applied. This is not an approximation and is done purely for cosmetic reasons. As the Wigner function depends only on the symmetric part of G, any antisymmetric part is unobservable. There is a third equation for $\mathrm{Tr}\, G^{-1}\dot{G}$ but this is automatically satisfied if (3.20) holds.

Equations (3.19) and (3.20) are two of the main results of this chapter. As expected, in the unitary case the centre moves according to the classical canonical equations of

motion $\dot{X} = \Omega\nabla H$ and the evolution of G is governed by the linearised Hamiltonian flow around the classical trajectory. The general dynamical equations for the centre of the state can be interpreted as a generalisation of Hamilton's canonical equations to Markovian open quantum systems. Following Littlejohn [86], the terms $\Lambda\Omega G - G\Omega\Lambda^T$ can be interpreted as a linearised flow in the non-unitary case. However, the additional term $2G\Omega D\Omega G$ in (3.20) does not result from the linearised flow. This term originates from the double Poisson brackets in (3.13) and ensures that the Heisenberg uncertainty principle is not violated. In particular, a physically meaningful Gaussian state must fulfil the Robertson-Schrödinger uncertainty relation, expressed in terms of G as [99]

$$G^{-1} + i\Omega \geq 0. \tag{3.21}$$

The extra term $2G\Omega D\Omega G$ is a quantum correction appearing in the semiclassical dynamics, guaranteeing that (3.21) is fulfilled for all times.

The generalisation of Heller's theory to Markovian open systems with *linear* Lindblad operators has previously been considered in [93, 94]. The approach taken therein, however, is quite different from the one presented here. In particular, the authors work with the Fourier transform of the Wigner function, the so-called chord function, in double phase space. While an equivalent of equations (3.19) and (3.20) is implicitly contained in the results presented there, they are not explicitly derived or analysed. Of course, both approaches are exact for quadratic Hamiltonians and linear Lindblad operators, and, as we shall discuss in detail in section 3.5, the equations in [93, 94] can be shown to reduce to a special case of our equations (3.19) and (3.20) for linear Lindblad operators. Apart from going beyond the restriction of linear Lindblad operators, the approach presented here has the advantage of directly yielding the set of dynamical equations (3.19) and (3.20) for the position and momentum expectation values as well as the covariances.

3.3.2 Geometric interpretation of the Lindblad terms

We now analyse the structure of the Lindblad terms in the dynamical equation for the centre (3.19) in more detail. There are two cases for which the geometric interpretation of

these terms is simple. First, for purely Hermitian or anti-Hermitian Lindblad operators the flow generated by the Lindblad terms vanishes, and the only effect in the semiclassical description is on the width of the Wigner function. This is in line with the well-known result that purely Hermitian or anti-Hermitian Lindblad operators lead to decoherence but no dissipation [100].

The second case is when the Weyl symbols of the Lindblad operators are holomorphic functions of $q \pm ip$. In this case, the flow they generate can be written as a gradient flow of the phase-space function $\Gamma := \mp\frac{1}{2}|L|^2$. In fact, the flow generated by a Lindblad operator is the gradient flow of the function $\Gamma = \mp\frac{1}{2}|L|^2$ if and only if the Lindblad symbol is a holomorphic function of either $q + ip$ or $q - ip$. This can be seen as follows. The holomorphy of L as a function of $q \pm ip$ is equivalent to the validity of the Cauchy-Riemann conditions

$$\nabla \operatorname{Re}(L) = \pm\Omega\nabla \operatorname{Im}(L), \tag{3.22}$$

which imply

$$\nabla \operatorname{Im}(L) = \mp\Omega\nabla \operatorname{Re}(L). \tag{3.23}$$

Observing that the Lindblad term on the right hand side of (3.19) may be expressed as

$$\Omega \operatorname{Im}\left(L\nabla\bar{L}\right) = \operatorname{Im}(L)\Omega\nabla \operatorname{Re}(L) - \operatorname{Re}(L)\Omega\nabla \operatorname{Im}(L), \tag{3.24}$$

the right hand side can immediately be identified as

$$\mp\left(\operatorname{Re}(L)\nabla \operatorname{Re}(L) + \operatorname{Im}(L)\nabla \operatorname{Im}(L)\right) = \mp\frac{1}{2}\nabla|L|^2. \tag{3.25}$$

On the other hand, assume we have

$$\operatorname{Im}(L)\Omega\nabla \operatorname{Re}(L) - \operatorname{Re}(L)\Omega\nabla \operatorname{Im}(L) = \mp\frac{1}{2}\nabla|L|^2 = \mp\big(\operatorname{Re}(L)\nabla \operatorname{Re}(L) + \operatorname{Im}(L)\nabla \operatorname{Im}(L)\big) \tag{3.26}$$

and that $L \neq 0$ (as otherwise the Lindblad flow vanishes). Acting with the symplectic onto equation (3.26) gives

$$-\operatorname{Im}(L)\nabla \operatorname{Re}(L) + \operatorname{Re}(L)\nabla \operatorname{Im}(L) = \mp(\operatorname{Re}(L)\Omega\nabla \operatorname{Re}(L) + \operatorname{Im}(L)\Omega\nabla \operatorname{Im}(L)). \tag{3.27}$$

Combining this with the original expression (3.26) yields the Cauchy-Riemann conditions $\nabla \operatorname{Re}(L) = \pm\Omega\nabla \operatorname{Im}(L)$. The gradient dynamics drives trajectories towards the closest maximum of the function Γ. Thus one possible physical interpretation is that Γ is an entropy of the system. Note that similar gradient dynamics have been discussed in the context of thermodynamics, for example by Öttinger and Grmela [101, 102].

Of course, there are operators that are neither Hermitian nor anti-Hermitian, nor have symbols that are holomorphic functions of $q \pm ip$. In some of these cases the Lindblad terms can still be written as gradient flows of more general functions. For instance, Lindblad operators of the form $\hat{L} = a\hat{q} + ib\hat{p}$ with $a \neq \pm b$ result in a semiclassical flow given by the gradient of the function $\Gamma = -\frac{ab}{2}(q^2 + p^2) \neq \mp\frac{1}{2}|L|^2$.

There are other Lindblad operators that instead lead to Hamiltonian flows, such as normal operators in one dimension. In general, however, the Lindblad term leads to a flow which is neither a Hamiltonian nor a gradient flow. Instead of deriving more intricate mathematical conditions for different types of flows, the following two examples aim to develop a better intuition of Lindblad operators that do not generate a Hamiltonian or gradient flow.

As an example, consider a two-dimensional system and a linear Lindblad operator $\hat{L} = \sqrt{\gamma}(\hat{q}_1 + i\hat{p}_2)$. Without a Hamiltonian term the evolution equations for the centre are

$$\dot{q}_1 = 0, \qquad \dot{q}_2 = -\gamma q_1, \qquad \dot{p}_1 = -\gamma p_2, \qquad \dot{p}_2 = 0. \tag{3.28}$$

In this case the semiclassical approximation is exact because L is linear. Both q_1 and p_2 are constants of motion and $p_1(q_2) = \frac{p_2}{q_1}q_2 + \frac{p_1(0)}{q_2(0)}$, i.e., all straight lines are phase-space trajectories and all points in the plane $(0, q_2, p_1, 0)$ in the four-dimensional phase space are fixed points.

A less trivial example is a one-dimensional system with nonlinear Lindblad operator $\hat{L} = \sqrt{\gamma}(\hat{q}^2 + i\hat{p}^2)$. Without a Hamiltonian the semiclassical equations of motion for q, p

are found to be

$$\begin{aligned} \dot{q} &= -2\gamma q^2 p, \\ \dot{p} &= -2\gamma q p^2. \end{aligned} \tag{3.29}$$

The flow conserves the quantity p/q and thus the trajectories are straight lines. The lines $q = 0$ and $p = 0$ are fixed points. In particular the point $p = 0 = q$ acts as a hyperbolic fixed point. Futhermore, the lines $q = p$ and $q = -p$ are the stable and unstable manifolds, respectively. In this example the semiclassical description is of course only an approximation. We shall not dwell on its quantum-classical correspondence here but instead consider more physically relevant examples in detail later.

3.3.3 Formulation in creation and annihilation operators

In many applications, in particular in quantum optics, the Hamiltonian and Lindblad operators are expressed in terms of annihilation and creation operators $\hat{a}_j$ and $\hat{a}_j^\dagger$, satisfying the commutation relations

$$[\hat{a}_i, \hat{a}_j^\dagger] = \delta_{ij}, \quad [\hat{a}_i, \hat{a}_j] = 0. \tag{3.30}$$

For such systems it is convenient to express the semiclassical equations (3.19) and (3.20) in terms of the complex canonical phase-space variables

$$a_j = \frac{1}{\sqrt{2}}(q_j + ip_j), \tag{3.31}$$

where q_j and p_j are the classical counterparts of the quadrature operators, defined as

$$\hat{q}_j = \frac{1}{\sqrt{2}}(\hat{a}_j^\dagger + \hat{a}_j), \quad \hat{p}_j = \frac{i}{\sqrt{2}}(\hat{a}_j^\dagger - \hat{a}_j), \tag{3.32}$$

which are in general not associated to a physical position or momentum. For the remainder of this subsection we choose to work in units of $\hbar = 1$ for simplicity.

The operators $\hat{q}_j, \hat{p}_j$ can be grouped into the vector $\hat{x} = (\hat{q}_1, \ldots, \hat{q}_n, \hat{p}_1, \ldots, \hat{p}_n)$ and the commutation relations between the quadrature operators can then be written in the form

$$[\hat{x}_i, \hat{x}_j] = i\Omega_{ij}, \tag{3.33}$$

where Ω is the symplectic form (3.4). That is, they form a set of canonically conjugate observables. If the Hamiltonian and Lindblad operators are expressed in terms of the $\hat{x}_j$, then the semiclassical Gaussian dynamics derived in the previous section are applicable. The transformation from quadrature operators $\hat{q}, \hat{p}$ to mode operators $\hat{a}, \hat{a}^\dagger$ is achieved via the transformation matrix

$$T = \frac{1}{\sqrt{2}} \begin{pmatrix} I & iI \\ I & -iI \end{pmatrix}. \tag{3.34}$$

Applying the transformations $X_c = TX$ and $G_c = TGT^\dagger$ yields

$$\dot{X}_c = -i\Omega\nabla H + \frac{1}{2}\Omega \sum_k \left(\bar{L}_k \nabla L_k - L_k \nabla \bar{L}_k\right), \tag{3.35}$$

$$\dot{G}_c = G_c\Omega(K - \Gamma) - (\bar{K} + \bar{\Gamma})\Omega G_c + G_c\Omega\Xi\Omega G_c, \tag{3.36}$$

where $X_c = (a, \bar{a})$ and $\nabla := (\partial_a, \partial_{\bar{a}})$. We have also defined K, Γ and Ξ as

$$K = iH'' + \frac{1}{2}\sum_k L_k \bar{L}_k'' - \bar{L}_k L_k'', \tag{3.37}$$

$$\Gamma = \frac{1}{2}\sum_k \left(\nabla L_k \nabla \bar{L}_k^T - \nabla \bar{L}_k \nabla L_k^T\right), \tag{3.38}$$

$$\Xi = \sum_k \left(\nabla L_k \nabla \bar{L}_k^T + \nabla \bar{L}_k \nabla L_k^T\right) \begin{pmatrix} 0 & I \\ I & 0 \end{pmatrix}, \tag{3.39}$$

where primes indicate Hessian matrices. Care must be taken when using these expressions. For instance, the term $\bar{L}_k''$ in (3.37) is the Hessian matrix of $\bar{L}_k$ with respect to $(a, \bar{a})$ and not the complex conjugate of the Hessian L_k''. The same applies to the gradients in (3.38) and (3.39).

In the complex coordinates $(a, \bar{a})$ the covariance matrix $\Sigma = G_c^{-1}$ takes the block form

$$\Sigma = \begin{pmatrix} \bar{\alpha} & \bar{\beta} \\ \beta & \alpha \end{pmatrix}, \tag{3.40}$$

with

$$\alpha_{ij} = \langle \hat{a}_i^\dagger \hat{a}_j + \hat{a}_j \hat{a}_i^\dagger \rangle - 2\langle \hat{a}_i^\dagger \rangle \langle \hat{a}_j \rangle, \tag{3.41}$$

$$\beta_{ij} = \langle \hat{a}_i^\dagger \hat{a}_j^\dagger + \hat{a}_j^\dagger \hat{a}_i^\dagger \rangle - 2\langle \hat{a}_i^\dagger \rangle \langle \hat{a}_j^\dagger \rangle. \tag{3.42}$$

In the commonly used mean-field approximation discussed briefly in Chapter 1 the covariances are zero (1.30). In contrast, our semiclassical method provides an approximation for the covariance elements. Knowledge of the covariances can often be useful in applications, as will be illustrated in the examples below.

3.4 Examples and applications

3.4.1 Harmonic oscillator with nonlinear damping and amplification

As a first example let us consider a harmonic oscillator with nonlinear damping and amplification. The Hamiltonian is given by $\hat{H} = \omega \hat{a}^\dagger \hat{a}$ and the three Lindblad operators

$$\hat{L}_1 = \sqrt{\gamma_1}\hat{a}, \quad \hat{L}_2 = \sqrt{\gamma_2}\hat{a}^2, \quad \hat{L}_3 = \sqrt{A}\hat{a}^\dagger \tag{3.43}$$

describe the damping and gain, where γ_1, γ_2 and A are the linear damping rate, nonlinear damping rate and amplification rate respectively. This model appears in the context of quantum optomechanics and is discussed in [103]. It could describe a driven nanomechanical oscillator coupled to a thermal bath, where the damping rate depends on the excitation of the resonator. Applying (3.35) immediately yields the semiclassical equation

$$\dot{a} = -iwa + \frac{1}{2}(A - \gamma_1)a - \gamma_2 |a|^2 a. \tag{3.44}$$

As discussed in [103] the origin $|a| = 0$ is a stable fixed point provided that $A - \gamma_1 < 0$. However, when the value of A exceeds γ_1 the system exhibits a Hopf bifurcation and the origin becomes unstable. In this case a stable limit cycle occurs and the long-term solution tends towards the curve $|a|^2 = (A - \gamma_1)/2\gamma_2$. Examples of phase-space portraits for both $A < \gamma_1$ and $A > \gamma_1$ are depicted in Figure 3.1, and the semiclassical and quantum dynamics are compared in Figure 3.2 for the case $A > \gamma_1$. Due to the weak nonlinear damping, a good correspondence is observed for short to medium times. Over longer times the centre of the semiclassical Gaussian becomes trapped on the limit cycle and the width grows. On the other hand, in accordance with the semiclassical flow (right frame of Figure 3.1), the quantum Wigner function begins to smear out over the limit cycle into a donut shape.

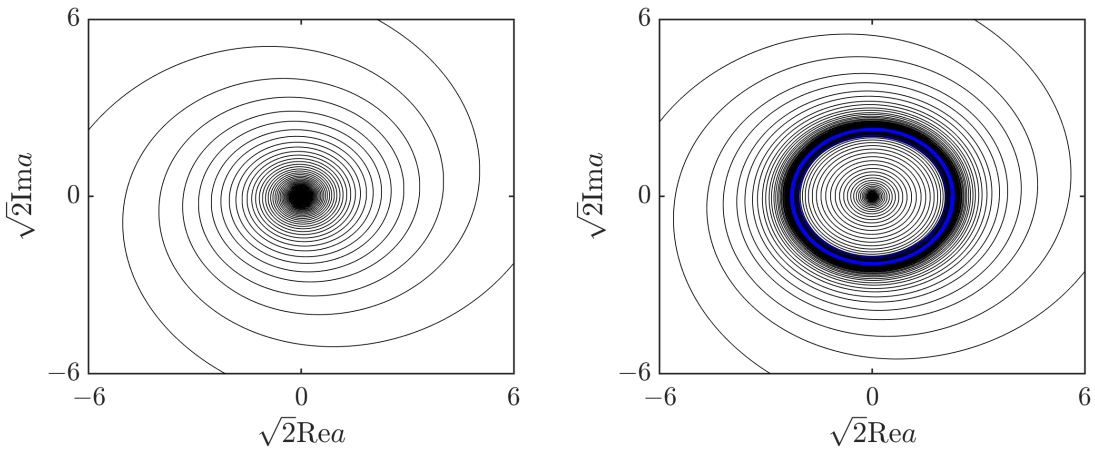


FIGURE 3.1: Phase-space portraits for the semiclassical dynamics (3.44) with $\omega = 1$, $\gamma_1 = 0.1$, $\gamma_2 = 0.01$, $A = 0.01$ (left) and $A = 0.15$ (right). In the left frame the origin is a stable fixed point. In the right frame there is a stable limit cycle at $|a|^2 = 2.5$, indicated by the blue circle, and the origin is an unstable fixed point.

In Figure 3.3 we additionally examine the time evolution of the covariance element α, where α is defined in (3.41). As expected, in the short time limit there is a good agreement with the quantum dynamics. Over a longer time the Gaussian continues to spread out, resulting in a growing value of α. This is in contrast to the quantum value of α, which eventually plateaus. This feature appears to stem from the quantum Wigner function smearing out over the limit cycle. In order to describe the spread of the Wigner function over a limit cycle in a semiclassical framework we would have to adapt the methods and results from [104] to open systems.

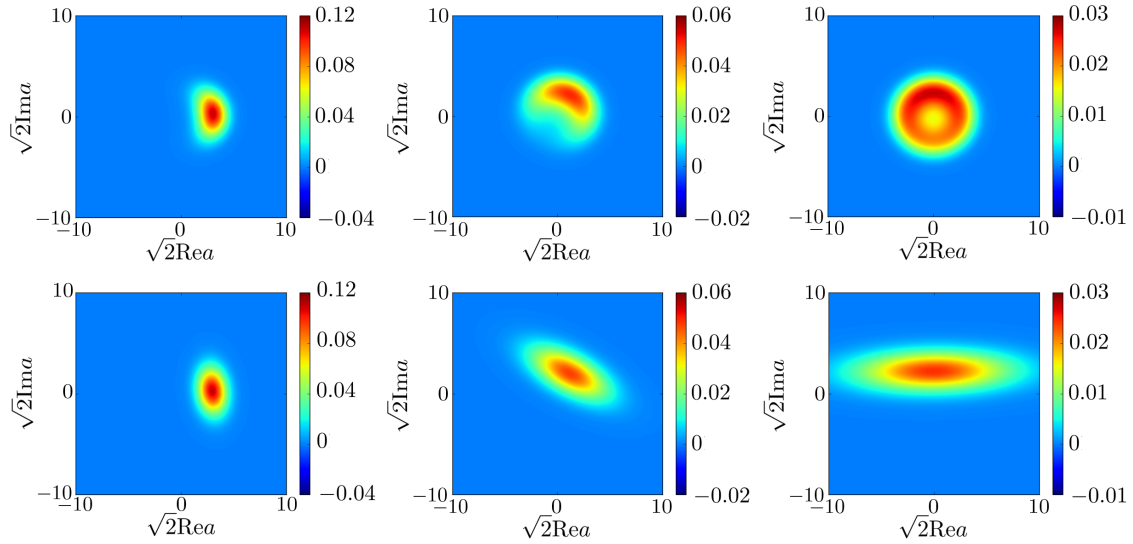


FIGURE 3.2: Comparison of the quantum (top row) and semiclassical (bottom row) dynamics of an initial Glauber coherent state with $\sqrt{2}\,\mathrm{Re}\;a = 4$ and $\sqrt{2}\,\mathrm{Im}\;a = 4$. The harmonic oscillator frequency $\omega = 1$, while the linear damping rate, nonlinear damping rate and amplification rate are $\gamma_1 = 0.1$, $\gamma_2 = 0.01$ and $A = 0.15$ respectively. Times $t = 13$, 50, 150 are shown left to right.

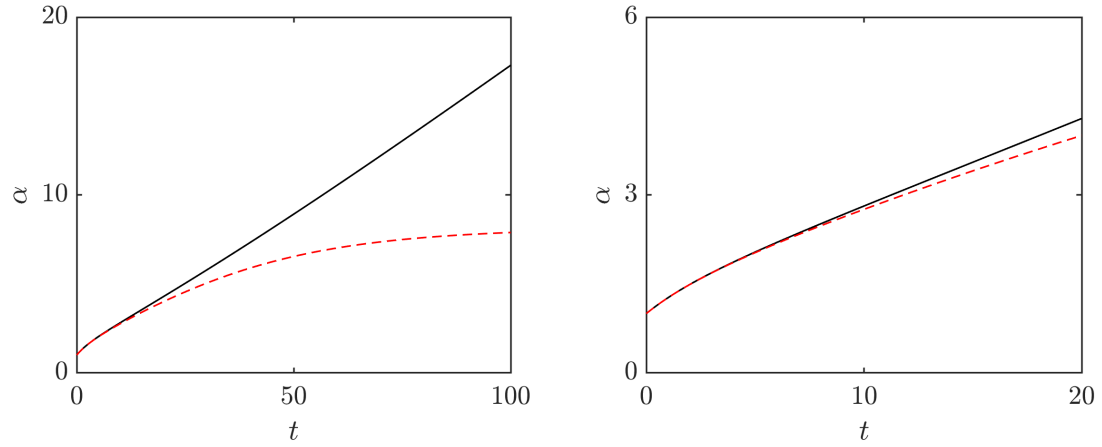


FIGURE 3.3: The long-time evolution of the covariance element $\alpha = \langle \hat{a}^\dagger \hat{a} + \hat{a}\hat{a}^\dagger \rangle - 2\langle \hat{a}^\dagger \rangle \langle \hat{a} \rangle$ is plotted on the left. A close up of the dynamics at early times is shown on the right. The quantum dynamics (black) are compared to the semiclassical results (red dashed), with the same initial conditions and parameters as Figure 3.2.

3.4.2 The dissipative Bose-Hubbard model

As a second application let us consider the description of cold atoms in optical lattices subject to dissipation and/or decoherence. The Hamiltonian is the Bose-Hubbard Hamiltonian (1.26) and the set of Lindblad operators $\{\hat{L}_k\}$ are arbitrary functions of the

operators $\hat{a}_i$ and $\hat{a}_i^\dagger$. In the semiclassical limit a pure BEC (1.28) in an optical lattice can be approximated as a product state of Glauber coherent states

$$|\Psi\rangle = \bigotimes_i |\alpha_i\rangle, \tag{3.45}$$

which we take as our initial state. The on-site Glauber coherent state $|\alpha_i\rangle$ is defined as an eigenstate of the annihilation operator $\hat{a}_i$, where the complex eigenvalue α_i describes the amplitude and phase of the coherent matter-wave field. This corresponds to a Poissonian atom number distribution on each site with average $\bar{n}_i = |\alpha_i|^2$. Thus, the atom number at each site is uncertain.

The celebrated mean-field description of BECs in optical lattices can be derived using a Gaussian approximation. In fact, this goes beyond the mean-field description as it also provides an approximation for correlation functions. While the mean-field dynamics for cold atoms in optical lattices for specific Lindblad operators have previously been derived in the literature by neglecting quantum fluctuations in the equations of motion for particular observables, the Gaussian approximation introduced here yields a canonical form of the mean-field dynamics for arbitrary Lindblad operators. We shall now provide these equations of motion for the general case, before briefly discussing the resulting dynamics for an example system.

The Weyl symbol of the Bose-Hubbard Hamiltonian (1.26) is given by

$$H = -J \sum_{j=1}^{M-1} (\bar{a}_j a_{j+1} + \bar{a}_{j+1} a_j) + \frac{U}{2} \sum_{j=1}^{M} \left(|a_j|^4 - 2|a_j|^2 + \frac{1}{2} \right). \tag{3.46}$$

Inserting the Hamiltonian above into (3.35) yields the Gross-Pitaevskii equation describing the Hamiltonian dynamics together with additional terms describing the effects of the Lindblad operators

$$\dot{a}_j = iJ(a_{j+1} + a_{j-1}) - iU(|a_j|^2 - 1)a_j + \frac{1}{2} \sum_k \left(\bar{L}_k \frac{\partial L_k}{\partial \bar{a}_j} - L_k \frac{\partial \bar{L}_k}{\partial \bar{a}_j} \right). \tag{3.47}$$

Thus, the usual mean-field result is recovered, together with the effect of any Lindblad operator that is a function of $\hat{a}$ and $\hat{a}^\dagger$. Furthermore, the equation of motion for G_c

provides short-time approximations for quantities depending on the covariance matrix elements. For instance, the phase coherence of the state is characterised by the first-order correlation function

$$g_{ij}^{(1)} = \frac{|\langle \hat{a}_i^\dagger \hat{a}_j \rangle|}{\sqrt{\langle \hat{a}_i^\dagger \hat{a}_i \rangle \langle \hat{a}_j^\dagger \hat{a}_j \rangle}}. \tag{3.48}$$

As a specific example let us consider a two-mode system with two-body losses due to inelastic scattering, which can be modelled by applying the nonlinear Lindblad operators $\hat{L}_j = \sqrt{\gamma}\hat{a}_j^2$ to each lattice site [5, 44]. In this case (3.47) leads to the equations of motion

$$\dot{a}_1 = iJa_2 - iU\left(|a_1|^2 - 1\right)a_1 - \gamma|a_1|^2 a_1, \tag{3.49}$$

$$\dot{a}_2 = iJa_1 - iU\left(|a_2|^2 - 1\right)a_2 - \gamma|a_2|^2 a_2. \tag{3.50}$$

The solution of these equations provides a good first order approximation to the total population $N(t) = |a_1(t)|^2 + |a_2(t)|^2$ and the population imbalance $2S_z(t) = |a_1(t)|^2 - |a_2(t)|^2$. Figure 3.4 illustrates this using an example with relatively small loss rate.

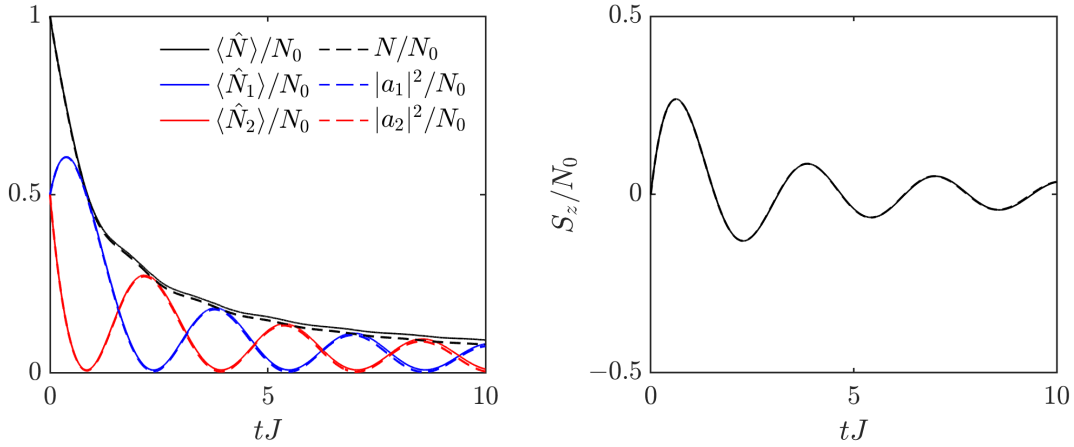


FIGURE 3.4: The left hand frame compares the quantum (solid lines) and semiclassical (dashed lines) dynamics of the total particle number (black), as well as the populations of site 1 (blue) and site 2 (red). The quantum (solid line) and semiclassical (dashed line) population imbalance is plotted in the right frame. In both cases the initial average particle number $N_0 = 20$, $UN_0 = 1J$, $\gamma N_0 = 0.8J$, and the initial coherent state parameters are $\alpha_1 = \sqrt{10}e^{i\pi/2}$ and $\alpha_2 = \sqrt{10}$.

In the right panel of Figure 3.5 we compare the quantum and semiclassical dynamics of the phase-coherence for the same system as in Figure 3.4. In the left panel we show the same comparison for the closed system for reference. As expected, a loss of phase

coherence is observed over time, indicating destruction of the condensate. The inclusion of losses leads to a better correspondence between the semiclassical and quantum dynamics for short times. This can be understood to some extent by the fact that since the Lindblad operators are holomorphic functions of $\hat{a}_j$ the dissipative parts of (3.49) and (3.50) may be written as a gradient flow. In the semiclassical limit the effect of the Lindblad operators is thus to localise the Wigner function.

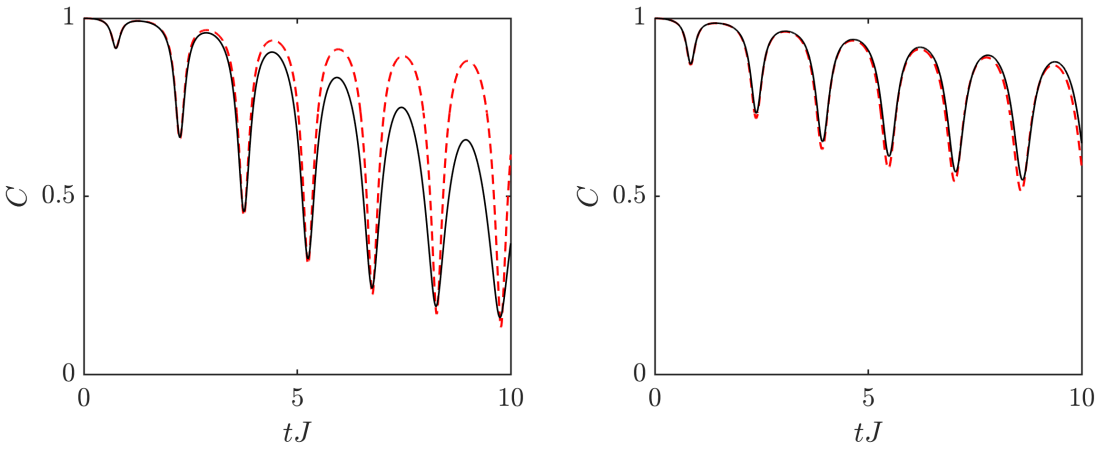


FIGURE 3.5: The quantum (black) and semiclassical (red dashed) dynamics of the phase coherence C between the two traps, for a closed system (left) and open system with $\gamma N_0 = 0.8J$ (right). In both cases $N_0 = 20$ and $UN_0 = 1J$. The initial coherent state parameters are the same as in Figure 3.4.

3.4.3 Ensemble averaged mean-field dynamics

As a further illustration we implement an ensemble calculation, which is capable of simulating non-Gaussian behaviour and requires only the semiclassical equations for the centre (3.35). Initial conditions a_i are sampled from the initial Gaussian Wigner function and the resulting ensemble is evolved via the semiclassical dynamics. Expectation values are then calculated by averaging over the trajectories

$$\langle \hat{A}(t) \rangle = \lim_{n\to\infty} \frac{1}{n} \sum_{i=1}^{n} A\left(a_i(t), \bar{a}_i(t)\right), \tag{3.51}$$

where A is the Weyl symbol of $\hat{A}$ and $a_i(t)$ is the solution to the semiclassical equations of motion with initial condition $a_i(0) = a_i$. This method is also referred to as the truncated

Wigner approximation and is a popular method for simulating beyond mean-field effects in both unitarily evolving systems and open systems described by the Lindblad equation [105, 106]. However, the semiclassical equations of motion for the Lindblad dynamics have previously been derived on a case-by-case basis, whereas the general phase-space dynamics (3.35) now enable an immediate application of the method.

Although the centre equations are deterministic, a stochastic element is maintained because of the sampling procedure. The ensemble spreads throughout the time evolution and can reproduce beyond mean-field effects, such as condensate depletion. This is illustrated in Figure 3.6 for a BEC with two-body losses, with the centre equations of motion given by (3.49) and (3.50). The population imbalance is depicted for two different interaction strengths. The ensemble average provides a good approximation of the breakdown dynamics, even in the case of a stronger interaction strength when a single mean-field trajectory is particularly poor.

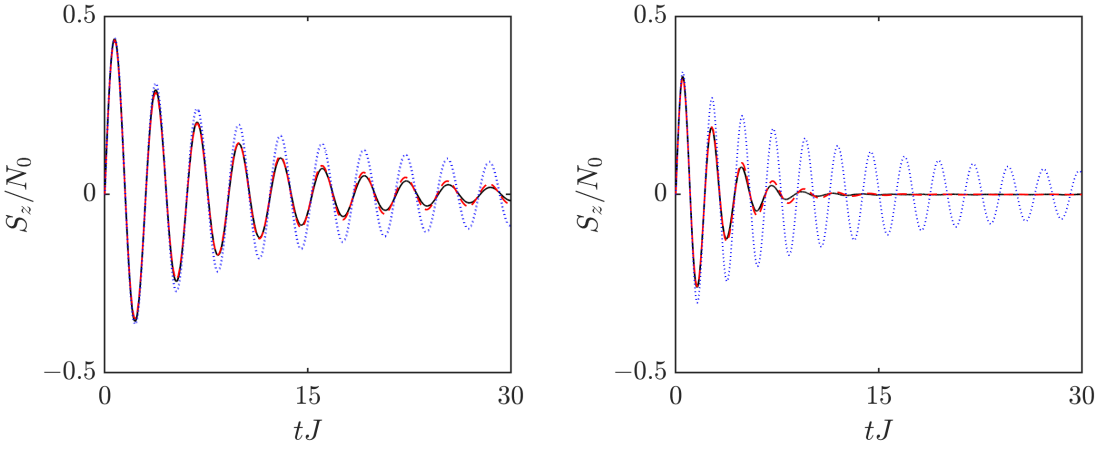


FIGURE 3.6: Comparison of the quantum (black), ensemble average (red dashed) and mean-field (blue small dashed) population imbalance $S_z = \langle \hat{N}_1 - \hat{N}_2 \rangle / 2$. In both cases $N_0 = 20$, the two-body decay rate $\gamma N_0 = 0.1J$ and the initial coherent state parameters are $\alpha_1 = \sqrt{10}\mathrm{e}^{i\pi/2}$ and $\alpha_2 = \sqrt{10}$. In the left frame $UN_0 = 1J$ and on the right $UN_0 = 5J$.

3.5 Lindblad dynamics as Schrödinger dynamics with a non-Hermitian Hamiltonian

In this section we approach the Lindblad dynamics from a different perspective. Specifically, by interpreting the Lindblad equation as a Schrödinger equation with a non-Hermitian Hamiltonian. The notion of a phase-space Schrödinger equation and phase-space wave functions have previously been explored in closed systems [107, 108]. Koda recently formulated several initial value semiclassical propagators for the Wigner function starting from an interpretation of the Moyal equation as a Schrödinger equation [109]. In the case of Lindblad dynamics, the new ingredient is the non-Hermiticity of the resulting Hamiltonian operator. In [95, 96] the semiclassical limit of Gaussian wave packet propagation for non-Hermitian Hamiltonians was developed. Reinterpreting the Wigner-evolution for Lindblad systems as a non-Hermitian Schrödinger equation, we can directly apply these results to obtain dynamical equations that can describe the semiclassical propagation of complex Gaussian Wigner functions, as they appear for example in the superpositions of Gaussian wave packets.

Let us begin by reviewing the semiclassical time evolution of Gaussian wave packets in non-Hermitian quantum systems [95, 96]. The initial states of interest are Gaussian wave packets of the form

$$\psi(q) = \frac{(\det \operatorname{Im} B)^{1/4}}{(\pi\hbar)^{n/4}} \mathrm{e}^{\frac{i}{\hbar}[(q-Q)\cdot B(q-Q)/2 + P\cdot(q-Q)+\alpha]}, \tag{3.52}$$

where $Q, P \in \mathbb{R}^n$ are the expectation values of position and momentum respectively, $\alpha \in \mathbb{C}$ is a phase factor and B is a complex symmetric matrix with $\operatorname{Im} B > 0$. A general non-Hermitian Hamiltonian $\hat{K}(\hat{q}, \hat{p})$ can be Taylor expanded about the time-dependent expectation values of position and momentum of the wave packet as

$$\hat{K}(\hat{q}, \hat{p}) \approx K + \nabla K \cdot (\hat{x} - X) + \frac{1}{2}(\hat{x} - X) \cdot K''(\hat{x} - X), \tag{3.53}$$

where K is the Weyl symbol of $\hat{K}$, $\hat{x} = (\hat{q}, \hat{p})$ and $X = (Q, P)$ is a vector of expectation values. The symbol K, as well as the first and second derivatives of K, are evaluated

at the centre of the wave packet X. Substituting the wave packet ansatz (3.52) and the Taylor expansion (3.53) into the Schrödinger equation $i\hbar\dot{\psi}(q) = \hat{K}\psi(q)$ yields the equations of motion for the wave packet parameters

$$\dot{X} = \Omega\nabla\mathrm{Re}K + G^{-1}\nabla\mathrm{Im}K, \tag{3.54}$$

$$\dot{B} = -BK_{pp}B - K_{qp}B - BK_{pq} - K_{qq}, \tag{3.55}$$

$$\dot{\alpha} = \frac{i\hbar}{4}\mathrm{Tr}\left([\mathrm{Im}B]^{-1}\mathrm{Im}\dot{B}\right) + P\cdot\dot{Q} - K + \frac{i\hbar}{2}\mathrm{Tr}\left(K_{pq} + K_{pp}B\right), \tag{3.56}$$

where the matrix G is related to B via

$$G = \begin{pmatrix} \mathrm{Im}\,B + \mathrm{Re}\,B[\mathrm{Im}\,B]^{-1}\,\mathrm{Re}\,B & -\mathrm{Re}\,B[\mathrm{Im}\,B]^{-1} \\ -[\mathrm{Im}\,B]^{-1}\,\mathrm{Re}\,B & [\mathrm{Im}\,B]^{-1} \end{pmatrix}. \tag{3.57}$$

The semiclassical dynamics of the centre (3.54) consist of a symplectic flow and a gradient part, where the main effect of the latter is to drive the system towards the maximum of $\mathrm{Im}K$. Moreover, the equations of motion for the centre couple to the width parameter, a feature having no counterpart in Hermitian systems or in the semiclassical Lindblad dynamics (3.19).

With these results at hand we now return to the semiclassical dynamics of the Lindblad equation. Consider an initial state $\phi(q) = \sum_j c_j\phi_j^A(q)$ that is a superposition of Gaussian wave packets

$$\phi_j^A(q) = \frac{(\det\mathrm{Im}\,A)^{1/4}}{(\pi\hbar)^{n/4}}\mathrm{e}^{\frac{i}{\hbar}[\frac{1}{2}(q-q_j)\cdot A(q-q_j)+p_j\cdot(q-q_j)]}, \tag{3.58}$$

where $q, q_j, p_j \in \mathbb{R}^n$ and A is an $n\times n$ complex symmetric matrix with $\mathrm{Im}\,A > 0$. The Wigner function of this state is

$$W(x) = \sum_{i,j} c_i^* c_j \psi_{ij}(x), \tag{3.59}$$

where $x = (q,p)$ and

$$\psi_{ij}(x) = \frac{1}{(\pi\hbar)^n}\mathrm{e}^{\frac{i}{\hbar}[(x-X_{ij})\cdot iG(x-X_{ij})+Y_{ij}\cdot(x-X_{ij})+\alpha_{ij}]} \tag{3.60}$$

is a complex Gaussian centred at $X_{ij} = \frac{1}{2}(q_i+q_j, p_i+p_j)$ with 'momentum' $Y_{ij} =$

$(p_j - p_i, q_i - q_j)$ and a complex phase $\alpha_{ij} = \frac{1}{2}(p_i + p_j) \cdot (q_i - q_j)$. The matrix G is related to the width A of the Gaussians in the superposition by

$$G = \begin{pmatrix} \operatorname{Im} A + \operatorname{Re} A[\operatorname{Im} A]^{-1} \operatorname{Re} A & -\operatorname{Re} A[\operatorname{Im} A]^{-1} \\ -[\operatorname{Im} A]^{-1} \operatorname{Re} A & [\operatorname{Im} A]^{-1} \end{pmatrix}. \tag{3.61}$$

As the phase-space Lindblad equation (3.6) is linear in the Wigner function W, the time evolution of (3.59) can be obtained by evolving each complex Gaussian ψ_{ij} individually and summing the results.

With this picture in mind our starting point is once again the Lindblad equation on phase space

$$i\hbar\partial_t\psi = H \star \psi - \psi \star H + i\sum_k L_k \star \psi \star \bar{L}_k - \frac{1}{2}\bar{L}_k \star L_k \star \psi - \frac{1}{2}\psi \star \bar{L}_k \star L_k. \tag{3.62}$$

However, we have now switched notation from W to ψ to indicate that we could be dealing with a complex component of the Wigner function, such as the ψ_{ij} in the discussion above. As this equation is linear in ψ, we can view (3.62) as a Schrödinger equation with a non-Hermitian Hamiltonian in a larger Hilbert space.

To this end we will use the fact that the star product can be written as the action of an operator on phase-space functions, see e.g. [109]. More precisely, we have

$$A \star \psi = \hat{A}^{(-)}\psi \quad \text{and} \quad \psi \star A = \hat{A}^{(+)}\psi, \tag{3.63}$$

where the operators

$$\hat{A}^{(\pm)} = A(\hat{x} \pm \frac{1}{2}\Omega\hat{y}) \tag{3.64}$$

act on the phase-space function $\psi(x)$. Furthermore,

$$\hat{x} = (q, p), \tag{3.65}$$

$$\hat{y} = (-i\hbar\nabla_q, -i\hbar\nabla_p), \tag{3.66}$$

are a pair of Hermitian operators that satisfy the canonical commutation relations

$$[\hat{x}_i, \hat{y}_j] = i\hbar\delta_{ij} \tag{3.67}$$

and can thus be treated like position and momentum operators in a space of doubled dimension. Making use of (3.63), the phase-space Lindblad equation (3.62) can be written as a Schrödinger equation

$$i\hbar\partial_t\psi(x,t) = \hat{K}(\hat{x},\hat{y})\psi(x,t), \tag{3.68}$$

with the non-Hermitian Hamiltonian

$$\hat{K}(\hat{x},\hat{y}) = \hat{H}^{(-)} - \hat{H}^{(+)} + i\sum_k \hat{L}_k^{(-)}\hat{\bar{L}}_k^{(+)} - \frac{1}{2}\widehat{(\bar{L}_k \star L_k)}^{(-)} - \frac{1}{2}\widehat{(\bar{L}_k \star L_k)}^{(+)}. \tag{3.69}$$

Finally, through the Wigner-Weyl transformation the non-Hermitian Hamiltonian $\hat{K}$ can be mapped onto the double phase-space function

$$\begin{aligned} K(x,y) = {} & H\big(x - \tfrac{1}{2}\Omega y\big) - H\big(x + \tfrac{1}{2}\Omega y\big) + i\sum_k L_k\big(x - \tfrac{1}{2}\Omega y\big) \star_2 \bar{L}_k\big(x + \tfrac{1}{2}\Omega y\big) \\ & - \frac{1}{2}(\bar{L}_k \star L_k)\big(x - \tfrac{1}{2}\Omega y\big) - \frac{1}{2}(\bar{L}_k \star L_k)\big(x + \tfrac{1}{2}\Omega y\big), \end{aligned} \tag{3.70}$$

where $\star_2$ denotes the Moyal product on the double phase-space. If we assume that the Hamiltonian and Lindblad operators are quantisations of $\hbar$-independent functions H and L_k, then using (3.3) we find that K has a semiclassical expansion $K = K^{(0)} + \hbar K^{(1)} + \ldots$, where the first two terms are given by

$$K^{(0)} = H^{(-)} - H^{(+)} + \sum_k \mathrm{Im}\left(\bar{L}_k^{(-)} L_k^{(+)}\right) - \frac{i}{2}\sum_k \left|L_k^{(-)} - L_k^{(+)}\right|^2, \tag{3.71}$$

$$K^{(1)} = \frac{1}{4}\sum_k \{\bar{L}_k, L_k\}^{(-)} + \{\bar{L}_k, L_k\}^{(+)}. \tag{3.72}$$

In the expression for $K^{(0)}$ we have separated real and imaginary parts, whereas $K^{(1)}$ is imaginary.[1]

We are now in the position to study the time evolution of initial wave packets of the form

$$\psi(x) = \frac{(\det \operatorname{Im} B)^{1/4}}{(\pi\hbar)^{n/2}} \mathrm{e}^{\frac{i}{\hbar}[(x-X)\cdot B(x-X)/2 + Y\cdot(x-X)+\alpha]}, \tag{3.73}$$

where $X, Y \in \mathbb{R}^{2n}$, $\alpha \in \mathbb{C}$ is a phase factor and B is a complex symmetric matrix with $\operatorname{Im} B > 0$. As shown above, such states appear as components of the Wigner function of superpositions of Gaussian states (3.59).

Direct application of the semiclassical equations (3.54-3.56) yields the following equations of motion

$$\dot{Z} = \Omega_2 \nabla \operatorname{Re} K^{(0)} + \mathcal{G}^{-1} \nabla \operatorname{Im} K^{(0)}, \tag{3.74}$$

$$\dot{B} = -BK^{(0)}_{yy}B - K^{(0)}_{xy}B - BK^{(0)}_{yx} - K^{(0)}_{xx}, \tag{3.75}$$

$$\begin{aligned}\dot{\alpha} = {} & \frac{i\hbar}{4} \operatorname{Tr}([\operatorname{Im} B]^{-1} \operatorname{Im} \dot{B}) + Y \cdot \dot{X} - K^{(0)}(X,Y) - \hbar K^{(1)}(X,Y) \\ & + \frac{i\hbar}{2} \operatorname{Tr}(K^{(0)}_{yx} + K^{(0)}_{yy} B),\end{aligned} \tag{3.76}$$

where $Z = (X, Y)$, $\nabla := (\partial_x, \partial_y)$ is the double phase-space gradient and Ω_2 is the double phase-space symplectic form. We have also defined

$$(K_{xy})_{ij} = \partial_{x_i} \partial_{y_j} K, \tag{3.77}$$

which satisfies $K_{yx} = (K_{xy})^T$, and $\mathcal{G}$ is related to B via

$$\mathcal{G} = \begin{pmatrix} \operatorname{Im} B + \operatorname{Re} B [\operatorname{Im} B]^{-1} \operatorname{Re} B & -\operatorname{Re} B [\operatorname{Im} B]^{-1} \\ -[\operatorname{Im} B]^{-1} \operatorname{Re} B & [\operatorname{Im} B]^{-1} \end{pmatrix}. \tag{3.78}$$

In order to obtain some insight into the properties of these equations of motion, we use the specific form of the real and imaginary parts of K in (3.71). We see that the imaginary

[1] We can allow more general functions that have asymptotic expansions in powers of $\hbar$, e.g., $H \sim H^{(0)} + \hbar H^{(1)} + \cdots$ and similarly for L_k. Then $K^{(0)}$ is determined by $H^{(0)}$ and $L^{(0)}_k$ only, and $K^{(1)}$ contains further terms depending on $H^{(1)}$, $L^{(1)}_k$ and $L^{(0)}_k$.

part is an even function of y, $\operatorname{Im} K^{(0)}(x,-y) = \operatorname{Im} K^{(0)}(x,y)$, with $\operatorname{Im} K^{(0)}(x,0) = 0$ and non-positive. The real part is an odd function of y, $\operatorname{Re} K^{(0)}(x,-y) = -\operatorname{Re}^{(0)} K(x,y)$. Using these properties and direct computations we find that

$$\nabla \operatorname{Re} K^{(0)}(x,0) = \left(0, \Omega\nabla_x H(x) + \Omega \sum_k \operatorname{Im}\left(L_k(x)\nabla \bar{L}_k(x)\right)\right), \tag{3.79}$$

$$\nabla \operatorname{Im} K^{(0)}(x,0) = \big(0,0\big). \tag{3.80}$$

By inserting this result into (3.74) we observe that if the initial value of Y is 0 then Y stays 0 for all times, and X satisfies the same equation of motion we found in (3.19). If we insert $B = 2iG$ into (3.75), and separate the real and imaginary parts of the Hessian matrix of $K^{(0)}$ at $y = 0$ in the same way, we find similarly that G satisfies (3.20). Hence our two different approaches are consistent.

The next natural question to ask is what happens when $Y \neq 0$. In this case we have a highly oscillatory initial Wigner function, which corresponds to a very non-classical state. As the imaginary part $\operatorname{Im} K^{(0)}(x,y)$ in (3.71) has a maximum at $y = 0$, we see that the gradient part in (3.74) wants to push Y to 0, and thereby reduce the frequency of the oscillations. In addition, (3.76) generates an exponentially damping factor if $\operatorname{Im} K^{(0)}(x,y) < 0$. Both of these effects are directly induced by the Lindblad operators. Thus, the general structure of the equations of motion (3.74) and (3.76), together with (3.71), allow us to conclude that oscillatory initial conditions will be smoothed and suppressed exponentially fast if they couple to the Lindblad terms via (3.71). This is a manifestation of decoherence [110], which is illustrated in an example at the end of this section.

Let us now compare these results to the work of Brodier and Ozorio de Almeida [94], who have also studied the Lindblad evolution of Gaussian states but for the special case of linear Lindblad operators of the form $\hat{L}_k = l_k \cdot \hat{x}$, with $l \in \mathbb{C}^{2n}$. The first difference is that Brodier and Ozorio de Almeida work with the chord function $\chi_{\hat{\rho}}(t,y) = \operatorname{Tr}\left(\hat{\rho} e^{-\frac{i}{\hbar} y\cdot\hat{x}}\right)$ rather than the Wigner function. As the chord function is the Fourier transform of the Wigner function, the chord function of (3.73) is given by

$$\chi(y) = \mathcal{N} e^{\frac{i}{\hbar}\left[\frac{1}{2}(y-Y)\cdot(\mathbb{N}+i\mathbb{M})(y-Y) + X\cdot y\right]}. \tag{3.81}$$

Here the matrices $\mathbb{N}, \mathbb{M}$ are real symmetric with $-B^{-1} = \mathbb{N} + i\mathbb{M}$ and the normalisation $\mathcal{N}$ can be determined from $\chi(0) = \mathrm{Tr}\,(\hat{\rho})$. The additional phase factors appearing in the Gaussian have been included in $\mathcal{N}$ for convenience. We now want to show that the equations of motion for X, Y, $\mathbb{N}$ and $\mathbb{M}$ match those in [94]. To begin with we note that the inverse of $\mathcal{G}$, defined in (3.78), is

$$\mathcal{G}^{-1} = \begin{pmatrix} \mathbb{M} + \mathbb{N}\mathbb{M}^{-1}\mathbb{N} & -\mathbb{N}\mathbb{M}^{-1} \\ -\mathbb{M}^{-1}\mathbb{N} & \mathbb{M}^{-1} \end{pmatrix}, \tag{3.82}$$

which can be obtained by direct computation. For linear Lindblad operators, $\mathrm{Im}\, K(x,y) = -\frac{1}{2} y \cdot \mathbb{D} y$ with $\mathbb{D} = \sum_k \mathrm{Re}(\bar{l}_k l_k^T)$, and the equation of motion for Z (3.74) may be rewritten as

$$\dot{X} = \nabla_y \,\mathrm{Re}\, K + \mathbb{N}\mathbb{M}^{-1}\mathbb{D}Y, \qquad \dot{Y} = -\nabla_x \,\mathrm{Re}\, K - \mathbb{M}^{-1}\mathbb{D}Y. \tag{3.83}$$

Taking the time derivative of $\mathbb{N} + i\mathbb{M} = -B^{-1}$ yields $\dot{\mathbb{N}} + i\dot{\mathbb{M}} = B^{-1}\dot{B}B^{-1}$. After inserting equation (3.75) for $\dot{B}$, and separating the real and imaginary parts, we further find the equations of motion for $\mathbb{M}$ and $\mathbb{N}$

$$\dot{\mathbb{M}} = \mathbb{D} + \mathrm{Re}\, K_{yx}\mathbb{M} + \mathbb{M}\,\mathrm{Re}\, K_{xy} - \mathbb{M}\,\mathrm{Re}\, K_{xx}\mathbb{N} - \mathbb{N}\,\mathrm{Re}\, K_{xx}\mathbb{M}, \tag{3.84}$$

$$\dot{\mathbb{N}} = -\,\mathrm{Re}\, K_{yy} + \mathrm{Re}\, K_{yx}\mathbb{N} + \mathbb{N}\,\mathrm{Re}\, K_{xy} + \mathbb{M}\,\mathrm{Re}\, K_{xx}\mathbb{M} - \mathbb{N}\,\mathrm{Re}\, K_{xx}\mathbb{N}\ . \tag{3.85}$$

Equations (3.83), (3.84) and (3.85) coincide with the ones derived in [94]. The main generalisation in the present approach is that it accounts for more general Lindblad operators, which need no longer be linear functions of $\hat{x}$. For general Lindblad operators $\mathrm{Im}\, K^{(0)}$ will depend on both y *and* x, leading to additional terms in the equations of motion for $X, Y, \mathbb{N}$ and $\mathbb{M}$ compared to those in [94]. This can be observed in (3.20), where the equation for $G = \mathbb{M}^{-1}/2$ contains terms involving second derivatives of the Lindblad operators.

We finally show how the doubled phase-space approach allows for a treatment of interference terms in the Wigner function by obtaining the semiclassical dynamics of an initial Schrödinger cat state in a damped anharmonic oscillator. Working in dimensionless units

with $\hbar = 1 = m = \omega$, the Hamiltonian is

$$\hat{H} = \frac{1}{2}(\hat{q}^2 + \hat{p}^2) + \frac{\beta}{4}\hat{q}^4, \tag{3.86}$$

where β controls the degree of anharmonicity. The damping is modelled with the Lindblad operator

$$\hat{L} = \sqrt{\frac{\gamma}{2}}(\hat{q} + i\hat{p}), \tag{3.87}$$

where γ is a damping rate. When $\beta = 0$ the semiclassical dynamics are exact. The corresponding double phase-space symbol K is found from (3.70) to be

$$K^{(0)}(x, y) = (\Omega x) \cdot y - \frac{\beta}{4}(x_q y_p^3 + 4x_q^3 y_p) - \frac{\gamma}{2} x \cdot y - \frac{i\gamma}{4} y \cdot y, \tag{3.88}$$

and

$$K^{(1)}(x, y) = \frac{i\gamma}{2}. \tag{3.89}$$

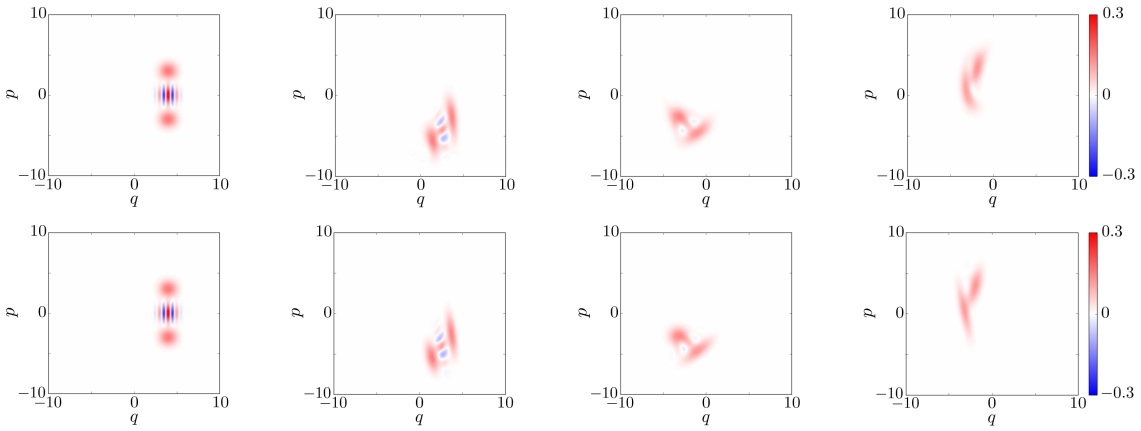


FIGURE 3.7: The quantum (top) and semiclassical (bottom) dynamics of an initial cat state in an anharmonic potential with $\beta = 0.1$ and damping at a rate $\gamma = 0.3$. Times $t = 0,\ 0.5,\ 1.5,\ 2.5$ are shown from left to right.

We consider an initial state that is a cat state, comprised of two Gaussians with $A = 1$ and both centred at $q = 4$ with momenta $p = \pm 3$. The Wigner function of this state (depicted on the left of Figure 3.7) is composed of two Gaussians centred at $(q = 4, p = \pm 3)$ in phase space, and an interference pattern with a Gaussian envelope centred at the midpoint of the two Gaussians. The semiclassical dynamics are obtained by evolving each complex Gaussian component of the initial Wigner function, summing

up the results and applying the Wigner function normalisation condition $\int dx\, W(x) = 1$. The resulting semiclassical dynamics are compared with the quantum dynamics in Figure 3.7. The Gaussian approximation clearly reproduces the essential features of the oscillation, damping and decoherence.

In Figure 3.8 we further depict a comparison between the semiclassical position and momentum expectation values and the quantum results for a longer timescale. We find that there is good agreement at short times. At longer times the results deviate as expected, while still capturing the qualitative features of the dynamics.

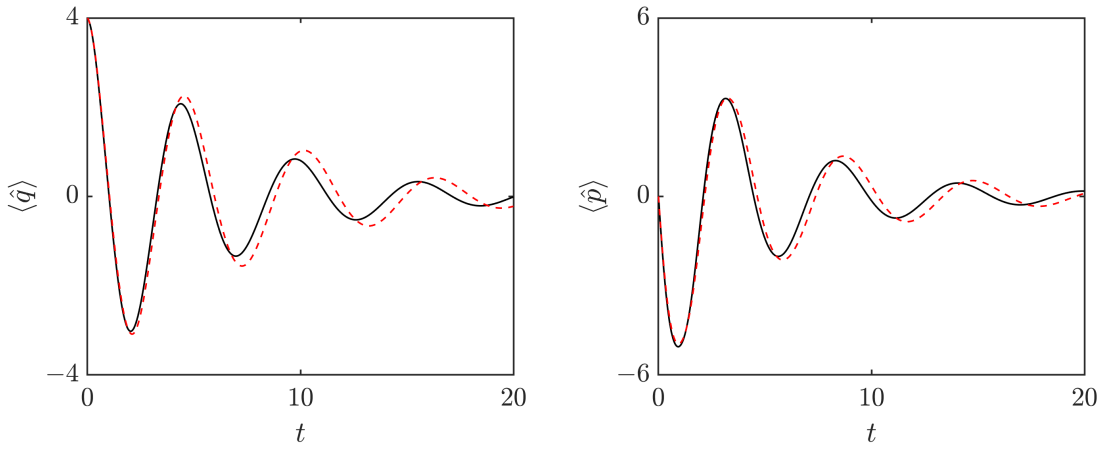


FIGURE 3.8: Time evolution of the position (left) and momentum (right) expectation values of the cat state above. The quantum dynamics (black) are compared to the semiclassical results (red dashed). The anharmonic parameter $\beta = 0.1$ and the damping rate $\gamma = 0.3$.

3.6 Summary

We have investigated the dynamics of Gaussian states in open quantum systems described by Lindblad equations in the semiclassical limit. This yields a new type of semiclassical phase-space dynamics incorporating the effects of damping and decoherence in the dynamics of the phase-space coordinates as well as a semiclassical approximation for the quantum covariances. This dynamics has an interesting geometric structure, which we have explored in a number of example systems. We have also transformed the dynamics

to complex phase-space variables, as they appear naturally in many models in quantum optics.

What makes the dynamics of Gaussian wave packets particularly appealing for closed quantum systems is the fact that an arbitrary initial wave function can be expanded into Gaussian states, each of which can be propagated independently. This expansion can also be repeated at intermediate time-steps, allowing for numerical quantum dynamics that can in principle be arbitrarily accurate [88, 89]. Due to the fact that Lindblad dynamics generates mixed states, this approach cannot be directly generalised to the case of open systems considered here. However, we have demonstrated how the interpretation of the Wigner dynamics in phase space as a Schrödinger dynamics with non-Hermitian Hamiltonian can be used to circumvent this issue.

Chapter 4

Non-adiabatic transitions through exceptional points in the band structure of a PT-symmetric lattice

4.1 Introduction

In the previous chapters we have seen several examples of non-Hermitian Hamiltonians appearing naturally in the Lindblad description of open quantum systems. However, non-Hermitian and PT-symmetric quantum theories constitute a thriving research area in their own right [7, 8]. In particular, exceptional points, at which two or more eigenstates of a system coalesce, have been at the centre of research interest both theoretically and experimentally [29, 111–119]. A number of these studies have investigated the behaviour of the wave function when parameters are varied cyclically around such a point [120–123]. In Hermitian quantum physics the adiabatic theorem ensures that a system prepared in an eigenstate remains in an instantaneous eigenstate, when parameters are varied sufficiently slowly. The situation is more involved in non-Hermitian systems. Here the exponential relative decay between different eigenstates competes with the exponentially small non-adiabatic corrections, which can lead to apparently non-adiabatic behaviour

even in the adiabatic limit of infinitely slow parameter variation [124–127]. This causes asymmetric behaviour encircling exceptional points.

In this chapter we go one step further and consider the behaviour of a system driven directly through an exceptional point. In particular, we study a two-level system driven through two consecutive exceptional points, at finite speed and in the adiabatic limit. The system is close to being Hermitian at the beginning and the end of the parameter sweep, making it meaningful to study the ratio of transmitted population between the instantaneous eigenstates far away from the exceptional points. We derive an *analytic* expression for the transmission probability. For adiabatic parameter variations this predicts a loss of information, leading to an equal redistribution of the population between the states coalescing in the exceptional point. In the fast driving limit quantum quench behaviour is recovered.

We further demonstrate how this could be observed using Bloch oscillations in a PT-symmetric lattice in a realistic experimental setup. Interestingly, the Hamiltonian of this system itself does not have any exceptional points. A similar effect of partial transitions between Bloch bands at exceptional points has recently been observed numerically in a more complicated lattice structure and experimentally using optical fibre loops [128, 129]. The quantitative description provided here explains these effects and opens up new avenues for the control of optical beams. Most of the results of this chapter have been published in [130]. In Chapter 5 we shall return to the Lindblad equation and consider the possibility of observing these effects in a quantum system by engineering single-particle losses from the odd sites of an optical lattice.

4.2 Adiabatic transitions in a two-mode system

Consider the PT-symmetric Hamiltonian

$$\hat{H} = \begin{pmatrix} -v & i\gamma \\ i\gamma & v \end{pmatrix}, \tag{4.1}$$

where γ and v are real parameters and we set $\gamma > 0$ without loss of generality. This Hamiltonian describes two states with an energy difference of $2v$ and an asymmetric coupling $i\gamma$. Its direct implementation in a two-waveguide setup is nontrivial due to the nonreciprocal coupling between the two modes. Nonreciprocal coupling between two resonators has been discussed for example in [131]. Here we shall consider a perhaps less obvious implementation of the Hamiltonian (4.1), as the Bloch Hamiltonian of a PT-symmetric tight-binding lattice. This setup allows for a direct visual observation of the population transfer between the two modes when the system is driven through the exceptional points.

The eigenvalues of the Hamiltonian (4.1)

$$\lambda_{\pm} = \pm\sqrt{v^2 - \gamma^2} \tag{4.2}$$

in dependence on v for a fixed value of γ are depicted in the left panel of Figure 4.1. The right panel shows the overlap between the two (right) eigenstates in dependence on v. For values of $|v| > \gamma$ the eigenvalues are real and for very large values of $|v|$ the eigenstates are almost orthogonal (and tend towards the standard basis vectors), leading the system to behave in an essentially Hermitian manner. For intermediate values of v the non-Hermiticity is more apparent in the non-vanishing overlap of the eigenstates. The system has two exceptional points located at $v = \pm\gamma$, at which both eigenvalues coalesce and the Hamiltonian has only a single eigenstate. For $|v| < |\gamma|$ the eigenvalues are complex conjugate and there is one exponentially growing and one exponentially decaying mode.

Suppose that the system is initially in one of the eigenstates for very large negative $v \ll -\gamma$, and v is increased adiabatically. One expects the state to closely follow the instantaneous eigenstate it originated from up until the exceptional point. At this point the initial instantaneous eigenstate coalesces with the other and it cannot be inferred in which of the two states the system originated. Thus, the population of the two instantaneous eigenstates is expected to be equal immediately after the exceptional point. However, this argument does not take into account that once the parameters have passed through the first exceptional point, one of the states decays exponentially while the other

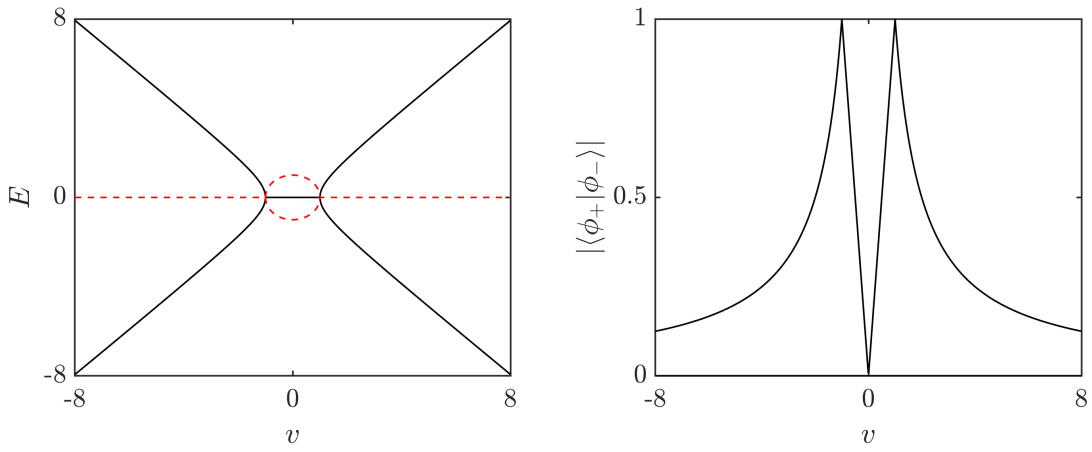


FIGURE 4.1: Eigenvalues and overlap of the eigenstates of the model Hamiltonian (4.1). The left panel shows the real (solid black line) and imaginary (dashed red line) parts of the eigenvalues, the right panel shows the overlap of the eigenstates, both in dependence on the coupling strength v for a fixed value of $\gamma = 1$.

grows exponentially. If v is varied adiabatically, the system has enough time to 'switch' to the configuration where the entire remaining population is in the exponentially growing state. When the system later passes through the second exceptional point the population is again equally distributed between the two eigenstates. Now both the states are stable and for large positive values of v the population is expected to be equally distributed between the two instantaneous eigenstates. That is, information about the initial state is lost when the system is driven *adiabatically* through the exceptional points.

This behaviour is indeed observed in numerical simulations and occurs independently of the initial state. In Figure 4.2 the relative population of the instantaneous eigenstates (calculated as the normalised projection onto the left eigenstate) and the overall norm of the wave function are plotted as a function of time. Here $v = \alpha t$ is slowly varied from a large negative initial value to a large positive final value for an initial eigenstate (top) and a randomly selected initial state (bottom). The norm, depicted on the right, grows approximately exponentially in the region between the two exceptional points and continues to oscillate after the second exceptional point due to the lack of orthogonality of the eigenstates. The oscillations die off at large values of v where the eigenstates become approximately orthogonal.

After driving the system though the pair of exceptional points, the state of the system

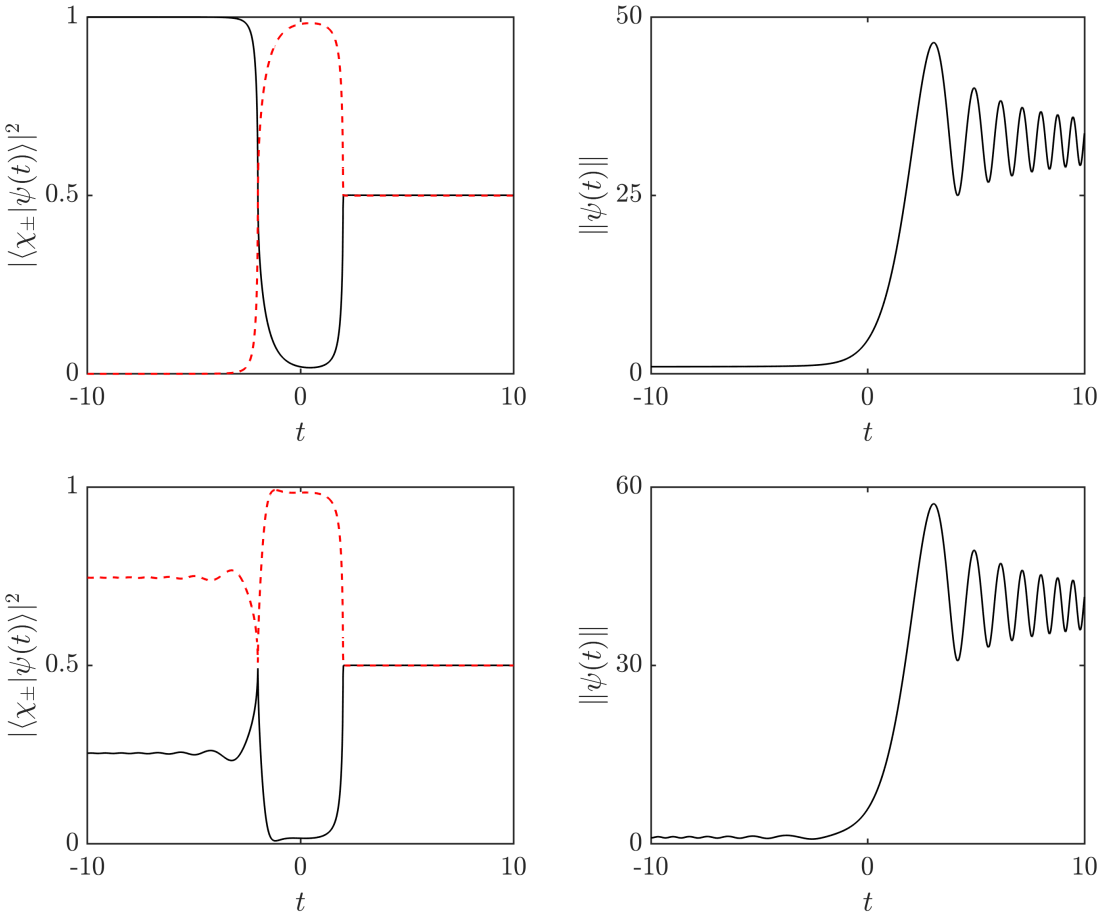


FIGURE 4.2: Dynamics generated by the Hamiltonian (4.1). v is varied linearly in time as $v = \alpha t$ from $v_i = -5$ to $v_f = 5$ with $\alpha = 0.5$ and $\gamma = 1$. The initial state is one of the instantaneous eigenstates (top) and a randomly selected state (bottom). The left panel shows the population in the two instantaneous eigenstates, the right panel shows the overall norm of the wave function.

is given by $\psi = (\psi_1', \psi_2')$ in the basis of eigenstates. In the adiabatic limit we have $|\psi_1'|^2 = \frac{1}{2} = |\psi_2'|^2$. Thus, while the initial state has two degrees of freedom (for example the relative phase between the two components and an amplitude), the final state is parameterised by a single variable, which is a relative phase between the two components. As there is clearly no one-to-one mapping from a one-dimensional space to a two-dimensional space, one cannot time reverse ψ to obtain the initial state. Of course, this observation is rather academic in nature, as no experiment will be truly adiabatic. Thus, in principle, one might be able to obtain the initial state by time reversing the dynamics. However, our numerical simulations show that the backwards time evolution

can be very sensitive to small perturbations. In the following section we shall investigate the instability with respect to time reversal in some detail.

4.3 Imperfect time reversal and the Loschmidt echo

Due to the presence of gain/loss in our system, the backward temporal evolution of the system can be very sensitive to small perturbations. Let us first suppose that an initial state $|\psi_i\rangle$ is propagated forwards to time t with the time-independent Hamiltonian $\hat{H}_1$, and then imperfectly time reversed by the time-independent Hamiltonian $\hat{H}_2$, yielding the final state

$$|\psi_f\rangle = \mathrm{e}^{i\hat{H}_2 t}\mathrm{e}^{-i\hat{H}_1 t}|\psi_i\rangle. \tag{4.3}$$

The Loschmidt echo $M(t)$ provides a measure of the sensitivity of the system to perturbations in the backward temporal evolution and is defined as [132]

$$M(t) = \frac{|\langle\psi_i|\psi_f\rangle|^2}{\langle\psi_i|\psi_i\rangle\langle\psi_f|\psi_f\rangle}. \tag{4.4}$$

That is, for perfect time reversal we have $M(t) = 1$, while for imperfect time reversal $M(t) < 1$. This measure of the stability of quantum motion due to perturbations in the Hamiltonian was originally introduced by Peres [132] in an effort to explain irreversibility at the microscopic level. The Loschmidt echo is a measurable quantity and has attracted attention across a range of disciplines [133], in particular in the field of quantum chaos. In contrast to classical systems, the invariance of the inner product between two pure states undergoing a unitarity time evolution implies that quantum states cannot exhibit a sensitivity to initial conditions. Thus, Peres proposed that one should instead look for sensitivity in the Hamiltonian generating the time evolution. And indeed there is a strong correspondence between chaos in a classical system and the behaviour of the Loschmidt echo in the quantum counterpart.

The above is readily generalised for time-dependent Hamiltonians $\hat{H}_1(t)$ and $\hat{H}_2(t)$. In particular, the final state may be written as

$$|\psi_f\rangle = \hat{U}_2(t_0, t)\hat{U}_1(t, t_0)|\psi_i\rangle, \tag{4.5}$$

where the forwards and backwards time-evolution operators have the form

$$\hat{U}_1(t, t_0) = T \exp\left(-i \int_{t_0}^{t} dt' \hat{H}_1(t')\right), \quad \hat{U}_2(t_0, t) = \bar{T} \exp\left(-i \int_{t}^{t_0} dt' \hat{H}_2(t')\right). \tag{4.6}$$

Here T is the chronological ordering operator, $\bar{T}$ is the anti-chronological ordering operator and the time-evolution operators are generally non unitary for non-Hermitian Hamiltonians.

Suppose that the initial state $|\psi_i\rangle$ is propagated forwards in time from $t_0 = -T$ to $t = T$, through both the exceptional points, where $\hat{H}_1(t) = \hat{H}(t)$ is the Hamiltonian in (4.1). By defining the parameter $\alpha \propto 1/T$ the limit $T \to +\infty$ corresponds to the adiabatic limit. Setting $\hat{H}_2(t) = \hat{H}(t)$ yields a perfect time-reversed propagation and the Loschmidt echo is equal to unity. However, *in practice* perfect time reversal can be difficult. This results in a final state $|\psi_f\rangle$ that differs dramatically from the initial state $|\psi_i\rangle$, and therefore a loss of information about the initial state for all practical purposes.

In the top left frame of Figure 4.3 we perturb γ in the time-reversed Hamiltonian and demonstrate with an initial state $\psi_i = (0, 1)$ that the Loschmidt echo can be less than unity for slow, but finite, parameter variation. For small T the usual quantum quench behaviour is observed, and the initial and final states coincide. On the other hand, as T increases we observe that $M(T)$ decays and converges to $1/2$, indicating that the populations $|\psi_{f,j}|^2/|\psi_f|^2 \to 1/2$, as expected from the discussion in the previous section. The remaining frames show the population imbalance (in the standard basis) for the forwards and backwards time evolution. Small differences in the state are quickly amplified in the region of exponential growth, so that the time-reversed population dynamics do not perfectly follow the forwards-time dynamics.

The levelling of the populations for large T in the perturbed time-reversed dynamics occurs independently of the initial state, as illustrated in Figure 4.4 for a random initial

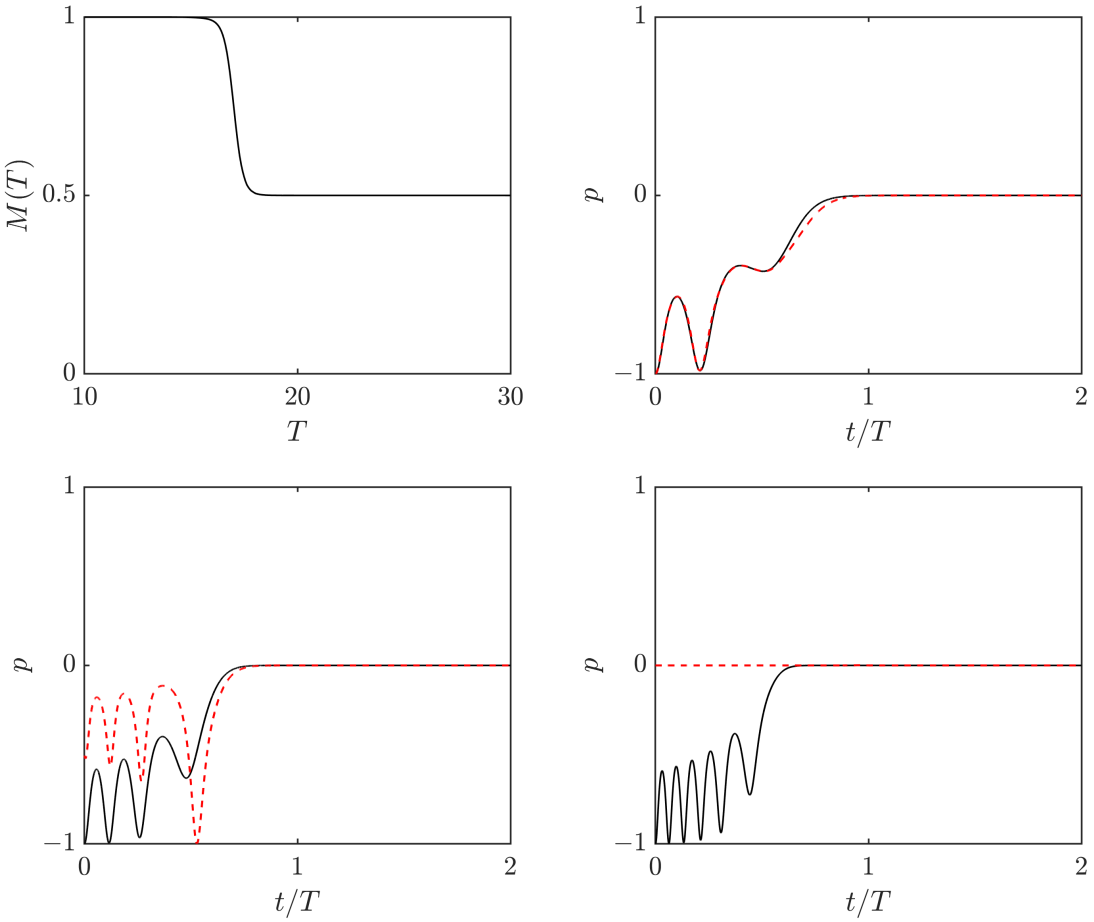


FIGURE 4.3: (Top left) The Loschmidt echo as a function of the parameter T for the initial state $\psi_i = (0, 1)$, with $\alpha = 2/T$ for each value of T. The remaining frames show the population imbalance p as a function of time for the forwards (black solid) and backwards (red dashed) time evolution with $T = 10$ (top right), $T = 17$ (bottom left) and $T = 30$ (bottom right). In each plot, $\gamma = 1$ in the forwards-time Hamiltonian and $\gamma = 1 + 10^{-14}$ in the backwards-time Hamiltonian.

state. However, for general initial states the Loschmidt echo $M(T)$ oscillates as a function of T, in contrast to the evolution depicted in Figure 4.3 for the initial state $\psi_i = (0, 1)$. As the population imbalance of the time-reversed dynamics is zero in the large T limit, these oscillations must be due to a difference between the relative phases of ψ_i and ψ_f. Noting that $|\psi_{f,j}|^2/|\psi_f|^2 \to 1/2$ for large T, the Loschmidt echo (4.4) may be approximated as

$$M(T) \approx \frac{1}{2} + |\psi_{i,1}||\psi_{i,2}| \cos\left[(\theta_1 - \theta_2) - (\phi_1 - \phi_2)\right]. \tag{4.7}$$

Here we have assumed that the initial state is normalised $\langle\psi_i|\psi_i\rangle = 1$, and introduced

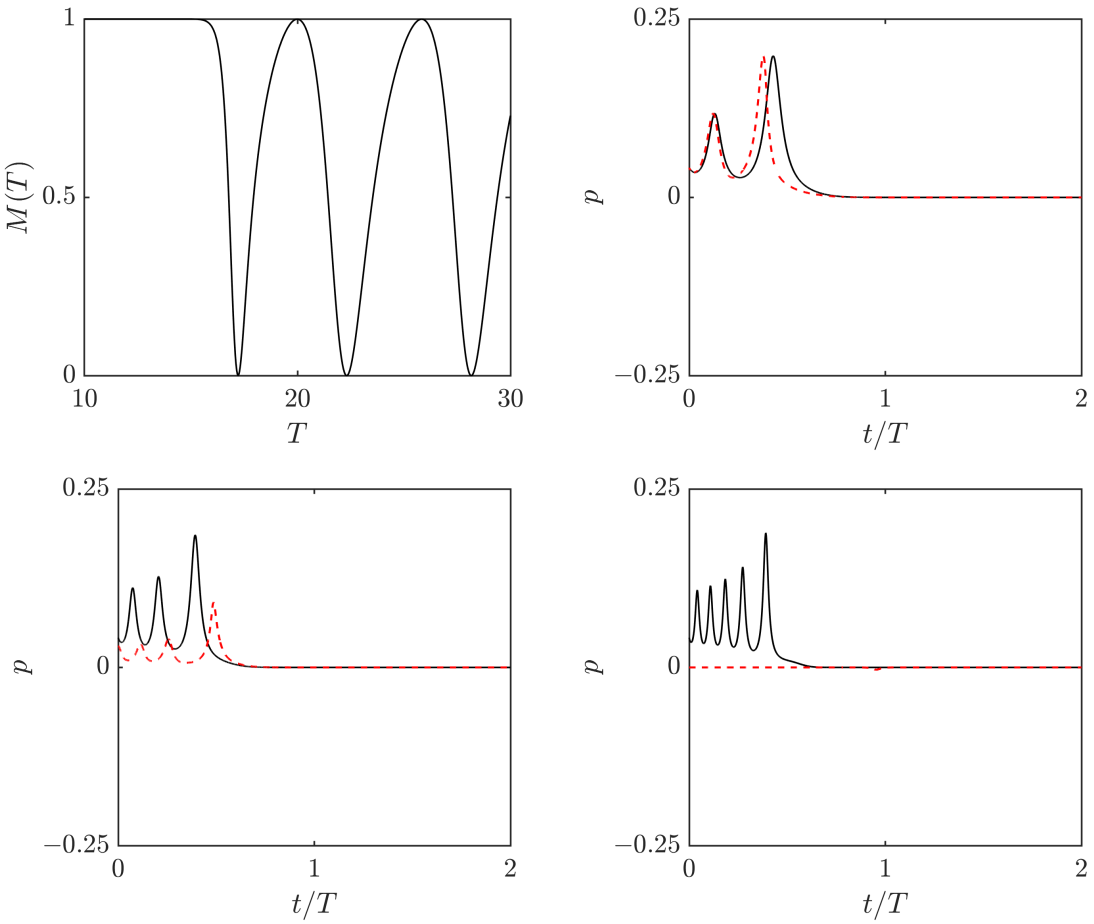


FIGURE 4.4: As in Figure 4.3, with a random initial state ψ_i. The random initial state is the same as in Figure 4.2.

the phases ϕ_j and θ_j via $\psi_{i,j} = |\psi_{i,j}|e^{i\phi_j}$ and $\psi_{f,j} = |\psi_{f,j}|e^{i\theta_j}$ respectively. The argument of the cosine is the difference between the initial and final relative phases. Clearly, for $\psi_i = (0, 1)$ the large T Loschmidt echo (4.7) is independent of the phases and is equal to $1/2$. However, for a general initial state the interference term in (4.7) results in an oscillating Loschmidt echo that can take values between 0 and 1.

These results raise interesting questions regarding the relationship between quantum chaos and the presence of exceptional points. However, these topics are rather tangential to the current chapter, so we leave a thorough analysis of the Loschmidt echo in non-Hermitian systems for future work. Having demonstrated the sensitivity of the backwards time evolution to small perturbations, we see that employing time reversal to retrieve information about the initial state is clearly not as trivial as it may at first seem.

4.4 Non-adiabatic transitions in a two-mode system

Let us now consider the behaviour of the system when v is varied non-adiabatically. This can be understood analytically by closely following Zener's derivation of the famous Landau-Zener-Majorana-Stückelberg formula [134]. We assume the parameter v to vary linearly in time. That is, $v = \alpha t$, $\alpha \in \mathbb{R}^+$, where t runs from minus to plus infinity. At $t \to \pm\infty$ the eigenstates are given by the two uncoupled levels, i.e., the standard basis. We assume that the system is initially in the eigenstate

$$|\psi_1\left(t \to -\infty\right)|^2 = 0, \quad |\psi_2\left(t \to -\infty\right)|^2 = 1. \tag{4.8}$$

We want to deduce the transmission probability into the same diabatic state at $t \to +\infty$, given by

$$P_{\mathrm{tr}} = \frac{|\psi_2\left(t \to +\infty\right)|^2}{|\psi_1\left(t \to +\infty\right)|^2 + |\psi_2\left(t \to +\infty\right)|^2}. \tag{4.9}$$

For this purpose we start from the Schrödinger equation for $\psi = (\psi_1, \psi_2)$

$$i\dot{\psi}_1 = -\alpha t\psi_1 + i\gamma\psi_2, \tag{4.10}$$

$$i\dot{\psi}_2 = i\gamma\psi_1 + \alpha t\psi_2, \tag{4.11}$$

and transform (4.10) into the second order differential equation

$$\ddot{\psi}_1 + \left(-\gamma^2 - i\alpha + (\alpha t)^2\right)\psi_1 = 0. \tag{4.12}$$

Applying the transformation $z(t) = \mathrm{e}^{-i\pi/4}\sqrt{2\alpha}t$ converts this equation into the Weber equation

$$\frac{d^2\psi_1}{dz^2} + \left(\nu + \frac{1}{2} - \frac{1}{4}z^2\right)\psi_1 = 0, \tag{4.13}$$

with $\nu = -i\beta$ and $\beta = \gamma^2/2\alpha$. A solution satisfying the initial conditions (4.8) is given by

$$\psi_1(t) = AD_{-\nu-1}\left(-iz(t)\right), \tag{4.14}$$

where A is a normalisation factor and D_ν is a Weber (or parabolic cylinder) function [135]. The normalisation factor is determined from the asymptotic value[1]

$$\psi_1\left(t \to -\infty\right) = A\mathrm{e}^{-i\pi(\nu+1)/4}\mathrm{e}^{-iR^2/4}R^{-\nu-1}, \tag{4.15}$$

with $R = \sqrt{2\alpha}t$. Inserting this into the equation of motion (4.10) provides an asymptotic expression for ψ_2

$$\psi_2\left(t \to -\infty\right) = -i\frac{\sqrt{2\alpha}}{\gamma}A\mathrm{e}^{-i\pi(\nu+1)/4}\mathrm{e}^{-iR^2/4}R^{-\nu}, \tag{4.16}$$

which, together with the initial conditions, yields $|A|^2 = \beta\mathrm{e}^{\pi\beta/2}$. Making use of the asymptotic value

$$\psi_1\left(t \to +\infty\right) = A\frac{\sqrt{2\pi}}{\Gamma\left(\nu+1\right)}\mathrm{e}^{i\pi\nu/4}\mathrm{e}^{iR^2/4}R^{\nu}, \tag{4.17}$$

and well-known properties of the gamma function, leads to the amplitude

$$\left|\psi_1\left(t \to +\infty\right)\right|^2 = \mathrm{e}^{2\pi\beta} - 1. \tag{4.18}$$

For unitary time evolution $\left|\psi_2\left(t \to +\infty\right)\right|^2$ can be obtained from $\left|\psi_1\left(t \to +\infty\right)\right|^2$ due to the conservation of probability. However, for the non-Hermitian dynamics considered here the total probability is no longer conserved. The amplitude $\left|\psi_2\left(t \to +\infty\right)\right|^2$ must be calculated by other means, starting with equation (4.11) and following a similar procedure to that above. Performing the transformation $z(t) = \mathrm{e}^{i\pi/4}\sqrt{2\alpha}t$ converts the equation of motion for the component ψ_2

$$\ddot{\psi}_2 + \left(-\gamma^2 + i\alpha + (\alpha t)^2\right)\psi_2 = 0 \tag{4.19}$$

into the Weber equation

$$\frac{d^2\psi_2}{dz^2} + \left(-\nu + \frac{1}{2} - \frac{1}{4}z^2\right)\psi_2 = 0, \tag{4.20}$$

[1]The various asymptotic expressions of the Weber function used in this chapter are listed in Appendix B for reference.

where $\nu = -i\beta$ with $\beta = \gamma^2/2\alpha$. Due to the initial condition $|\psi_2(t \to -\infty)|^2 = 1$ the solution should be non-vanishing as $t \to -\infty$. Furthermore, the solution should have asymptotic behaviour consistent with equation (4.16). Thus, the solution is of the form $\psi_2(t) = BD_{-\nu}(-z(t))$. Making use of the asymptotic expansion

$$\psi_2(t \to -\infty) = B\mathrm{e}^{-i\pi\nu/4}\mathrm{e}^{-iR^2/4}R^{-\nu} \tag{4.21}$$

and the initial conditions (4.8) yields the normalisation factor $|B|^2 = \mathrm{e}^{\pi\beta/2}$. This, together with the asymptotic result for the Weber function

$$|D_{-\nu}(-z(t \to +\infty))|^2 = \mathrm{e}^{3\pi\beta/2}, \tag{4.22}$$

leads to the amplitude

$$|\psi_2(t \to +\infty)|^2 = \mathrm{e}^{2\pi\beta}. \tag{4.23}$$

Inserting (4.18) and (4.23) into the definition of the transmission probability (4.9) finally yields

$$P_{\mathrm{tr}} = \left(2 - \mathrm{e}^{-\frac{\pi\gamma^2}{\alpha}}\right)^{-1}. \tag{4.24}$$

As expected, this approaches $\frac{1}{2}$ in the adiabatic limit. On the other hand, in the limit of fast driving, the usual quantum quench behaviour is observed. For intermediate values of α the transmission probability monotonically increases with α, interpolating between the two limits. Figure 4.5 depicts the transmission probability as a function of α for various values of γ.

4.5 The two-mode model as the Bloch Hamiltonian of a PT-symmetric tight-binding lattice

We now demonstrate that the model (4.1) can accurately describe the band transitions in a PT-symmetric lattice with an applied static force. This allows for a direct observation of the transition through a series of exceptional points in dependence on the adiabatic parameter, which can be tuned via the static force. Let us consider a PT-symmetric

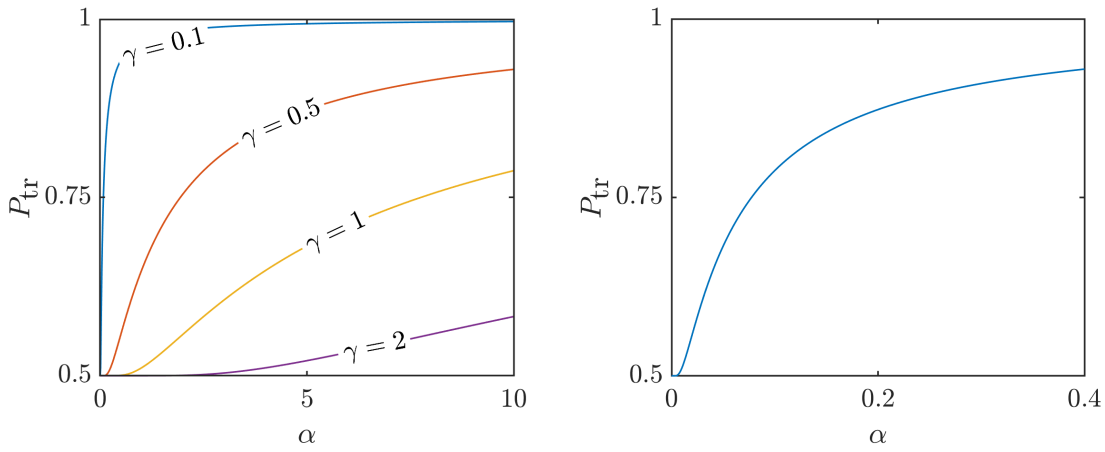


FIGURE 4.5: Transmission probability (4.24) as a function of the driving parameter. The left panel shows the variation with γ, the right panel focuses on small driving parameter values for $\gamma = 0.1$.

tight-binding Hamiltonian of the form

$$\hat{H} = \sum_j -\big(|j+1\rangle\langle j| + |j\rangle\langle j+1|\big) + i\Gamma(-1)^j |j\rangle\langle j|, \tag{4.25}$$

with a gain and loss rate $\Gamma \in \mathbb{R}^+$. This model can be realised, for example, as a chain of waveguides with absorption in every other waveguide and optical gain of an equal strength in the waveguides in between. Some of the properties of this model have previously been discussed in [136, 137]. A passively PT-symmetric version of this model has been implemented experimentally in [138]. The single-band tight-binding Hamiltonian without gain/loss is briefly reviewed in Appendix C.

It is convenient to study the system in the quasimomentum representation, i.e., in the basis of the Bloch states

$$|k\rangle = \sum_j |j\rangle\langle j|k\rangle = \frac{1}{\sqrt{2\pi}} \sum_j \mathrm{e}^{ikj} |j\rangle, \tag{4.26}$$

where the quasimomentum k is confined to the region $-\pi \leq k \leq \pi$. The Bloch states are orthogonal and normalised to the 2π-periodic delta comb $\langle k|k'\rangle = \delta_{2\pi}(k'-k)$. The Hamiltonian (4.25) is not diagonal in the quasimomentum representation and one finds

the equation of motion

$$i\dot{\psi}(k) = -2\cos k\,\psi(k) + i\Gamma\,\psi(k+\pi). \tag{4.27}$$

In a similar spirit to [139], we introduce the two-component function $\Psi = (\Psi_1, \Psi_2)$ with $\Psi_1(k) = \psi(k)$ and $\Psi_2(k) = \psi(k+\pi)$. The time evolution may then be written as the two-level Schrödinger equation

$$i\dot{\Psi} = (-2\cos k\sigma_z + i\Gamma\sigma_x)\,\Psi = h(k)\Psi, \tag{4.28}$$

where σ_i are Pauli matrices and the Bloch Hamiltonian is defined as

$$h(k) = \begin{pmatrix} -2\cos k & i\Gamma \\ i\Gamma & 2\cos k \end{pmatrix}. \tag{4.29}$$

The k-dependent eigenvalues of $h(k)$ define the dispersion relation of the two band system

$$E_\pm(k) = \pm\sqrt{4\cos^2 k - \Gamma^2}. \tag{4.30}$$

The band structure is complex for arbitrarily small values of Γ. For values of $\Gamma < 2$ there are exceptional points at $2|\cos k| = \Gamma$ and when $2|\cos k| < \Gamma$ the energy is imaginary. For $\Gamma > 2$ the bands are purely imaginary and there are no exceptional points. Here we focus on Γ values well below this critical point. An example of the band structure for $\Gamma = 0.2$ is depicted in the top row of Figure 4.6. The bottom row of the same figure shows the modulus squared of the components of the eigenstates. The eigenstates are close to the standard basis vectors at $k = 0$ and $k = \pi$. However, as illustrated in Figure 4.7 for $\Gamma = 0.8$, when Γ is increased this is no longer the case.

We now show that the two-component function $\Psi(k)$ of a broad Gaussian beam in position space is an approximate eigenstate of the Bloch Hamiltonian, when the Bloch states are close to the standard basis vectors. Consider a Gaussian in real space representation given by

$$\psi(j) = \mathcal{N}\mathrm{e}^{-(j-q_0)^2/2\sigma^2 + ik_0(j-q_0)}, \tag{4.31}$$

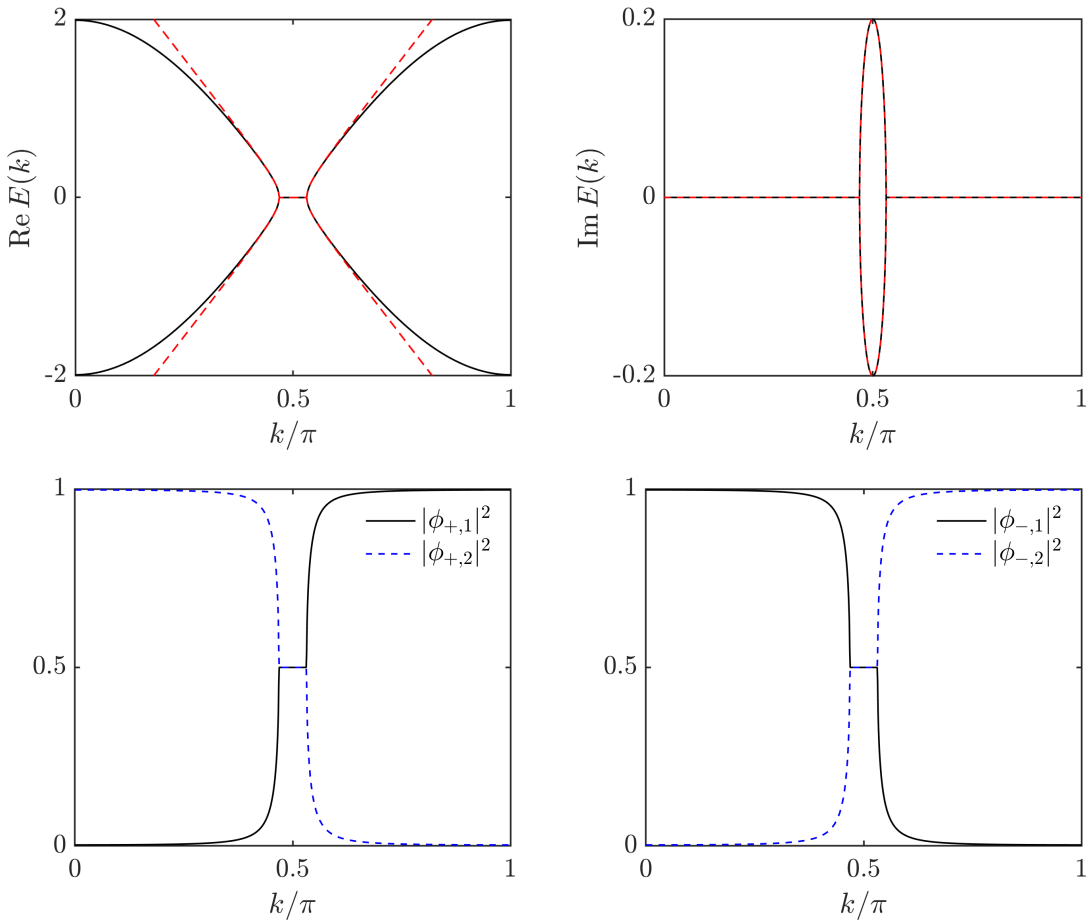


FIGURE 4.6: Top row: Real (left) and imaginary (right) parts of the dispersion relation (4.30) for $\Gamma = 0.2$. The red dashed line depicts the same quantities for the Taylor expansion of the Bloch Hamiltonian (4.29) around $k = \pi/2$. Bottom row: Modulus squared of the components of the eigenstates $\phi_\pm$ associated with $E_\pm(k)$.

where j is the lattice index; q_0 is the centre of the Gaussian; k_0 is the initial momentum; σ is the width parameter; and $\mathcal{N}$ is a normalisation constant, chosen so that $\sum_j |\psi(j)|^2 = 1$. The quasimomentum representation of this state is found to be

$$\psi(k) = \frac{\sqrt{\sigma}}{\pi^{1/4}} \frac{\theta_3\left(z, \mathrm{e}^{i\pi\tau}\right)}{\sqrt{\theta_3\left(-q_0\pi, \mathrm{e}^{i\pi\tau/2}\right)}} \mathrm{e}^{-\frac{\sigma^2}{2}(k-k_0)^2 - iq_0k}, \tag{4.32}$$

where $z = i\sigma^2\pi(k - k_0) - q_0\pi$, $\tau = 2i\sigma^2\pi$ and the Jacobi theta function $\theta_3(z, \mathrm{e}^{i\pi\tau})$ is defined as [135]

$$\theta_3\left(z, \mathrm{e}^{i\pi\tau}\right) = 1 + 2\sum_{n=1}^{\infty} \mathrm{e}^{i\pi\tau n^2} \cos\left(2nz\right). \tag{4.33}$$

Thus, $\psi(k)$ is the product of a Gaussian distribution in quasimomentum space and a

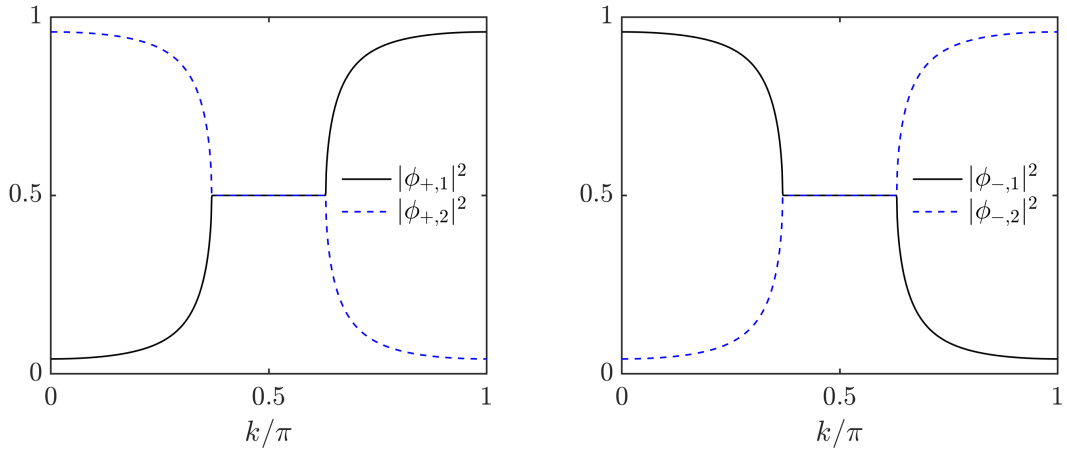


FIGURE 4.7: Modulus squared of the components of the eigenstates $\phi_\pm$ associated with $E_\pm(k)$ for $\Gamma = 0.8$.

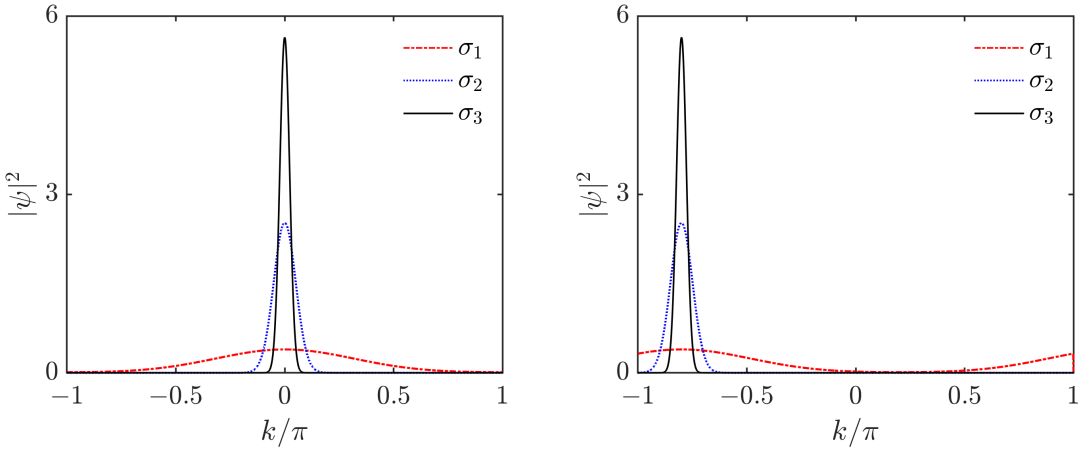


FIGURE 4.8: The modulus squared of the k-space representation of a Gaussian beam converges towards the 2π-periodic delta function as the width parameter σ increases. In both plots $q_0 = 0$, $\sigma_1 = \sqrt{0.5}$, $\sigma_2 = \sqrt{20}$ and $\sigma_3 = \sqrt{100}$. On the left $k_0 = 0$ and on the right $k_0 = -0.8\pi$.

term involving Jacobi theta functions. Using the properties of the theta function it is straightforward to check that $\psi(k + 2m\pi) = \psi(k)$ for any integer m. Furthermore, a broad Gaussian distribution in position space with $\sigma \to \infty$ yields a highly localised (2π-periodic) function in k-space such that $|\psi(k, 0)|^2 \to \delta_{2\pi}(k - k_0)$, as illustrated in Figure 4.8.

In order to obtain the two-component function $\Psi(k)$ we need to calculate $\psi(k+\pi)$. From (4.32) it follows that

$$\psi(k+\pi) = \frac{\sqrt{\sigma}}{\pi^{1/4}} \frac{\theta_2\left(z, \mathrm{e}^{i\pi\tau}\right)}{\sqrt{\theta_3\left(-q_0\pi, \mathrm{e}^{i\pi\tau/2}\right)}} \mathrm{e}^{-\frac{\sigma^2}{2}(k-k_0)^2 - iq_0k}, \tag{4.34}$$

where the theta function $\theta_2(z, \mathrm{e}^{i\pi\tau})$ is defined as

$$\theta_2(z, \mathrm{e}^{i\pi\tau}) = 2\mathrm{e}^{i\pi\tau/4} \sum_{n=0}^{\infty} \mathrm{e}^{i\pi\tau n(n+1)} \cos\left((2n+1)z\right) \tag{4.35}$$

and we made use of the relation

$$\theta_2(z, \mathrm{e}^{i\pi\tau}) = \mathrm{e}^{iz+i\pi\tau/4} \theta_3\left(z + \frac{1}{2}\pi\tau, \mathrm{e}^{i\pi\tau}\right). \tag{4.36}$$

Thus, $\Psi(k)$ may be written as

$$\Psi(k) = \frac{\sqrt{\sigma}}{\pi^{1/4}} \frac{\mathrm{e}^{-\frac{\sigma^2}{2}(k-k_0)^2 - iq_0k}}{\sqrt{\theta_3\left(-q_0\pi, \mathrm{e}^{i\pi\tau/2}\right)}} \begin{pmatrix} \theta_3\left(z, \mathrm{e}^{i\pi\tau}\right) \\ \theta_2\left(z, \mathrm{e}^{i\pi\tau}\right) \end{pmatrix}. \tag{4.37}$$

In the broad Gaussian limit $\sigma \to \infty$, τ tends to infinity along the imaginary axis and the two-components effectively become $(\theta_3(z, \mathrm{e}^{i\pi\tau}), \theta_2(z, \mathrm{e}^{i\pi\tau})) \to (1, 0)$. The two-component function $\Psi(k)$ then becomes a standard basis vector multiplied by a Gaussian wave packet that is highly localised around k_0. Thus, for example, a broad Gaussian beam in position space with momentum $k_0 = 0$ ($k_0 = \pi$) yields a $\Psi(k)$ that is approximately one of the eigenstates of the Bloch Hamiltonian at $k = 0$ ($k = \pi$) depicted in Figure 4.6.

If a static force is applied to the lattice a term $F\sum_j j|j\rangle\langle j|$ is added to the Hamiltonian (4.25). An initial state $\Psi(k)$ that is approximately an eigenstate of the Bloch Hamiltonian will then perform a non-Hermitian version of the famous Bloch oscillations (see, e.g., [140] or Appendix C). This is accompanied by transitions between the bands, which appear as a splitting of the beam in real space. An example of the resulting dynamics can be seen in the left frame of Figure 4.9 for $\Gamma = 0.2$, where time is measured in units of the Bloch period $T = 2\pi/F$. We observe that the Bloch oscillations sweep through the band structure depicted in Figure 4.6. Similar behaviour has been observed experimentally in

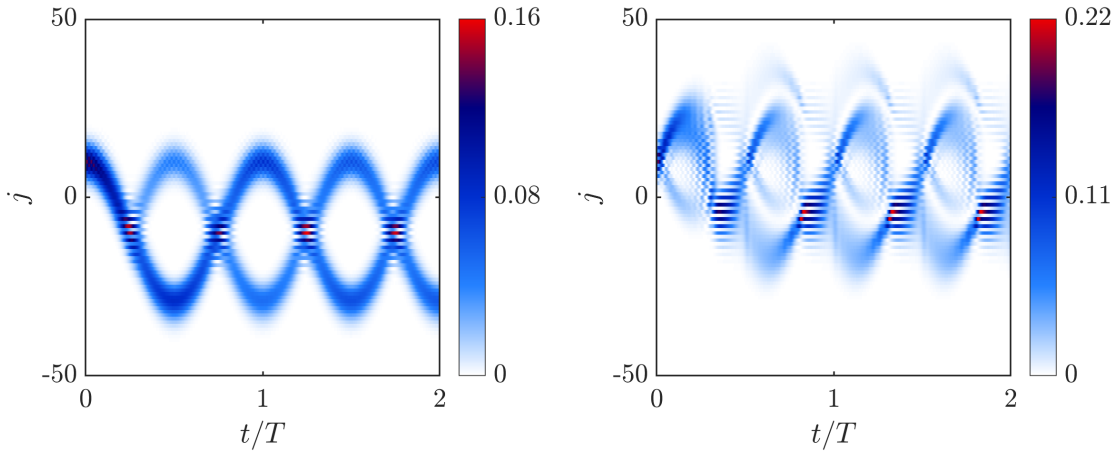


FIGURE 4.9: Time evolution of the renormalised density $|\psi_j|^2/|\psi|^2$ for an initial Gaussian wave packet in position space such that the two-component function $\Psi(k,0)$ is approximately a Bloch state (left) and is far from a Bloch state (right). The Gaussian parameters are $x_0 = 10$, $\sigma^2 = 20$, $k_0 = 0$ (left) and $k_0 = 0.3\pi$ (right). In both cases $F = 0.1$, with $\Gamma = 0.2$ (left) and $\Gamma = 0.8$ (right).

a system of optical fibre loops [129]. The right frame of the same figure demonstrates that the dynamics will fail to map out the band structure if $\Psi(k,0)$ is not approximately a Bloch state. In this particular case the gain/loss rate is set to $\Gamma = 0.8$ and $\psi(j,0)$ is a broad Gaussian beam in position space with $k_0 = 0.3\pi$. Thus $\Psi(k,0)$ is approximately a standard basis vector. However, in Figure 4.7 we see that neither of the eigenstates of the Bloch Hamiltonian are well approximated by a standard basis vector at $k = 0.3\pi$ when $\Gamma = 0.8$.

If $\Psi(k,0)$ is initialised in an approximate eigenstate of the Bloch Hamiltonian at $k = 0$ or $k = \pi$, then after half a Bloch period $t = T/2$ the populations of the two bands, i.e. the relative amplitudes of the two beams, are approximated by the Landau-Zener-type Hamiltonian (4.1). This can be understood in the following way. The static force introduces a term Fq into the two-component Hamiltonian (4.28)

$$h(k,q) = -2\cos k\sigma_z + i\Gamma\sigma_x + Fq, \tag{4.38}$$

where $q = id/dk$ is canonically conjugate to k with $[q, k] = i$. The expectation value of k evaluated in the two-component state $\Psi(k, t)$ is

$$\langle k \rangle_t = \frac{\int dk\, \Psi^\dagger(k,0) U^\dagger k U \Psi(k,0)}{\int dk\, \Psi^\dagger(k,0) U^\dagger U \Psi(k,0)}, \tag{4.39}$$

where we have defined the (non-unitary) time-evolution operator $U = \mathrm{e}^{-ih(k,q)t}$ and the integrals are over the interval $[-\pi/2, \pi/2]$. The Zassenhaus formula [141] enables the time-evolution operator to be factorised into the product $U = \mathrm{e}^{A(k)}\mathrm{e}^{-iFqt}$, with some matrix operator A that is independent of q, such that

$$\langle k \rangle_t = \frac{\int dk\, k \Psi^\dagger(k+Ft,0) \mathrm{e}^{A^\dagger(k)} \mathrm{e}^{A(k)} \Psi(k+Ft,0)}{\int dk\, \Psi^\dagger(k+Ft,0) \mathrm{e}^{A^\dagger(k)} \mathrm{e}^{A(k)} \Psi(k+Ft,0)}. \tag{4.40}$$

For a Gaussian in position space the two-component function $\Psi(k, 0)$ is given by equation (4.37), and in the broad beam limit the expectation value (4.40) reduces to

$$\langle k \rangle_t = \langle k \rangle_0 - Ft. \tag{4.41}$$

This is the acceleration theorem that is well known for Hermitian systems. In the non-Hermitian case this is only an approximation and relies on the initial quasimomentum uncertainty being negligible. It follows from the properties of the delta function that $\langle k \rangle_0 = 0$ when $k_0 = 0$ or $k_0 = \pi$.

In summary, if a static force is applied to the PT-symmetric chain (4.25), and $\Psi(k, 0)$ is approximately a Bloch state, then the dynamics can be described by the effectively time-dependent Bloch Hamiltonian (4.29), with the operator k replaced by its time-dependent expectation value $\langle k \rangle_t = \langle k \rangle_0 - Ft$. We can further Taylor expand the effective two-level system (4.29) around the band edge $k = \pi/2$, yielding

$$h(k) = \begin{pmatrix} 2\left(k - \frac{\pi}{2}\right) & i\Gamma \\ i\Gamma & -2\left(k - \frac{\pi}{2}\right) \end{pmatrix}. \tag{4.42}$$

The eigenvalues of the Taylor-expanded Hamiltonian are depicted in the top panel of Figure 4.6, in comparison to the exact eigenvalues for $\Gamma = 0.2$. We observe a good agreement of the eigenvalues close to the exceptional points. Making the substitution

$k \to \langle k \rangle_t$ and shifting the origin of time, results in a Hamiltonian of the form (4.1) with $\alpha \to 2F$ and $\gamma \to \Gamma$. The instantaneous eigenstates represent the two quasimomentum bands of the system. It follows from (4.24) that the transmission probability is

$$P_{\mathrm{tr}} = \left(2 - \mathrm{e}^{-\frac{\pi\Gamma^2}{2F}}\right)^{-1}. \tag{4.43}$$

Thus, if $\Psi(k, 0)$ is initialised in an approximate eigenstate of the Bloch Hamiltonian at $k = 0$ or $k = \pi$, then after half a Bloch period $t = T/2$ the populations of the two bands are approximated by (4.43).

This result agrees well with numerical calculations, as demonstrated in Figure 4.10 for an initial broad Gaussian beam. The time evolution of the renormalised density $|\psi_j|^2/|\psi|^2$ on each site j is plotted for $\Gamma = 0.2$ and three values of F. In each case the Bloch oscillations sweep through the band structure depicted in Figure 4.6. The data points in the bottom right panel were obtained by evolving the same initial state up to half the Bloch period for various values of F. Each point corresponds to the population in the upper branch of the beam in position space at $t = T/2$ for a particular F value. The agreement between the numerically observed transmission probability and the approximative formula (4.43) is excellent. This behaviour is observed for a wide range of parameters, as long as the two beams splitting at the exceptional point can be meaningfully distinguished. We expect the experimental observation of this transition, due to sweeping through exceptional points, to be entirely within reach.

Finally, let us attempt to gain some insight into the oscillatory behaviour of the beam in position space. For instance, as observed in the left panel of Figure 4.9. For this purpose we consider a single-band approximation and demonstrate that the motion of the beam in position space can be linked to the semiclassical dynamics of narrow momentum Gaussian wave packets. The single-band approximation is derived from the eigenvalues of the Hamiltonian (4.38), which are readily found to be

$$\xi_{\pm}(q, k) = Fq + E_{\pm}(k). \tag{4.44}$$

Here we have again identified the coordinate $q = id/dk$ canonically conjugate to k and

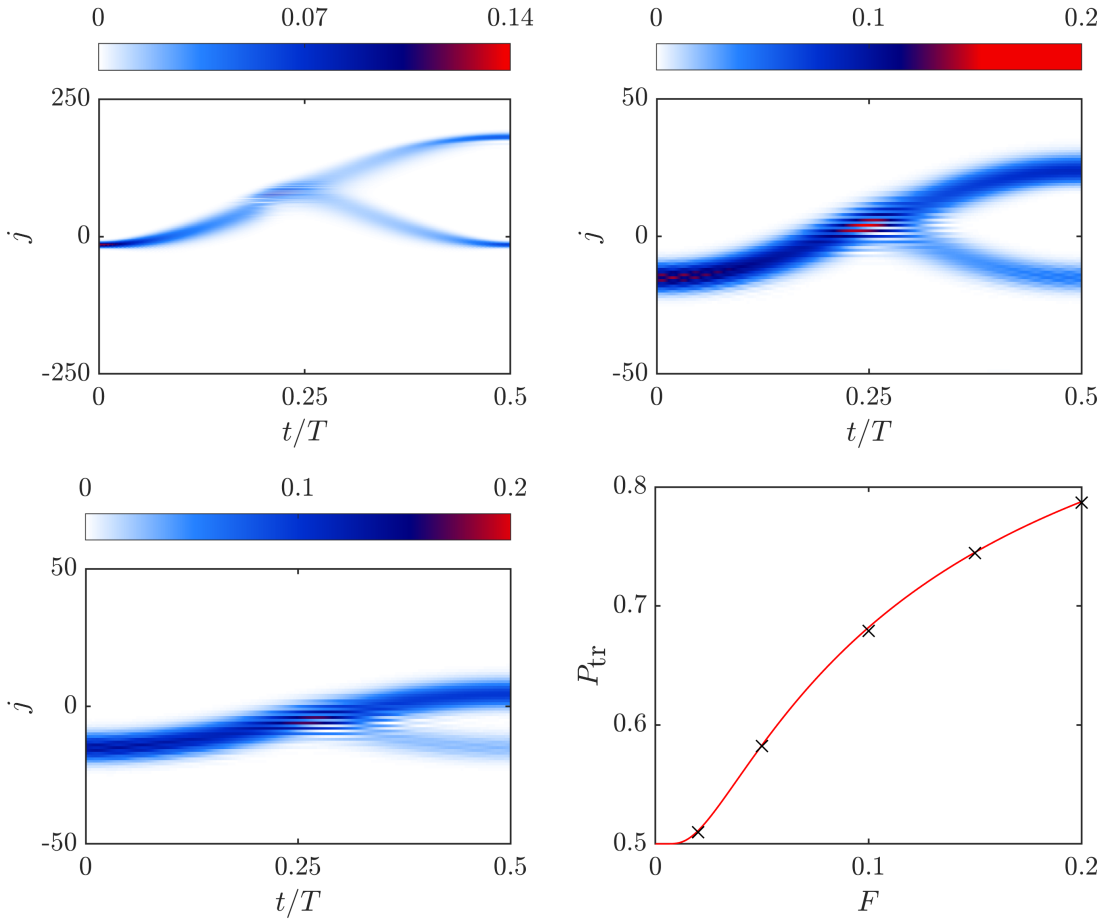


FIGURE 4.10: Time evolution of the renormalised density for an initial Gaussian wave packet in position space with centre $x_0 = -15$, momentum $k_0 = \pi$ and width $\sigma^2 = 20$, for $\Gamma = 0.2$ and different values of F ($F = 0.02$ top left, $F = 0.1$ top right, and $F = 0.2$ bottom left). The bottom right panel shows the transmission probability for $\Gamma = 0.2$ as a function of F (red). The crosses are numerical values of the transmitted fraction, obtained by evaluating the population in the upper branch of the beam in position space at $t = T/2$, where the Bloch period $T = 2\pi/F$.

$E_\pm(k)$ is the field-free dispersion relation (4.30), i.e., $E_\pm(k)$ are the eigenvalues of the Bloch Hamiltonian (4.29). In the single-band approximation the population in each band $\pm$ is assumed to evolve independently under the non-Hermitian Hamiltonian $\xi_\pm(q, k)$. Thus, as the coupling between the bands is ignored, this approximation cannot account for any population transfer between the bands. Note that the q and k are different in the $\pm$ bands, so that technically we should write $E_\pm(q_\pm, k_\pm)$. However, for notational simplicity we do not explicitly indicate this, as it should be clear from the context which band is being referred to.

Recall from Chapter 3 that the semiclassical dynamics of a Gaussian wave packet generated by a non-Hermitian phase-space Hamiltonian $H(q,k) = \mathrm{Re}\, H + i\, \mathrm{Im}\, H$ are given by

$$\dot{q} \quad = \partial_k \,\mathrm{Re}\, H + \Sigma_{qk}\partial_k \,\mathrm{Im}\, H + \Sigma_{qq}\partial_q \,\mathrm{Im}\, H, \tag{4.45}$$

$$\dot{k} \quad = -\partial_q \,\mathrm{Re}\, H + \Sigma_{kk}\partial_k \,\mathrm{Im}\, H + \Sigma_{qk}\partial_q \,\mathrm{Im}\, H, \tag{4.46}$$

where Σ encodes the (co)variances of the canonical coordinates according to

$$\Sigma_{qq} = 2(\Delta q)^2, \quad \Sigma_{kk} = 2(\Delta k)^2, \quad \Sigma_{qk} = \Sigma_{kq} = 2\Delta_{qk}, \tag{4.47}$$

and the determinant of Σ is one. The covariances are also time dependent, following the dynamical equations

$$\dot{\Sigma} = \Omega\,\mathrm{Re}\, H''\Sigma - \Sigma\,\mathrm{Re}\, H''\Omega + \Omega\,\mathrm{Im}\, H''\Omega + \Sigma\,\mathrm{Im}\, H''\Sigma, \tag{4.48}$$

where Ω is the symplectic matrix

$$\Omega = \begin{pmatrix} 0 & 1 \\ -1 & 0 \end{pmatrix} \tag{4.49}$$

and H'' is the Hessian of H.

In order to make progress we must distinguish between the regions of k-space where the square root $\sqrt{4\cos^2 k - \Gamma^2}$ appearing in $E_\pm(k)$ is real or imaginary. In the region where it is real we find

$$\mathrm{Re}\,\xi_\pm = Fq + E_\pm(k), \quad \mathrm{Im}\,\xi_\pm = 0, \tag{4.50}$$

while in the region where it is imaginary

$$\mathrm{Re}\,\xi_\pm = Fq, \quad \mathrm{Im}\,\xi_\pm = \pm\sqrt{\Gamma^2 - 4\cos^2 k}. \tag{4.51}$$

An application of the semiclassical equations (4.45), (4.46) and (4.48) in the region where the square root is real yields

$$\dot{q} = \partial_k E_\pm(k), \quad \dot{k} = -F, \tag{4.52}$$

and

$$\dot{\Sigma}_{qq} = 2\Sigma_{qk}\partial_{kk}E_\pm(k), \quad \dot{\Sigma}_{qk} = \Sigma_{kk}\partial_{kk}E_\pm(k), \quad \dot{\Sigma}_{kk} = 0. \tag{4.53}$$

Similarly, in the region where the square root is imaginary,

$$\dot{q} = \Sigma_{qk}\partial_k \operatorname{Im}\xi_\pm, \quad \dot{k} = -F + \Sigma_{kk}\partial_k \operatorname{Im}\xi_\pm, \tag{4.54}$$

and

$$\dot{\Sigma}_{qq} = \left(\Sigma_{qk}^2 - 1\right)\partial_{kk}\operatorname{Im}\xi_\pm, \quad \dot{\Sigma}_{qk} = \Sigma_{qk}\Sigma_{kk}\partial_{kk}\operatorname{Im}\xi_\pm, \quad \dot{\Sigma}_{kk} = \Sigma_{kk}^2\partial_{kk}\operatorname{Im}\xi_\pm, \tag{4.55}$$

where $\operatorname{Im}\xi_\pm$ is defined in (4.51). Now observe that in the approximation of an initially infinitely narrow momentum wave packet with $\Sigma_{kk}(0) = 0$, the (co)variances remain constant for all times, i.e., $\Sigma_{kk}(t) = 0$ and $\Sigma_{qk}(t) = \Sigma_{qk}(0)$. In this case the equations of motion simplify to

$$\dot{q} = \partial_k E_\pm(k), \quad \dot{k} = -F \tag{4.56}$$

in the region where the square root is real, and

$$\dot{q} = \Sigma_{qk}(0)\partial_k \operatorname{Im}\xi_\pm, \quad \dot{k} = -F \tag{4.57}$$

in the region where the square root is imaginary. The acceleration theorem $k(t) = -Ft + k(0)$ is recovered in both regions, while

$$q(t) = q(0) - \frac{1}{F}\left[E_\pm(k(t)) - E_\pm(k(0))\right] \tag{4.58}$$

in the real region and

$$q(t) = q(0) + \frac{i}{F}\Sigma_{qk}(0)\left[E_\pm(k(t)) - E_\pm(k(0))\right] \tag{4.59}$$

in the imaginary region. In the special case where $\Sigma_{qk}(0) = 0$, the position of each wave packet follows the real dispersion relation in the unbroken PT-symmetry phase and remains stationary in the broken phase. Therefore, as observed in Figure 4.10, the position maps out the real part of the band structure of the Bloch Hamiltonian.

4.6 Summary

We have investigated a two-level system driven through two consecutive exceptional points adiabatically and at finite speed. In the adiabatic limit this leads to behaviour having no analogue in the Hermitian case. The population is equally distributed between the states coalescing in the exceptional point, corresponding to a loss of information of the initial state. In the limit of fast driving, the familiar quantum quench behaviour is recovered. We have derived an analytic expression for the population transfer for arbitrary speed of parameter variation, interpolating between these two extremes. We observed that the backward temporal evolution exhibits a strong sensitivity to perturbations in the backwards-time Hamiltonian, suggesting that this model could be useful to study the relationship between exceptional points and quantum chaos.

Finally, we demonstrated how the model can be experimentally investigated in a PT-symmetric lattice using Bloch oscillations, such as an optical waveguide setup, providing new opportunities for engineering beam dynamics. We note that the exceptional points of the two-level Hamiltonian (4.1) form a set of measure zero, and in practice the exceptional points will never be hit. A benefit of the experimental realisation proposed here is that the exceptional points appear in the band structure of the Bloch Hamiltonian. Although the exceptional points move when the parameters are slightly changed, the system is driven through them when the quasimomentum varies continuously according to the acceleration theorem. In practice, if the PT-symmetry is broken, e.g. due to unequal gain/loss rates on different lattice sites, then there are no exceptional points. However, we find that the associated effects are still observable (see Figure 5.4 in Chapter 5). In the next chapter we explore the possibility of realising this PT-symmetric system in a dissipative quantum system described by the Lindblad equation.

Chapter 5

Bloch oscillations in a Bose-Hubbard chain with single-particle losses

In recent years there has been great interest in the dynamics of ultracold atoms and BECs trapped in an optical lattice with a static tilt [43, 142–144]. The application of a tilt can cause the atoms to undergo Bloch oscillations, as has been demonstrated, for example, in remarkable experiments with one and two bosonic atoms [145]. A BEC of weakly-interacting particles also exhibits Bloch oscillations. Although this behaviour can dramatically change when the particle interaction strength increases [146]. In a full many-particle treatment, a system of ultracold atoms in a tilted optical lattice with $M = 2L + 1$ lattice sites can be described by the Bose-Hubbard Hamiltonian

$$\hat{H} = -\sum_{j=-L}^{L-1} \left(\hat{a}_{j+1}^{\dagger} \hat{a}_j + \hat{a}_j^{\dagger} \hat{a}_{j+1} \right) + \frac{U}{2} \sum_{j=-L}^{L} \hat{n}_j \left(\hat{n}_j - 1 \right) + F \sum_{j=-L}^{L} j \hat{n}_j, \tag{5.1}$$

where $F \in \mathbb{R}$ describes the lattice tilt. For simplicity we will work with units where the coupling constant $J = 1$.

In this chapter we consider the effects of localised single-particle losses from the odd sites of the lattice. As briefly discussed in Chapter 1, this type of dissipative process can be described by Lindblad operators of the form $\hat{L}_j \propto \hat{a}_j$. Here we assume that the decay rate γ is the same on each dissipative lattice site and take $\hat{L}_j = \sqrt{4\gamma}\hat{a}_j$, where the factor

of four is included to make the resulting expressions correspond to those in the previous chapter. The Lindblad equation (1.4) then has the form

$$\frac{d}{dt}\hat{\rho} = -i\left(\hat{H}_{\text{eff}}\hat{\rho} - \hat{\rho}\hat{H}_{\text{eff}}^{\dagger}\right) - 2\gamma \sum_{j=-L}^{L} \left((-1)^j - 1\right) \hat{a}_j \hat{\rho} \hat{a}_j^{\dagger}, \tag{5.2}$$

where the effective Hamiltonian is defined as

$$\hat{H}_{\text{eff}} = \hat{H} + i\gamma \sum_{j=-L}^{L} \left((-1)^j - 1\right) \hat{n}_j \tag{5.3}$$

with $\hat{H}$ being the Bose-Hubbard Hamiltonian (5.1). The effective Hamiltonian has passive PT-symmetry and, for a single particle system, it reduces to the PT-symmetric Hamiltonian analysed in Chapter 4 up to an overall decay term.

In the case of a single particle we show that the time evolution of the state $\hat{\rho}$ is completely determined by $\hat{H}_{\text{eff}}$, so that the single particle system may be viewed as a quantum implementation of the PT-symmetric Hamiltonian (4.25) with a static tilt. The spectral properties of $\hat{H}_{\text{eff}}$ are analysed for an infinite lattice and features in the spectrum are linked to observable dynamical effects.

We then consider the mean-field limit of a many-particle system. Using the general semiclassical structure presented in Chapter 3 we find that the mean-field dynamics are described by a complex discrete nonlinear Schrödinger equation with nonlinear (passive) PT-symmetry. Nonlinear PT-symmetric systems can have properties quite unlike their linear counterparts and are a subject of recent research interest. They appear naturally in models of BECs in PT-symmetric potentials [147–149], as well as in the context of classical wave systems [150] and nonlinear optics [151, 152]. Analytic expressions are derived for the generalised nonlinear stationary states and the nonlinear Bloch bands. The interplay of nonlinearity and particle losses is found to lead to peculiar features in the nonlinear Bloch bands, such as the vanishing of solutions and the formation of additional exceptional points. The stability of the stationary states is determined via the Bogoliubov-de Gennes equation and connected to features in the mean-field dynamics. Surprisingly, the stability of the nonlinear Bloch bands appears to influence the quantum

dynamics even far from the mean-field limit. This is demonstrated numerically for a two-particle system.

5.1 Single-particle system

5.1.1 State evolution

We begin this chapter with an analysis of a single-particle system. Let us first consider the time evolution of the quantum state $\hat{\rho}$. For a single particle the time evolution of $\hat{\rho}$ is completely determined by the effective Hamiltonian (5.3). To see this, consider the expansion of the density operator in the basis $\{|i\rangle, |v\rangle\}$,

$$\hat{\rho} = \sum_{i,j} \rho_{ij}|i\rangle\langle j| + \sum_{i} \rho_{iv}|i\rangle\langle v| + \sum_{i} \bar{\rho}_{iv}|v\rangle\langle i| + \rho_{vv}|v\rangle\langle v|, \tag{5.4}$$

where $|i\rangle$ is a Fock state corresponding to a single particle on the i^{th} lattice site and $|v\rangle$ is the vacuum state. Inserting this expansion into the Lindblad equation (5.2) yields the equations of motion for the matrix elements

$$i\dot{\rho}_{ij} = \left[\hat{H}_{\text{eff}}\hat{\rho} - \hat{\rho}\hat{H}_{\text{eff}}^{\dagger}\right]_{ij}, \quad i\dot{\rho}_{jv} = \left[\hat{H}_{\text{eff}}\hat{\rho}\right]_{jv}, \quad i\dot{\rho}_{vv} = -2i\gamma \sum_{j} \left((-1)^{j} - 1\right) \rho_{jj}. \tag{5.5}$$

By defining the components of the vector ψ via $\rho_{ij} = \psi_i \bar{\psi}_j$ it is straightforward to verify from the first equation above that the evolution of ψ is governed by the non-Hermitian Schrödinger equation

$$i\dot{\psi} = H_{\text{eff}}\,\psi, \tag{5.6}$$

where H_{eff} is the effective Hamiltonian (5.3) represented in the basis $\{|j\rangle\}$. In what follows it is convenient to express the single-particle effective Hamiltonian in terms of the basis states $\{|j\rangle\}$ as

$$\hat{H}_{\text{eff}} = \sum_{j=-L}^{L} -\left(|j+1\rangle\langle j| + |j\rangle\langle j+1|\right) + Fj|j\rangle\langle j| + i\gamma\left((-1)^{j} - 1\right)|j\rangle\langle j|. \tag{5.7}$$

Writing out the non-Hermitian Schrödinger equation (5.6) explicitly yields the equations of motion for the components

$$i\dot{\psi}_j = -\left(\psi_{j+1} + \psi_{j-1}\right) + Fj\psi_j + i\gamma\left((-1)^j - 1\right)\psi_j. \tag{5.8}$$

Furthermore, by defining the vector $\eta = (\rho_{1v}, \ldots, \rho_{Mv})^T$ we see that the time evolution of $\hat{\rho}$ is given by

$$\rho_{ij}(t) = \psi_i(t)\bar{\psi}_j(t), \quad \eta(t) = \mathrm{e}^{-iH_{\mathrm{eff}}t}\eta(0) \quad \text{and} \quad \rho_{vv}(t) = 1 - |\psi(t)|^2, \tag{5.9}$$

where the expression for $\rho_{vv}(t)$ follows from the trace preservation of the Lindblad equation. In general, knowing only the time evolution of the components ρ_{ij} is not sufficient to recover the time evolution of the density matrix. However, we see that if

$$\rho_{jv}(0) = 0, \quad \forall j \tag{5.10}$$

then the vector $\eta(t)$ is zero for all time and the time evolution of the density matrix is described by the elements ρ_{ij} alone, and thus by the wavefunction ψ. The condition (5.10) holds for the initial states considered in this section.

5.1.2 Spectral properties

We now consider the spectral properties of the effective Hamiltonian (5.7) with an infinite lattice and show that the spectrum generally consists of two ladders of eigenvalues. The analysis in this section closely follows [153], in which the authors investigate the Bose-Hubbard Hamiltonian with the additional terms $\sum_j \epsilon(-1)^j \hat{a}_j^\dagger \hat{a}_j$ (assumed to be zero in our model). There, the ground state energies of the lattice sites are alternately increased or decreased and $\epsilon > 0$ is the energy difference between neighbouring sites.

In a similar vein to [153], we introduce the complex conjugation operator $\hat{C}$ and the translation operator $\hat{T}_m = \sum_j |j-m\rangle\langle j|$, which shifts the lattice by m sites to the left. A short calculation shows that this pair of operators satisfy the following commutation

relations

$$\left[\hat{T}_m, \hat{H}_{\text{eff}}\right] = i\gamma \sum_{j=-\infty}^{+\infty} (-1)^j \left(1-(-1)^m\right) |j-m\rangle\langle j| + mF \sum_{j=-\infty}^{+\infty} |j-m\rangle\langle j|, \tag{5.11}$$

$$\left[\hat{C}, \hat{H}_{\text{eff}}\right] = -2i\gamma \sum_{j=-\infty}^{+\infty} \left((-1)^j - 1\right) |j\rangle\langle j|\hat{C}, \tag{5.12}$$

$$\left[\hat{T}_m, \hat{C}\right] = 0. \tag{5.13}$$

Let $|\lambda\rangle$ be an eigenvector of $\hat{H}_{\text{eff}}$ with the eigenvalue $\lambda(F,\gamma)$ so that

$$\hat{H}_{\text{eff}}|\lambda\rangle = \lambda(F,\gamma)\,|\lambda\rangle. \tag{5.14}$$

To simplify the notation we temporarily drop the functional dependence of $\lambda(F,\gamma)$ on the system parameters. Using the commutation relations above it can be shown that

$$\begin{aligned} \hat{H}_{\text{eff}}\left[\hat{T}_{2l}|\lambda\rangle\right] &= \left(\lambda - 2lF\right)\left[\hat{T}_{2l}|\lambda\rangle\right], \\ \hat{H}_{\text{eff}}\left[\hat{T}_{2l+1}\hat{C}|\lambda\rangle\right] &= \left(\bar{\lambda} - (2l+1)F - 2i\gamma\right)\left[\hat{T}_{2l+1}\hat{C}|\lambda\rangle\right], \end{aligned} \tag{5.15}$$

where $l \in \mathbb{Z}$. An application of the operators $\hat{T}_{2l}$ and $\hat{T}_{2l+1}\hat{C}$ to the eigenvector $|\lambda\rangle$ then yields the ladders of eigenvectors

$$\hat{H}_{\text{eff}}|E_{\alpha,n}\rangle = E_{\alpha,n}|E_{\alpha,n}\rangle, \tag{5.16}$$

where $\alpha = 0, 1$ labels the ladder, and the states

$$|E_{0,n}\rangle = \hat{T}_{-2n}|\lambda\rangle, \quad |E_{1,n}\rangle = \hat{C}\hat{T}_{-(2n+1)}|\lambda\rangle \tag{5.17}$$

are associated with the energies

$$E_{0,n} = \operatorname{Re}\lambda + 2nF + i\operatorname{Im}\lambda, \tag{5.18}$$

$$E_{1,n} = \operatorname{Re}\lambda + (2n+1)F - i\operatorname{Im}\lambda - 2i\gamma. \tag{5.19}$$

The expressions for these energies can be simplified by considering the operator

$$\hat{X} = \sum_j (-1)^j |-j\rangle\langle j|, \tag{5.20}$$

which connects $\hat{H}_{\text{eff}}$ to its adjoint

$$\hat{X}\hat{H}_{\text{eff}} = -\hat{H}_{\text{eff}}^\dagger \hat{X}. \tag{5.21}$$

By acting on the eigenvalue equation (5.16) with $\hat{X}$ one can show that $\hat{X}|E_{\alpha,n}\rangle$ is an eigenvector of $\hat{H}_{\text{eff}}^\dagger$ with eigenvalue $-E_{\alpha,n}$ and the spectrum of $\hat{H}_{\text{eff}}^\dagger$ may be written as

$$S = \{-\operatorname{Re}\lambda - i\operatorname{Im}\lambda, -\operatorname{Re}\lambda + i\operatorname{Im}\lambda + 2i\gamma - F\} \tag{5.22}$$

modulo $2F$. However, the eigenvalues of $\hat{H}_{\text{eff}}^\dagger$ can also be put into correspondence with the complex conjugate eigenvalues of $\hat{H}_{\text{eff}}$, that is,

$$S = \{\operatorname{Re}\lambda - i\operatorname{Im}\lambda, \operatorname{Re}\lambda + i\operatorname{Im}\lambda + 2i\gamma + F\} \tag{5.23}$$

modulo $2F$. Equality of the sets (5.22) and (5.23) implies that $\operatorname{Re}\lambda = 0$, and the energies in (5.18) and (5.19) simplify to

$$E_{0,n} = 2nF + i\operatorname{Im}\lambda\,(F,\gamma)\,, \tag{5.24}$$

$$E_{1,n} = (2n+1)F - i\operatorname{Im}\lambda\,(F,\gamma) - 2i\gamma. \tag{5.25}$$

Thus, the spectrum of $\hat{H}_{\text{eff}}$ generally consists of two energy ladders. The real part has values centred around $\operatorname{Re}E = 0$, with equal spacings of size F, while the imaginary part of each ladder is fixed and independent of n. The real and imaginary parts of the spectrum are shown in Figure 5.1 for two different values of F. The eigenvalues were obtained from numerical simulations in a lattice of size $M = 201$ and eigenvalues due to the finite lattice size were discarded.

The equidistance of the real parts of the eigenvalues give rise to periodic dynamics. In the absence of losses, it is well known that the dynamics are periodic with the so-called

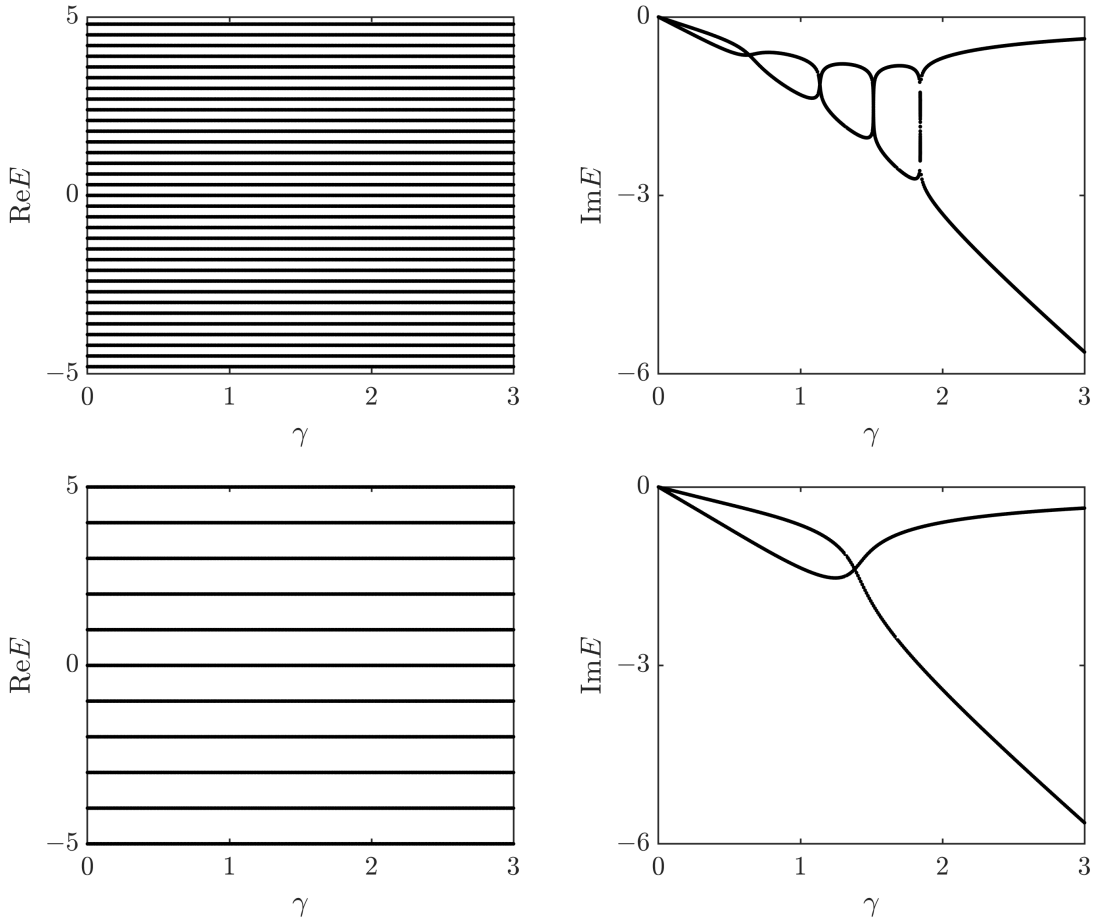


FIGURE 5.1: Real (left) and imaginary (right) parts of the eigenvalues of the effective Hamiltonian as a function of the decay rate γ for a fixed static tilt $F = 0.3$ (top row) and $F = 1$ (bottom row).

Bloch period $T = 2\pi/F$ (see, e.g., [140]). When particle losses are present, the separation of the imaginary parts of the energy means that one of the energy ladders decays faster than the other. This has observable consequences. For instance, when $\gamma = 0$ a single particle initialised on a single lattice site $|\Psi(0)\rangle = |j\rangle$ performs left-right symmetric Bloch oscillations with a time period T [140]. However, when $\gamma \neq 0$ the decay of one of the ladders eventually leads to an effective frequency doubling of the system, resulting in an additional breathing mode of reduced width. This effect is illustrated in Figure 5.2, where the renormalised density $|\psi_j|^2/|\psi|^2$ on each lattice site j is shown for both the unitary and dissipative time evolution.

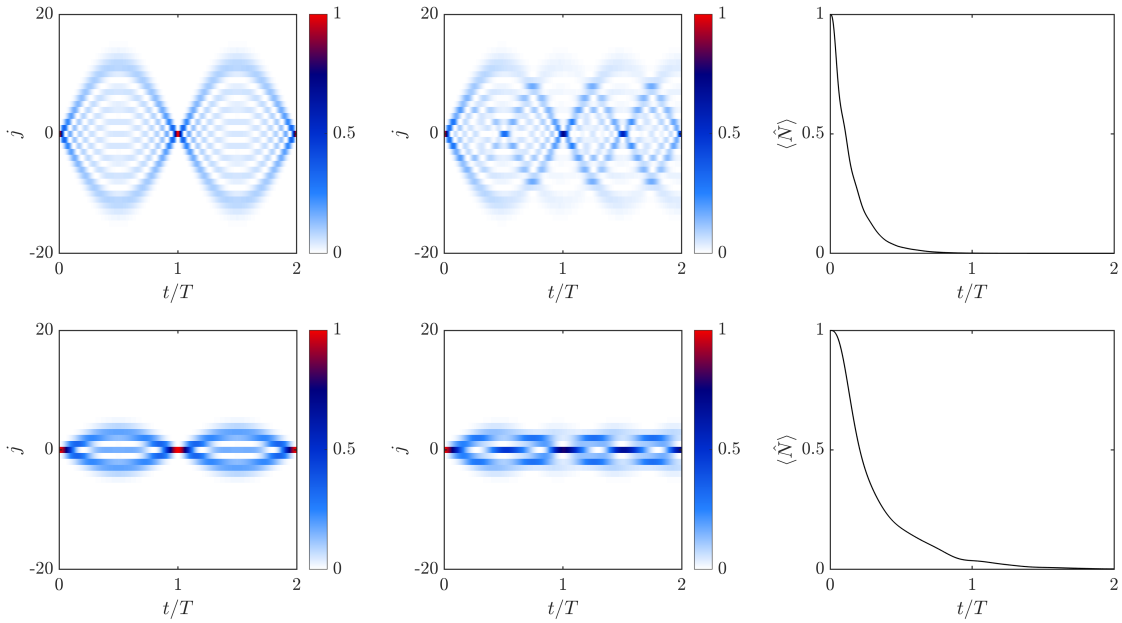


FIGURE 5.2: The renormalised density is plotted as a function of time for a single particle initialised on the central lattice site $j = 0$, with a static tilt $F = 0.3$ (top row) and $F = 1$ (bottom row). The unitary dynamics $\gamma = 0$ are plotted in the left column. The dissipative dynamics with $\gamma = 0.2$ and $\gamma = 0.4$ are shown in the middle column of the top and bottom rows respectively. The particle number expectation value dynamics are depicted in the right column for the dissipative cases.

5.1.3 Bloch oscillations of a broad Gaussian state

The single-particle effective Hamiltonian (5.7) is equivalent to the PT-symmetric tight-binding Hamiltonian (4.25) considered in Chapter 4 up to an overall decay. Thus, the previous results on non-Hermitian Bloch oscillations of Gaussian wave packets also apply here. In complete analogy with Chapter 4, we can make use of the quasimomentum representation and introduce a two-component wavefunction $\Psi(k)$. This obeys the equation of motion $i\dot{\Psi}(k) = h(k, q)\Psi(k)$, with the two-component Hamiltonian

$$h(k, q) = -2\cos k\sigma_z + i\gamma\sigma_x + Fq - i\gamma. \tag{5.26}$$

Observe that (5.26) is simply (4.38) with an additional overall decay $-i\gamma$. One can then determine the dispersion relation from $h(k, q)$ with $F = 0$. However, we instead reformulate the problem in a way that can also be applied to the many-particle mean-field dynamics considered later in the chapter.

With $F = 0$, we separate the equations of motion for the wave function components in the $\{|j\rangle\}$ basis, ψ_j (5.8), into even and odd lattice sites

$$i\dot{\psi}_{2j} = -\left(\psi_{2j+1} + \psi_{2j-1}\right), \tag{5.27}$$

$$i\dot{\psi}_{2j-1} = -\left(\psi_{2j} + \psi_{2j-2}\right) - 2i\gamma\psi_{2j-1}. \tag{5.28}$$

The translational symmetry of the system motivates the ansatz

$$\psi_{2j} = A\mathrm{e}^{ik(2j)-iEt}, \quad \psi_{2j-1} = B\mathrm{e}^{ik(2j-1)-iEt} \tag{5.29}$$

for the even and odd components, with $-\pi \leq k \leq \pi$. Substituting these expressions into the equations of motion (5.27) and (5.28) yields the pair of equations for A and B,

$$\begin{pmatrix} 0 & -2\cos k \\ -2\cos k & -2i\gamma \end{pmatrix} \begin{pmatrix} A \\ B \end{pmatrix} = E \begin{pmatrix} A \\ B \end{pmatrix}, \tag{5.30}$$

which can be interpreted as an eigenvalue equation. From this eigenvalue equation it is straightforward to obtain the field-free dispersion relation

$$E(k) = -i\gamma \pm \sqrt{4\cos^2 k - \gamma^2}, \tag{5.31}$$

which matches that of the PT-symmetric system (4.30) apart from an overall imaginary term $-i\gamma$. The band structure is illustrated in Figure 5.3. When $\gamma < 2$ there are exceptional points at $2|\cos k| = \gamma$, and for values of the quasimomentum $2|\cos k| > \gamma$ the energy has a real part. At the exceptional points the passive PT-symmetry breaks and for $2|\cos k| < \gamma$ the energy becomes purely imaginary. For $\gamma \geq 2$ the bands are purely imaginary for all values of the quasimomentum.

Let us now consider the dynamics of an initial Gaussian wave packet

$$|\Psi(0)\rangle = \mathcal{N} \sum_{j=-L}^{L} \mathrm{e}^{-(j-q_0)^2/2\sigma^2 + ik_0(j-q_0)}|j\rangle, \tag{5.32}$$

where q_0 is the centre of the Gaussian; k_0 is the initial momentum; σ is the width parameter; and $\mathcal{N}$ is a normalisation constant. As discussed at length in Chapter 4, an

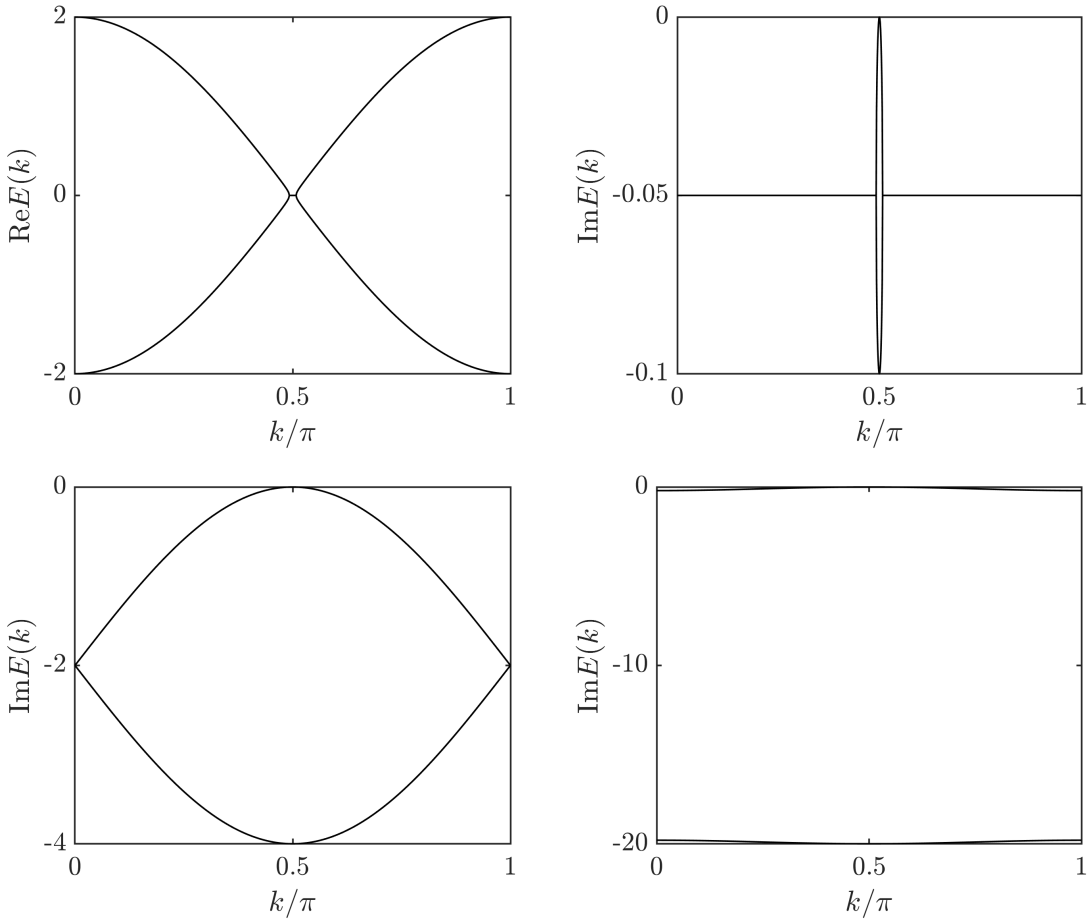


FIGURE 5.3: (Top row) Real (left) and imaginary (right) parts of the dispersion relation (5.31) for $\gamma = 0.05$. (Bottom row) The band structure is purely imaginary for $\gamma \geq 2$. On the left $\gamma = 2$ and on the right $\gamma = 10$.

application of a lattice tilt F can result in Bloch oscillations, together with a splitting of the beam in real space due to a transfer of population between the Bloch bands. This is illustrated in the left frame of Figure 5.4 for $\gamma = 0.05$ and $F = 0.2$, where the Gaussian wave packet effectively maps out the real part of the band structure depicted in Figure 5.3. Numerical simulations show that this behaviour does not require the decay rate to be exactly the same on each dissipative site. This can be seen in the middle panel of Figure 5.4, where the decay rates on the dissipative sites γ_j are randomly selected from the interval $(0.025, 0.125)$.

We finally comment on the perhaps counterintuitive result that increasing the decay rate γ on each lattice site can inhibit particle loss. This is illustrated in Figure 5.5 for an initial Gaussian wave packet. As γ is increased towards the critical value $\gamma = 2$ the

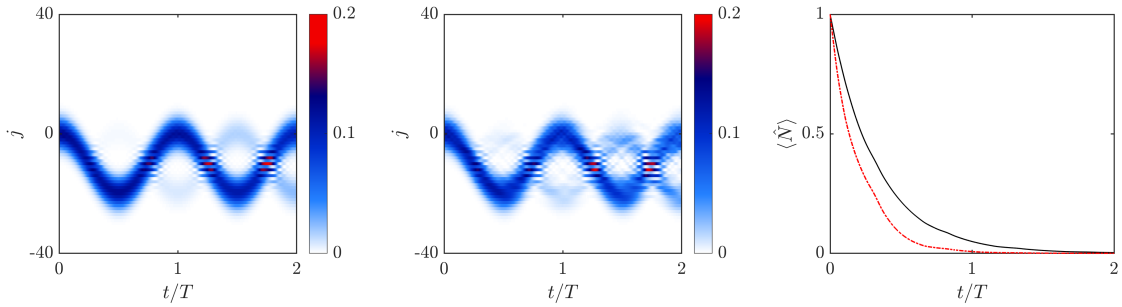


FIGURE 5.4: The renormalised number density is plotted as a function of time for an initial Gaussian wave packet in position space with $q_0 = 0$, $k_0 = 0$, $\sigma = \sqrt{20}$ and $F = 0.2$. Results are shown for $\gamma = 0.05$ (left) and γ_j randomly chosen from the interval $(0.025, 0.125)$ (middle). The right frame shows the total particle number dynamics for $\gamma = 0.05$ (black solid) and the randomised decay rates (red dashed).

total particle number decays faster. However, increasing γ beyond this value leads to a slowing down of the decay. This can be understood from the band structure in the bottom right frame of Figure 5.3, where a large γ leads to a quasi-stable band and a rapidly decaying band. For large γ, Bloch oscillations are no longer present and instead the density localises onto the stable lattice sites. In fact, the absence of Bloch oscillations is predicted by the semiclassical dynamics (4.59) derived in the previous chapter. In this case $\mathrm{Re}E = 0$ and the centre of the Gaussian is constant $q = q(0)$.

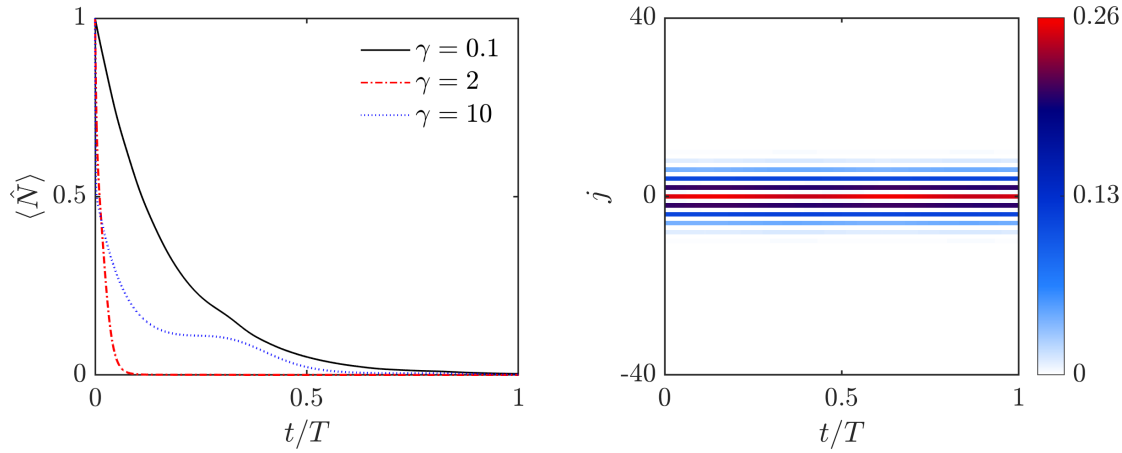


FIGURE 5.5: (Left) Particle number expectation value dynamics for an initial Gaussian wave packet in position space with $q_0 = 0$, $k_0 = 0$ and $\sigma = \sqrt{20}$. Several different values of γ are shown with $F = 0.2$. (Right) The renormalised number density for the case $\gamma = 10$.

5.2 Mean-field limit of a many-particle system

Let us now consider the time evolution of a pure BEC (1.28), defined in Chapter 1 as

$$|\Psi(0)\rangle = \frac{1}{\sqrt{N_0!}}\left(\sum_{j=-L}^{L}\psi_j\hat{a}_j^\dagger\right)^{N_0}|v\rangle, \tag{5.33}$$

where N_0 is the initial number of particles. A far richer set of dynamics are expected to be possible for many-particle systems, owing to the interplay between particle interactions and dissipation. However, for many particles on a large lattice the size of the Hilbert space prohibits numerical investigations. Thus, to obtain insights into the case of large particle numbers we consider the mean-field limit $N_0 \to \infty$. This is expected to be valid provided that the state remains close to a pure BEC.

The mean-field equations of motion may be obtained from the general dissipative phase-space dynamics (3.35) derived in Chapter 3. To this end, we note that the Weyl symbol of the Bose-Hubbard Hamiltonian (5.1) is

$$H = -\sum_{j=-L}^{L-1}\left(\bar{a}_{j+1}a_j + \bar{a}_j a_{j+1}\right) + \frac{U}{2}\sum_{j=-L}^{L}\left(|a_j|^4 - 2|a_j|^2\right) + F\sum_{j=-L}^{L} j|a_j|^2, \tag{5.34}$$

up to an overall constant term. Inserting this, and the Weyl symbols of the Lindblad operators $L_j = \sqrt{4\gamma}a_j$, into the equation of motion for $\dot{a}_j$ (3.35) then yields

$$i\dot{\psi}_j = -\left(\psi_{j+1} + \psi_{j-1}\right) + Fj\psi_j + g|\psi_j|^2\psi_j + i\gamma\left((-1)^j - 1\right)\psi_j. \tag{5.35}$$

Here we have defined $\psi_j = a_j/\sqrt{N_0}$ and fixed $g = UN_0$ as $N_0 \to \infty$. The initial conditions $\psi_j(0)$ are the parameters ψ_j appearing in the pure BEC state (5.33). We note that the nonlinear complex Schrödinger equation (5.35) could also be implemented in classical optics using an array of waveguides with absorption and Kerr nonlinearity.

5.2.1 Nonlinear Bloch bands

For a single particle we found that a knowledge of the band structure was crucial for understanding the number density Bloch oscillations. In the mean-field limit it is possible to define nonlinear Bloch states and their corresponding nonlinear generalised eigenvalues. In closed systems it has been shown that the presence of particle interactions can lead to novel features in the nonlinear Bloch bands. For instance, the formation of loops at the band edges [154] for a Bose-Einstein condensate in a bichromatic lattice [155]. Here we shall examine the nonlinear band structure when the odd lattice sites are dissipative.

The nonlinear Bloch states are defined as the stationary states ϕ_j of the field-free version of equation (5.35)

$$\mu\phi_j = -\left(\phi_{j+1} + \phi_{j-1}\right) + g|\phi_j|^2\phi_j + i\gamma\left((-1)^j - 1\right)\phi_j, \tag{5.36}$$

where μ is a generalised nonlinear complex eigenvalue. Just as in the single-particle system, the translational symmetry motivates the ansatz

$$\phi_j = \begin{cases} A\mathrm{e}^{ikj}, & j \text{ even}, \\ B\mathrm{e}^{ikj}, & j \text{ odd}, \end{cases} \tag{5.37}$$

for the stationary states, with the quasimomentum $-\pi \leq k \leq \pi$ and the normalisation convention $|A|^2 + |B|^2 = 1$. The coefficients A and B are then determined by the nonlinear two-level system

$$\begin{pmatrix} g|A|^2 & -2\cos k \\ -2\cos k & g|B|^2 - 2i\gamma \end{pmatrix} \begin{pmatrix} A \\ B \end{pmatrix} = \mu \begin{pmatrix} A \\ B \end{pmatrix}. \tag{5.38}$$

This reduces to the single-particle case (5.30) for non-interacting particles $g = 0$. To simplify the calculations an overall complex energy $\frac{g}{2} - i\gamma$ is subtracted from the diagonal, leading to the PT-symmetric system

$$\begin{pmatrix} cz + i\gamma & -2\cos k \\ -2\cos k & -cz - i\gamma \end{pmatrix} \begin{pmatrix} A \\ B \end{pmatrix} = \tilde{\mu} \begin{pmatrix} A \\ B \end{pmatrix}, \tag{5.39}$$

with

$$z = |A|^2 - |B|^2, \quad c = \frac{g}{2}. \tag{5.40}$$

In [147] Graefe has shown that the eigenvalues of a nonlinear complex two-level system (5.39) can be obtained analytically. Here we closely follow the procedure in [147] to obtain the nonlinear Bloch bands. Multiplying the first equation by $\bar{A}$, the second by $\bar{B}$, and making use of the normalisation condition $|A|^2 + |B|^2 = 1$, yields the generalised eigenvalues

$$\tilde{\mu} = cz^2 + i\gamma z - 2\cos k \left(\bar{A}B + \bar{B}A\right). \tag{5.41}$$

For $k = \pm\frac{\pi}{2}$ equation (5.41) reduces to

$$\tilde{\mu} = cz^2 + i\gamma z \tag{5.42}$$

and (5.39) provides the two conditions

$$(cz + i\gamma)\, A = \tilde{\mu}A, \quad -(cz + i\gamma)\, B = \tilde{\mu}B. \tag{5.43}$$

In this case the only solutions are $z = \pm 1$, corresponding to $(A = 1, B = 0)$ and $(A = 0, B = 1)$ with generalised eigenvalues $\mu = g$ and $\mu = g - 2i\gamma$ respectively.

When $k \neq \pm\frac{\pi}{2}$ it can be shown that the possible values of the population imbalance z are given by the real roots of the polynomial

$$\left(c^2 + \gamma^2\right) z^4 + \left(4\cos^2 k - c^2 - \gamma^2\right) z^2 = 0, \tag{5.44}$$

which has the four solutions

$$z = 0, 0, \pm\sqrt{1 - \frac{4\cos^2 k}{c^2 + \gamma^2}}. \tag{5.45}$$

Let us now parameterise the nonlinear Bloch states as

$$A = \sqrt{\frac{1+z}{2}}\mathrm{e}^{-iv}, \quad B = \sqrt{\frac{1-z}{2}}\mathrm{e}^{iv}. \tag{5.46}$$

Following the analysis in [147] it can be shown that when $k \neq \pm\frac{\pi}{2}$ there are up to four possible solutions with

$$(z, v) = \begin{cases} \left(0, \frac{1}{2}\arcsin\left(\frac{\gamma}{2\cos k}\right)\right), & (5.47) \\ \left(\pm\sqrt{1 - \frac{4\cos^2 k}{c^2+\gamma^2}}, -\frac{1}{2}\arctan\left(\frac{\gamma}{c}\right)\right), & (5.48) \end{cases}$$

where the phase coordinate for the second solution in (5.47) is given by $\pi/2 - v$. The nonlinear eigenvalues corresponding to the two solutions in (5.47) are given by

$$\mu = \mp \mathrm{sgn}(\cos k)\sqrt{4\cos^2 k - \gamma^2} + c - i\gamma \tag{5.49}$$

respectively. Those corresponding to the two solutions (5.48) may be written in the form

$$\mu = 2c\left[1 - \frac{2\cos^2 k}{c^2+\gamma^2}\left(1 + \mathrm{sgn}(\cos k)\right)\right] + i\gamma(z-1). \tag{5.50}$$

In the latter expression the real part of μ is constant when $\cos k$ is negative, resulting in nonlinear Bloch bands that are 2π-periodic. This should be contrasted with the non-interacting Bloch bands ($g = 0$), which were found to be π-periodic.

Only pairs (z, v) that are real valued correspond to solutions. Thus, there are only two solutions for $|2\cos k| < \gamma$ and two for $4\cos^2 k > c^2 + \gamma^2$. There are three solutions at the exceptional points $2|\cos k| = \gamma$, where the two solutions (5.47) coalesce in an exceptional point (EP2). The nonlinearity introduces additional exceptional points at the quasimomentum values $2|\cos k| = \sqrt{c^2+\gamma^2}$. At these points there can be three or two solutions. There are three solutions for $\mathrm{sgn}(\cos k) > 0$, as the two solutions in (5.48) coalesce (EP2). Surprisingly, there are only two solutions for $\mathrm{sgn}(\cos k) < 0$, as both the solutions in (5.48) coalesce with one solution in (5.47) (EP3). Otherwise there are four solutions. The existence of an EP2, EP3 and even an EP4 has previously been demonstrated for a BEC in a PT-symmetric double well potential [148, 149, 156].

The real and imaginary parts of μ are plotted in Figure 5.6 for weak ($g = 2$) and strong ($g = 7$) interaction strengths, when the decay rate is $\gamma = 0.1$. The Bloch bands for the non-interacting ($g = 0$) case are also shown in the top row for comparison.

The combination of interaction and dissipation leads to significant changes in the band structure compared to the single particle (non-interacting) case. When g is switched on a pair of solutions vanish just after the exceptional points at $2|\cos k| = \gamma$, visible around $k = \pm\pi/2$, and a new band emerges (coloured blue). The interaction introduces additional exceptional points at $2|\cos k| = \sqrt{c^2+\gamma^2}$ that vanish when $\sqrt{c^2+\gamma^2} > 2$. Away from exceptional points the solutions in the blue band have the same real part but different imaginary parts. The solutions in the black band have different real parts but degenerate imaginary parts.

5.2.2 Stability analysis

In contrast to the Bloch states of the single-particle system, the nonlinear Bloch states can become dynamically unstable due to particle interactions. The stability of the stationary states can be determined by examining the effect of a small time-dependent perturbation of the stationary solution of the form [155]

$$\psi_j(t) = \mathrm{e}^{-i\mu t}\phi_j + \begin{cases} \mathrm{e}^{ikj-i\mu t}\left(\mathrm{e}^{-i\omega t}\delta\chi_-^A + \mathrm{e}^{i\bar{\omega}t}\overline{\delta\chi}_+^A\right), & j \text{ even}, \\ \mathrm{e}^{ikj-i\mu t}\left(\mathrm{e}^{-i\omega t}\delta\chi_-^B + \mathrm{e}^{i\bar{\omega}t}\overline{\delta\chi}_+^B\right), & j \text{ odd}. \end{cases} \tag{5.51}$$

By inserting the ansatz (5.51) into the field-free version of (5.35) the problem reduces to the two-mode system analysed in [147], and the stability analysis obtained therein can immediately be applied.

In particular, it is sufficient to consider the nonlinear Schrödinger equation

$$i\frac{d}{dt}\begin{pmatrix}\Psi_1\\ \Psi_2\end{pmatrix} = H_{nl}(|\Psi_1|^2, |\Psi_2|^2)\begin{pmatrix}\Psi_1\\ \Psi_2\end{pmatrix}, \tag{5.52}$$

where $H_{nl}(|\Psi_1|^2, |\Psi_2|^2)$ is the two-level nonlinear Hamiltonian

$$H_{nl}(|\Psi_1|^2, |\Psi_2|^2) = \begin{pmatrix} g|\Psi_1|^2 & -2\cos k \\ -2\cos k & g|\Psi_2|^2 - 2i\gamma \end{pmatrix}. \tag{5.53}$$

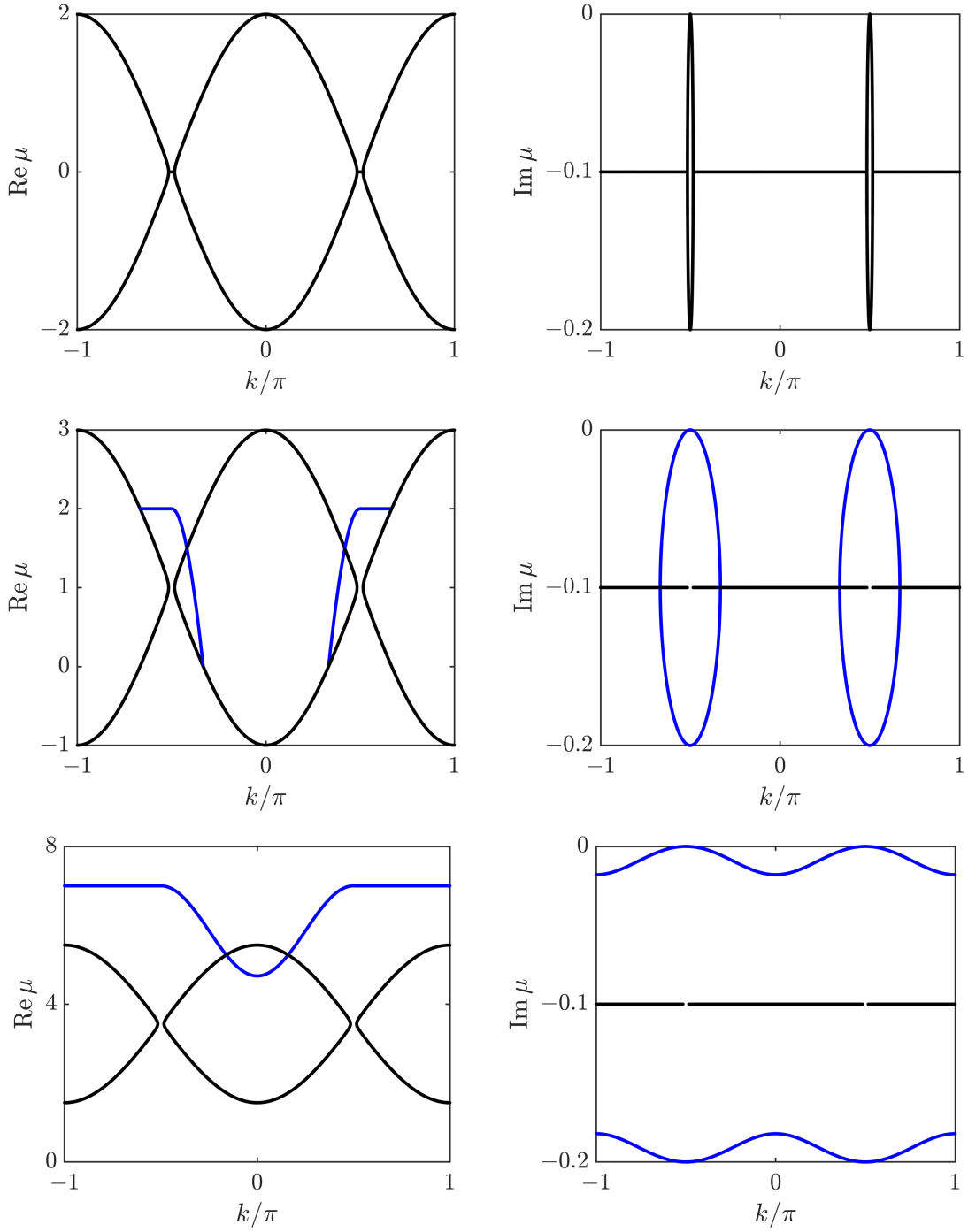


FIGURE 5.6: Real (left column) and imaginary (right column) parts of the nonlinear Bloch bands for $g = 0$ (top row), $g = 2$ (middle row) and $g = 7$ (bottom row) when $\gamma = 0.1$.

In the previous section we found that the stationary states of this system are given by $\chi = (A, B)$, with corresponding nonlinear eigenvalues μ. Therefore, the stability analysis (5.51) reduces to analysing the linearised effect of a small time-dependent perturbation to the stationary solution χ of the form

$$\Psi(t) = \mathrm{e}^{-i\mu t}\left(\chi + \delta\chi_- \mathrm{e}^{-i\omega t} + \overline{\delta\chi}_+ \mathrm{e}^{i\bar{\omega} t}\right), \tag{5.54}$$

where the components of $\delta\chi_\pm = (\delta\chi_\pm^A, \delta\chi_\pm^B)$ are defined in (5.51). In this case it can be shown [147] that the Bogoliubov-de Gennes equations yield the eigenvalue equation

$$M \begin{pmatrix} \delta\chi_- \\ \delta\chi_+ \end{pmatrix} = \omega \begin{pmatrix} \delta\chi_- \\ \delta\chi_+ \end{pmatrix}, \tag{5.55}$$

where M is the 4×4 matrix

$$M = \begin{pmatrix} H^0_{nl} - \mu + cP \begin{pmatrix} |A|^2 & -A\bar{B} \\ -\bar{A}B & |B|^2 \end{pmatrix} P & cP \begin{pmatrix} A^2 & -AB \\ -AB & B^2 \end{pmatrix} \bar{P} \\ -c\bar{P} \begin{pmatrix} \bar{A}^2 & -\bar{A}\bar{B} \\ -\bar{A}\bar{B} & \bar{B}^2 \end{pmatrix} P & -\bar{H}^0_{nl} + \bar{\mu} - c\bar{P} \begin{pmatrix} |A|^2 & -\bar{A}B \\ -A\bar{B} & |B|^2 \end{pmatrix} \bar{P} \end{pmatrix}. \tag{5.56}$$

Here H^0_{nl} is the nonlinear Hamiltonian (5.53) evaluated at the stationary solution $\chi = (A, B)$ and P is the projection matrix orthogonal to χ,

$$P = \begin{pmatrix} 1 - |A|^2 & -A\bar{B} \\ -\bar{A}B & 1 - |B|^2 \end{pmatrix}. \tag{5.57}$$

The imaginary parts of the eigenvalues ω determine the stability of the stationary solution χ. When $\mathrm{Im}\,\omega \leq 0$ the perturbations are decaying or oscillating, and the solution is stable. On the other hand, if $\mathrm{Im}\,\omega > 0$ the perturbations grow exponentially and the solution is unstable. A short calculation reveals that at $k = \pm\pi/2$ the solution $\chi = (1, 0)$ with $\mu = g$ is stable, while the second solution $\chi = (0, 1)$ with $\mu = g - 2i\gamma$ is unstable. In general the stability of the stationary solutions changes as the system parameters are varied. This is illustrated in Figure 5.7 for two different values of g and varying

quasimomentum values, with $\gamma = 0.1$.

For the states (5.47), with corresponding nonlinear eigenvalues (5.49), the eigenvalue equation (5.55) yields the characteristic polynomial

$$\omega^4 + 4\left(\gamma^2 - 4\cos^2 k \mp \operatorname{sgn}(\cos k) c\sqrt{4\cos^2 k - \gamma^2}\right)\omega^2 = 0. \tag{5.58}$$

It follows that for $\operatorname{sgn}(\cos k) > 0$ the solution corresponding to μ_+ becomes unstable for quasimomentum values satisfying $4\cos^2 k < c^2 + \gamma^2$, while the other state corresponding to μ_- remains stable. The behaviour of these solutions is reversed when the cosine changes sign, i.e., when $\operatorname{sgn}(\cos k) < 0$.

It is important to note that the stability obtained from the Bogoliubov-de Gennes equations can differ during the time evolution of the system. Due to particle losses the norm $(|A|^2+|B|^2)$ is no longer conserved. This effectively leads to a time-dependent interaction strength and, therefore, different stability behaviour during the time evolution. We shall now show that the stability of the nonlinear Bloch bands can have a strong influence on the mean-field dynamics.

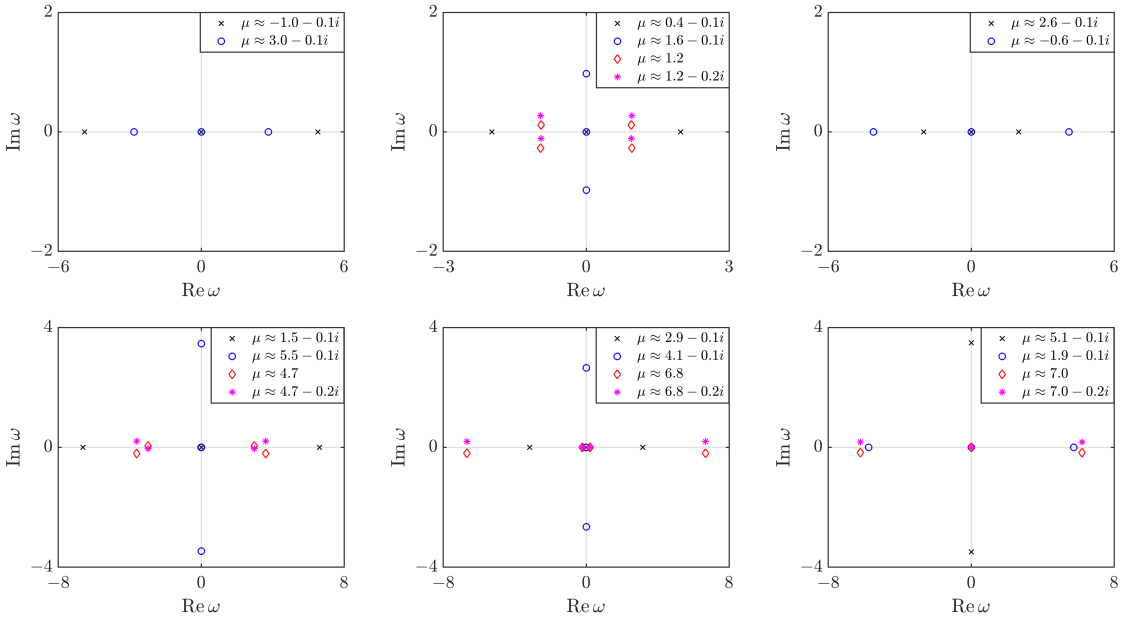


FIGURE 5.7: Eigenvalues ω of the stability matrix M corresponding to different stationary states for $\gamma = 0.1$, $g = 2$ (top row) and $g = 7$ (bottom row). The columns show results for different values of the quasimomentum, with $k = 0$ (left), $k = -0.4\pi$ (middle) and $k = -0.8\pi$ (right).

5.2.3 Mean-field and two-particle dynamics

We now examine the dynamics of an initial pure BEC state (5.33). The parameters ψ_j of the BEC state are taken to be the components of a nonlinear stationary state ϕ_j (5.37), weighted by a Gaussian envelope $\psi_j \propto \phi_j e^{-(j-q_0)^2/2\sigma^2}$. In particular, we assume that $k = 0$ and consider the two stationary states in (5.47), which correspond to a pure BEC in the lower or upper black bands at $k = 0$ in Figure 5.6.

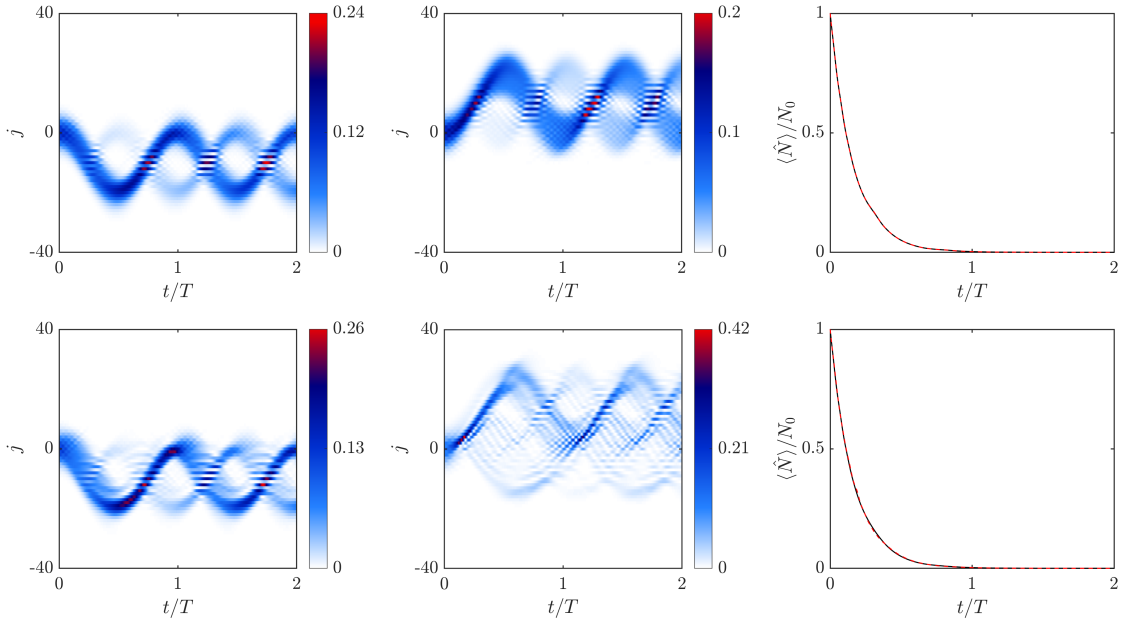


FIGURE 5.8: (Top row) The renormalised number density is plotted as a function of time for an initial pure BEC in the lower band (left) and the upper band (middle), with $k = 0$, $x_0 = 0$ and $\sigma = \sqrt{20}$. The right frame shows the total particle number expectation value dynamics for both the initial states (lower band - black; upper band - red dashed). The system parameters are $g = 2$, $\gamma = 0.1$ and $F = 0.2$. (Bottom row) As in the top row, with $g = 7$.

The renormalised density dynamics are shown in Figure 5.8 for both initial states, with $\gamma = 0.1$ and $F = 0.2$. For a weak interaction strength ($g = 2$) and a state initialised in the lower band, the particles perform Bloch oscillations accompanied by a splitting of the beam in position space. As expected, the dynamics are similar to the single-particle system. However, if the state is initialised in the upper band then the dynamics deviate from the single-particle case. This can be attributed to the change in the stability of the upper band, which is depicted in the top row of Figure 5.7. For a strong interaction strength ($g = 7$) the lower band is initially stable, while the upper band is initially

unstable (Figure 5.7). This has a dramatic effect on the mean-field dynamics, as can clearly be seen in Figure 5.8. In particular, the strong instability of the upper band results in a focussing of the density towards a single lattice site. The subsequent dynamics are not dissimilar to the frequency doubled single-particle Bloch oscillations depicted in Figure 5.2.

Surprisingly, even far from the mean-field limit, the stability of the density dynamics has a dependence on the initial state. This is illustrated in Figure 5.9 for a two-particle system with $\gamma = 0.1$ and $F = 0.2$. For a weak interaction strength ($U = 1$) and a state initialised in the lower band, the density behaves like a single particle. However, if the state is initialised in the upper band, then a squeezing and broadening of the density beam is observed, as well as additional structure from $t \approx 0.5T$ onwards. Increasing the interaction strength ($U = 7$) leads to additional many-body features, yet there is still a clear difference between the density dynamics for different initial states. A thorough investigation of the two-particle quantum dynamics is left for future work.

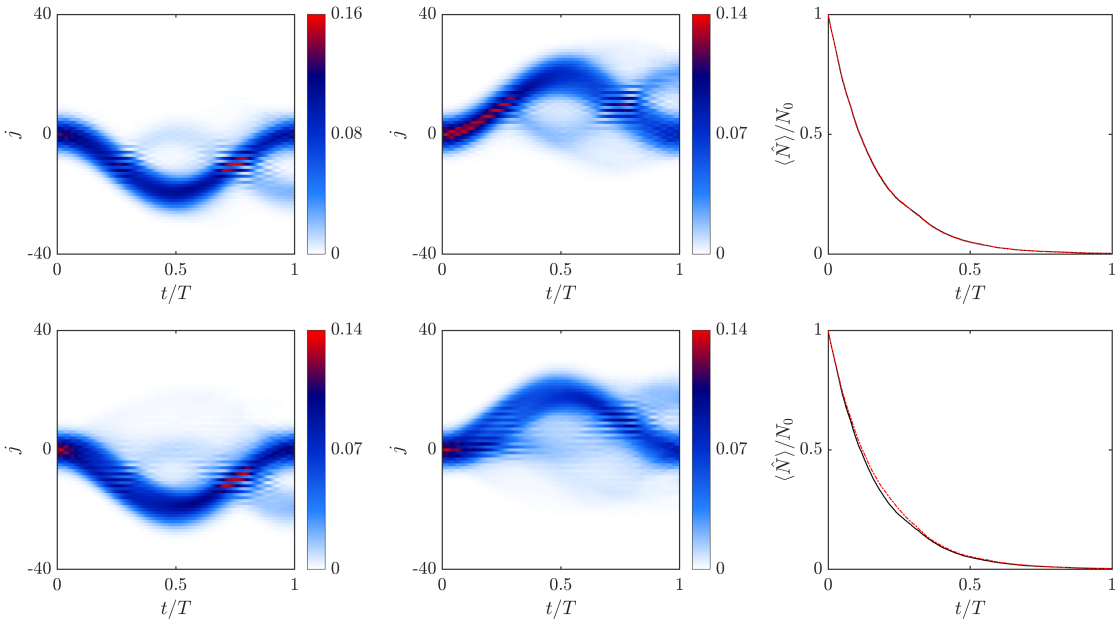


FIGURE 5.9: As in Figure 5.8 but for $N = 2$ particles, with $U = 1$ (top row) and $U = 7$ (bottom row).

5.3 Summary

We have investigated Bloch oscillations in a Bose-Hubbard chain with single-particle losses from the odd lattice sites. We demonstrated that the single-particle system may be viewed as a quantum implementation of the PT-symmetric Hamiltonian discussed in Chapter 4. The spectrum of the single-particle effective Hamiltonian was analysed and found to consist of two ladders of eigenvalues, which we linked to dynamical effects. In the mean-field limit of a many-particle system we derived analytic expressions for the generalised nonlinear stationary states and the nonlinear Bloch bands. The combination of nonlinearity and particle losses led to unusual features in the nonlinear Bloch bands, such as the vanishing of solutions and the formation of additional exceptional points. The stability of the stationary states was determined via the Bogoliubov-de Gennes equation, and was shown to strongly influence the mean-field dynamics. Finally, for a two-particle system far from the mean-field limit, the stability of the density dynamics was shown to have a dependence on the initial state.

Appendix A

The quantum jump method

In this appendix we provide details of the quantum jump method, which is used at several points throughout the thesis to numerically solve the Lindblad equation. Let us first assume that the initial state is a pure state $\hat{\rho}(0) = |\phi(0)\rangle\langle\phi(0)|$. The quantum jump method evolves the initial state $|\phi(0)\rangle$ using a stochastic procedure to obtain $|\phi(t)\rangle$, referred to as an individual quantum trajectory. By averaging over many trajectories, the time evolution of the quantum state $\hat{\rho}(t)$, and thereby the expectation values of operators, can be obtained. In each time step the original formulation of the quantum jump method [18, 19] proceeds as follows:

1. Suppose that the state at the beginning of the time step is $|\phi(t)\rangle$. This is also referred to as the Monte-Carlo wavefunction (MCWF). This state is evolved under the effective Hamiltonian (1.6) so that at time $t + \delta t$

$$|\tilde{\phi}(t+\delta t)\rangle = \left(\hat{I} - i\hat{H}_{\text{eff}}\delta t\right)|\phi(t)\rangle, \tag{A.1}$$

   provided that δt is sufficiently small. As $\hat{H}_{\text{eff}}$ is non-Hermitian the norm of this state will be less than one. In particular,

$$\langle\tilde{\phi}(t+\delta t)|\tilde{\phi}(t+\delta t)\rangle = 1 - \delta t \sum_j \langle\phi(t)|\hat{L}_j^\dagger \hat{L}_j|\phi(t)\rangle = 1 - \delta p, \tag{A.2}$$

where $\delta p = \sum_j \delta p_j$ with $\delta p_j = \delta t \langle\phi(t)|\hat{L}_j^\dagger \hat{L}_j|\phi(t)\rangle \geq 0$. Each δp_j can be interpreted as the probability that the process described by the Lindblad operator $\hat{L}_j$ occurs during this time step. Furthermore, for this calculation to be valid δt must be chosen so that $\delta p \ll 1$.

2. In order to determine the time evolution during this time step, a uniform random number r is drawn between 0 and 1. If $r > \delta p$ then no jump occurs and the normalised state at time $t + \delta t$ is given by

$$|\phi(t+\delta t)\rangle = \frac{|\tilde{\phi}(t+\delta t)\rangle}{\sqrt{1-\delta p}}. \tag{A.3}$$

As δp is very small this is the typical evolution. On the other hand, if $r \leq \delta p$ a jump occurs and we must choose a particular $\hat{L}_j$ to apply to the state. The jump associated with the Lindblad operator $\hat{L}_j$ occurs with probability $P_j = \delta p_j/\delta p$ and the state after the jump is

$$|\phi(t+\delta t)\rangle = \frac{\hat{L}_j|\phi(t)\rangle}{\sqrt{\delta p_j/\delta t}}. \tag{A.4}$$

To show that this stochastic procedure is equivalent to the Lindblad equation, we consider the average of the operator $\hat{\sigma}(t) = |\phi(t)\rangle\langle\phi(t)|$ over many trajectories, denoted by $\overline{\hat{\sigma}(t)}$. Suppose that at time t the MCWF is given by $|\phi(t)\rangle$. Due to the different possible outcomes of no jump or jump, the average value of $\hat{\sigma}(t+\delta t)$ is given by

$$\overline{\hat{\sigma}(t+\delta t)} = (1-\delta p)\frac{|\tilde{\phi}(t+\delta t)\rangle}{\sqrt{1-\delta p}}\frac{\langle\tilde{\phi}(t+\delta t)|}{\sqrt{1-\delta p}} + \delta p \sum_j P_j \frac{\hat{L}_j|\phi(t)\rangle}{\sqrt{\delta p_j/\delta t}}\frac{\langle\phi(t)|\hat{L}_j^\dagger}{\sqrt{\delta p_j/\delta t}}. \tag{A.5}$$

After inserting the various definitions introduced in the discussion above this simplifies to

$$\overline{\hat{\sigma}(t+\delta t)} = \hat{\sigma}(t) - i\delta t\left(\hat{H}_{\text{eff}}\hat{\sigma}(t) - \hat{\sigma}(t)\hat{H}_{\text{eff}}^\dagger\right) + \delta t \sum_j \hat{L}_j\hat{\sigma}(t)\hat{L}_j^\dagger. \tag{A.6}$$

Averaging over all trajectories, and taking the limit $\delta t \to 0$, indeed yields the Lindblad equation

$$\frac{d}{dt}\overline{\hat{\sigma}(t)} = -i\left(\hat{H}_{\text{eff}}\overline{\hat{\sigma}(t)} - \overline{\hat{\sigma}(t)}\hat{H}_{\text{eff}}^\dagger\right) + \sum_j \hat{L}_j\overline{\hat{\sigma}(t)}\hat{L}_j^\dagger. \tag{A.7}$$

Thus, if $\hat{\rho}(0) = |\phi(0)\rangle\langle\phi(0)|$ then $\overline{\hat{\sigma}(t)}$ and $\hat{\rho}(t)$ coincide for all time. The expectation value of an arbitrary operator $\hat{A}$ can then be calculated from $\langle\hat{A}\rangle_t = \mathrm{Tr}\left(\overline{\hat{\sigma}(t)}\hat{A}\right)$. Furthermore, this procedure can be generalised to mixed initial states by decomposing the initial state into a statistical mixture of pure states $\hat{\rho}(0) = \sum_k p_k|\lambda_k\rangle\langle\lambda_k|$ and then randomly choosing the initial MCWF from the set $\{|\lambda_k\rangle\}$ with the probabilities $\{p_k\}$.

The original formulation of the quantum jump method outlined above has two main deficiencies. The first, it is only of first order in the time step δt. The second, a jump takes an entire time step, so that the method underestimates the time between jumps. In this thesis the method presented in [20] is implemented, which improves upon the previous algorithm by allowing the effective Hamiltonian evolution to be numerically calculated to arbitrary precision. Moreover, jumps occur at specific instants of time, which can also be calculated to any accuracy desired. The algorithm goes as follows:

1. Sample the initial state $\hat{\rho}(t_0)$ to obtain the initial MCWF $|\phi(t_0)\rangle$.

2. Draw a random number η uniformly distributed in the interval $[0, 1]$. The time at which the next jump occurs t' is obtained by numerically solving

$$\|\mathrm{e}^{-i\hat{H}_{\mathrm{eff}}t'}|\phi(t_0)\rangle\|^2 = \eta \tag{A.8}$$

   to find the time t'. Here t_0 is the time that the previous jump occurred or the time at the start of the calculation.

3. Within the interval $t \in [t_0, t']$ the MCWF follows the deterministic evolution generated by the effective Hamiltonian

$$|\phi(t)\rangle = \frac{\mathrm{e}^{-i\hat{H}_{\mathrm{eff}}(t'-t_0)}|\phi(t_0)\rangle}{\|\mathrm{e}^{-i\hat{H}_{\mathrm{eff}}(t'-t_0)}|\phi(t_0)\rangle\|}. \tag{A.9}$$

4. At time t' a jump occurs, which is realised by the Lindblad operator $\hat{L}_j$ with probability

$$P_j = \frac{\langle\phi(t'_-)|\hat{L}_j^\dagger\hat{L}_j|\phi(t'_-)\rangle}{\sum_j\langle\phi(t'_-)|\hat{L}_j^\dagger\hat{L}_j|\phi(t'_-)\rangle}, \tag{A.10}$$

where $|\phi(t'_-)\rangle$ is the state at time t' obtained from the effective Hamiltonian evolution. If the process associated with $\hat{L}_j$ occurs, then the state after the jump is given by

$$|\phi(t'_+)\rangle = \frac{\hat{L}_j|\phi(t'_-)\rangle}{\|\hat{L}_j|\phi(t'_-)\rangle\|}. \tag{A.11}$$

5. Repeat the procedure from step 2 using $|\phi(t'_+)\rangle$ as the initial MCWF.

Appendix B

Asymptotic expressions for the Weber function

In this appendix we provide useful asymptotic expansions for the Weber function from [157]. If $|z| \gg 1$ and $|z| \gg |\nu|$, then depending on $\arg z$ we have

$$D_\nu(z) \sim \mathrm{e}^{-z^2/4} z^\nu \left(1 - \frac{\nu(\nu-1)}{2z^2} + \dots\right), \quad |\arg z| < \frac{3\pi}{4}, \tag{B.1}$$

$$\begin{aligned} D_\nu(z) \sim{}& \mathrm{e}^{-z^2/4} z^\nu \left(1 - \frac{\nu(\nu-1)}{2z^2} + \dots\right) \\ &- \frac{\sqrt{2\pi}}{\Gamma(-\nu)} \mathrm{e}^{i\nu\pi} \mathrm{e}^{z^2/4} z^{-\nu-1} \left(1 + \frac{(\nu+1)(\nu+2)}{2z^2} + \dots\right), \quad \frac{\pi}{4} < \arg z < \frac{5\pi}{4}, \end{aligned} \tag{B.2}$$

$$\begin{aligned} D_\nu(z) \sim{}& \mathrm{e}^{-z^2/4} z^\nu \left(1 - \frac{\nu(\nu-1)}{2z^2} + \dots\right) \\ &- \frac{\sqrt{2\pi}}{\Gamma(-\nu)} \mathrm{e}^{-i\nu\pi} \mathrm{e}^{z^2/4} z^{-\nu-1} \left(1 + \frac{(\nu+1)(\nu+2)}{2z^2} + \dots\right), \quad -\frac{5\pi}{4} < \arg z < -\frac{\pi}{4}. \end{aligned} \tag{B.3}$$

Appendix C

The single-band tight-binding Hamiltonian

Here we briefly discuss the dynamics of a single particle in a periodic potential under the influence of a static force. The presentation closely follows [140], which explores this topic in depth.

In the single-band tight-binding approximation the Hamiltonian of interest is

$$\hat{H} = \sum_{j=-\infty}^{+\infty} -J\left(|j+1\rangle\langle j| + |j\rangle\langle j+1|\right) + Fj|j\rangle\langle j|, \tag{C.1}$$

where $\{|j\rangle\}$ is an orthonormal basis (for example, $|j\rangle$ could be a Wannier state localised on lattice site j); $J \in \mathbb{R}$ is the hopping parameter between neighbouring sites; and $F \in \mathbb{R}$ is a static force.

It is convenient to study the system in the quasimomentum representation, i.e., in the basis of Bloch waves

$$|k\rangle = \frac{1}{\sqrt{2\pi}} \sum_{j=-\infty}^{+\infty} \mathrm{e}^{ikj}|j\rangle, \tag{C.2}$$

with the quasimomentum k is confined to the region $-\pi \leq k \leq \pi$. The Bloch waves are orthogonal and normalised to the 2π-periodic delta comb $\langle k|k'\rangle = \delta_{2\pi}(k-k')$, and satisfy the Bloch condition $\langle j+1|k\rangle = \mathrm{e}^{ikj}\langle j|k\rangle$. The tight-binding Hamiltonian (C.1) is

diagonal in the quasimomentum representation $\langle k|\hat{H}|k'\rangle = \delta_{2\pi}(k-k')H(k)$, with

$$H(k) = E(k) + iF\frac{d}{dk}, \tag{C.3}$$

and the first term

$$E(k) = -2J\cos k \tag{C.4}$$

is the dispersion relation for the field-free ($F = 0$) case.

The eigenstates of the Hamiltonian (C.3), referred to as Wannier-Stark states, are obtained from the eigenvalue equation $H(k)\Psi(k) = E\Psi(k)$ with the periodic boundary condition $\Psi(0) = \Psi(2\pi)$. Solving the eigenvalue equation yields the eigenstates

$$\Psi_m(k) = \langle k|\Psi_m\rangle = \frac{1}{\sqrt{2\pi}}\mathrm{e}^{-i\left(mk+\frac{2J}{F}\sin k\right)}, \tag{C.5}$$

corresponding to the eigenvalues $E_m = mF$, where $m = 0, \pm1, \pm2, \ldots$. The eigenvalues are equidistant and independent of the coupling parameter J, and form the so-called Wannier-Stark ladder.

As a consequence of the equidistance of the eigenvalues the dynamics are periodic with period $T = 2\pi/F$, referred to as the Bloch period. For example, Figure C.1 demonstrates

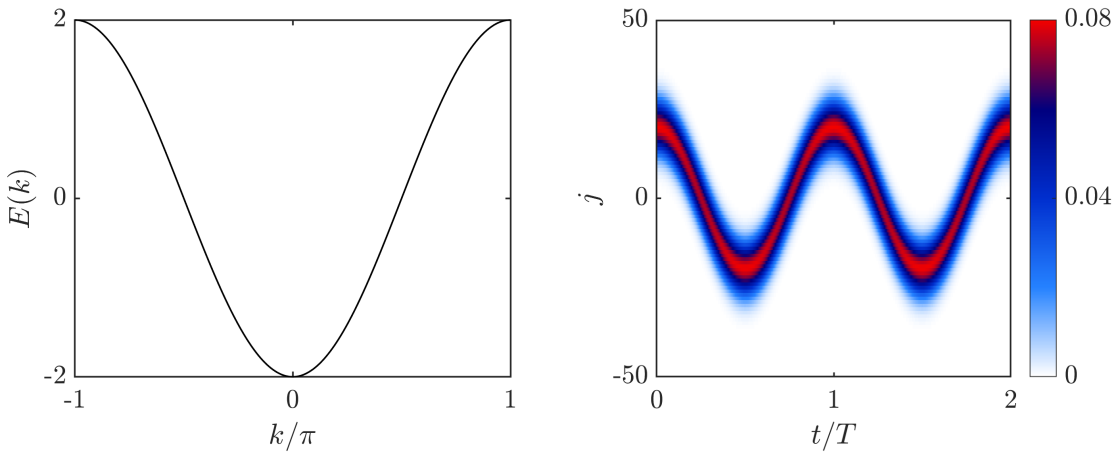


FIGURE C.1: (Left) The dispersion relation (C.4) with $J = 1$. (Right) Time evolution of the density for an initial broad Gaussian wave packet in position space with $x_0 = 20$, $k_0 = 0$ and $\sigma = \sqrt{50}$. The parameters $J = 1$, $F = 0.1$ and the Bloch period $T = 2\pi/F$.

that an initial broad Gaussian wave packet in position space performs Bloch oscillations with a period T, effectively mapping out the dispersion relation (C.4). Furthermore, by writing the time-evolution operator $\hat{U}(t) = \mathrm{e}^{-i\hat{H}t}$ in the Bloch wave basis,

$$\langle k'|\hat{U}(t)|k\rangle = \sum_m \langle k'|\Psi_m\rangle \mathrm{e}^{-iE_m t}\langle \Psi_m|k\rangle, \tag{C.6}$$

$$= \mathrm{e}^{-\frac{2iJ}{F}(\sin k' - \sin k)}\delta_{2\pi}(k' - k + Ft), \tag{C.7}$$

we see that the quasimomentum follows the acceleration theorem $k' = -Ft + k$.

Bibliography

[1] S. Diehl, A. Micheli, A. Kantian, B. Kraus, H. P. Büchler and P. Zoller, *Quantum states and phases in driven open quantum systems with cold atoms*, Nat. Phys. **4**, 878 (2008)

[2] P. Würtz, T. Langen, T. Gericke, A. Koglbauer and H. Ott, *Experimental Demonstration of Single-Site Addressability in a Two-Dimensional Optical Lattice*, Phys. Rev. Lett. **103**, 080404 (2009)

[3] V. V. Albert and L. Jiang, *Symmetries and conserved quantities in Lindblad master equations*, Phys. Rev. A **89**, 022118 (2014)

[4] H.-P. Breuer and F. Petruccione, *The theory of open quantum systems*, Oxford University Press, Oxford, (2002)

[5] A. J. Daley, *Quantum trajectories and open many-body quantum systems*, Advances in Physics **63**, 77 (2014)

[6] N. Moiseyev, *Non-Hermitian Quantum Mechanics*, Cambridge University Press, (2004)

[7] C. M. Bender, *PT symmetry: In quantum and classical physics*, World Scientific, (2018)

[8] D. Christodoulides and J. Yang, *Parity-Time symmetry and its applications*, Springer, (2018)

[9] H. M. Wiseman and G. J. Milburn, *Quantum Measurement and Control*, Cambridge University Press, Cambridge, (2014)

[10] K. Kraus, *States, effects, and operations: Fundamental notions of quantum theory*, Springer, Berlin, (1983)

[11] R. Alicki and K. Lendi, *Quantum dynamical semigroups and applications*, Springer, Berlin, (1987)

[12] G. Lindblad, *On the generators of quantum dynamical semigroups*, Commun. Math. Phys. **48**, 119 (1976)

[13] V. Gorini, A. Kossakowski and E. C. G. Sudarshan, *Completely positive dynamical semigroups of N-level systems*, J. Math. Phys. **17**, 821 (1976)

[14] B. Baumgartner, H. Narnhofer and W. Thirring, *Analysis of quantum semigroups with GKS-Lindblad generators: I. Simple generators*, J. Phys. A **41**, 065201 (2008)

[15] D. A. Lidar, I. L. Chuang and K. B. Whaley, *Decoherence-Free Subspaces for Quantum Computation*, Phys. Rev. Lett. **81**, 2594 (1998)

[16] C.-E. Bardyn, M. A. Baranov, C. V. Kraus, E. Rico, A. İmamoğlu, P. Zoller and S. Diehl, *Topology by dissipation*, New J. Phys. **15**, 085001 (2013)

[17] M. Am-Shallem, A. Levy, I. Schaefer and R. Kosloff, *Three approaches for representing Lindblad dynamics by a matrix-vector notation*, arXiv preprint arXiv:1510.08634 (2015)

[18] J. Dalibard, Y. Castin and K. Mølmer, *Wave-function approach to dissipative processes in quantum optics*, Phys. Rev. Lett. **68**, 580 (1992)

[19] R. Dum, P. Zoller and H. Ritsch, *Monte Carlo simulation of the atomic master equation for spontaneous emission*, Phys. Rev. A **45**, 4879 (1992)

[20] R. Dum, A. S. Parkins, P. Zoller and C. W. Gardiner, *Monte Carlo simulation of master equations in quantum optics for vacuum, thermal, and squeezed reservoirs*, Phys. Rev. A **46**, 4382 (1992)

[21] R. El-Ganainy, K. G. Makris, D. N. Christodoulides and Z. H. Musslimani, *Theory of coupled optical PT-symmetric structures*, Opt. Lett. **32**, 2632 (2007)

[22] Y. Ashida, S. Furukawa and M. Ueda, *Quantum critical behaviour influenced by measurement backaction in ultracold gases*, Phys. Rev. A **94**, 053615 (2016)

[23] C. M. Bender, S. Boettcher and P. N. Meisinger, *PT-symmetric quantum mechanics*, J. Math. Phys. **40**, 2201 (1999)

[24] C. M. Bender, D. C. Brody and H. F. Jones, *Complex Extension of Quantum Mechanics*, Phys. Rev. Lett. **89**, 270401 (2002)

[25] A. Guo, G. J. Salamo, D. Duchesne, R. Morandoti, M. Volatier-Ravat, V. Aimez, G. A. Siviloglou and D. N. Christodoulides, *Observation of PT-Symmetry Breaking in Complex Optical Potentials*, Phys. Rev. Lett. **103**, 093902 (2009)

[26] C. E. Rüter, K. G. Makris, R. El-Ganainy, D. N. Christodoulides, M. Segev and D. Kip, *Observation of parity-time symmetry in optics*, Nature Physics **6**, 192 (2010)

[27] D. C. Brody, *Biorthogonal quantum mechanics*, J. Phys. A: Math. Theor. **47**, 035305 (2014)

[28] G. Demange and E. M. Graefe, *Signatures of three coalescing eigenfunctions*, J. Phys. A: Math. Theor. **45**, 025303 (2012)

[29] W. D. Heiss, *The physics of exceptional points*, J. Phys. A: Math. Theor. **45**, 444016 (2012)

[30] H. Cartarius, J. Main and G. Wunner, *Exceptional Points in Atomic Spectra*, Phys. Rev. Lett. **99**, 173003 (2007)

[31] H. Cartarius and N. Moiseyev, *Fingerprints of exceptional points in the survival probability of resonances in atomic spectra*, Phys. Rev. A **84**, 013419 (2011)

[32] K. Jones-Smith and H. Mathur, *Non-Hermitian quantum Hamiltonians with $\mathcal{PT}$ symmetry*, Phys. Rev. A **82**, 042101 (2010)

[33] J. D. Jackson, *Classical Electrodynamics*, John Wiley & Sons, (1998)

[34] T. Prosen, *PT-Symmetric Quantum Liouvillean Dynamics*, Phys. Rev. Lett. **109**, 090404 (2012)

[35] D. Dast, D. Haag, H. Cartarius and G. Wunner, *Quantum master equation with balanced gain and loss*, Phys. Rev. A **90**, 052120 (2014)

[36] D. Dast, D. Haag, H. Cartarius, J. Main and G. Wunner, *Bose-Einstein condensates with balanced gain and loss beyond mean-field theory*, Phys. Rev. A **94**, 053601 (2016)

[37] T. Arimitsu and H. Umezawa, *A General Formulation of Nonequilibrium Thermo Field Dynamics*, Prog. Theo. Phys. **74**, 429 (1985)

[38] M. Ban, *Postselected quantum systems and their time evolution in non-equilibrium thermo-field dynamics*, Quantum Stud.: Math. Found. **3**, 203 (2016)

[39] L. Pitaevskii and S. Stringari, *Bose-Einstein Condensation and Superfluidity*, Oxford University Press, Oxford, (2018)

[40] C. Gross, *Spin squeezing, entanglement and quantum metrology with Bose-Einstein condensates*, J. Phys. B: At. Mol. Opt. Phys. **45**, 103001 (2012)

[41] T. Byrnes, K. Wen and Y. Yamamoto, *Macroscopic quantum computation using Bose-Einstein condensates*, Phys. Rev. A **85**, 040306(R) (2012)

[42] R. J. Lewis-Swan and K. V. Kheruntsyan, *Proposal for a motional-state Bell inequality test with ultracold atoms*, Phys. Rev. A **91**, 052114 (2015)

[43] O. Morsch and M. Oberthaler, *Dynamics of Bose-Einstein condensates in optical lattices*, Rev. Mod. Phys. **78**, 179 (2006)

[44] G. Kordas, D. Witthaut, P. Buonsante, A. Vezzani, R. Burioni, A. I. Karanikas and S. Wimberger, *The Dissipative Bose-Hubbard Model. Methods and Examples*, Eur. Phys. J. Special Topics **224**, 2127 (2015)

[45] T. J. Martinez, M. Ben-Nun and R. D. Levine, *Multi-Electronic-State Molecular Dynamics: A Wave Function Approach with Applications*, J. Phys. Chem. **100**, 7884 (1996)

[46] X. Kong, A. Markmann and V. S. Batista, *Time-sliced thawed Gaussian propagation method for simulations of quantum dynamics*, J. Phys. Chem. A **120**, 3260 (2016)

[47] D. V. Shalashilin and M. S. Child, *The phase-space CSS approach to quantum and semiclassical molecular dynamics for high-dimensional systems*, Chem. Phys. **304**, 103 (2004)

[48] D. V. Shalashilin, *Quantum mechanics with the basis set guided by Ehrenfest trajectories: Theory and application to spin-boson model*, J. Chem. Phys. **130**, 244101 (2009)

[49] M. F. Herman and E. Kluk, *A semiclassical justification for the use of non-spreading wavepackets in dynamics calculations*, Chem. Phys. **91**, 27 (1984)

[50] K. G. Kay, *Integral expressions for the semiclassical time-dependent propagator*, J. Chem. Phys. **100**, 4377 (1994)

[51] S. Tomsovic, *Complex saddle trajectories for multidimensional quantum wave packet and coherent state propagation: Application to a many-body system*, Phys. Rev. E **98**, 023301 (2018)

[52] S. Tomsovic, P. Schlagheck, D. Ullmo, J. D. Urbina and K. Richter, *Post-Ehrenfest many-body quantum interferences in ultracold atoms far out of equilibrium*, Phys. Rev. A **97**, 061606 (2018)

[53] L. Mandelstam and I. Tamm, *The uncertainty relation between energy and time in nonrelativistic quantum mechanics*, J. Phys. (USSR) **9**, 249 (1945)

[54] J. Uffink, *The rate of evolution of a quantum state*, Am. J. Phys. **61**, 935 (1993)

[55] D. C. Brody and L. P. Hughston, *Geometry of quantum statistical inference*, Phys. Rev. Lett. **77**, 2851 (1996)

[56] M. Paris and J. Rehacek, *Quantum State Estimation*, Springer, Berlin, (2004)

[57] V. Giovannetti, S. Lloyd and L. Maccone, *Advances in quantum metrology*, Nature Photonics **5**, 222 (2011)

[58] F. Campaioli, F. A. Pollock, F. C. Binder, L. Céleri, J. Goold, S. Vinjanampathy and K. Modi, *Enhancing the Charging Power of Quantum Batteries*, Phys. Rev. Lett. **118**, 150601 (2017)

[59] J. Anandan and Y. Aharonov, *Geometry of quantum evolution*, Phys. Rev. Lett. **65**, 1697 (1990)

[60] D. C. Brody, *Information geometry of density matrices and state estimation*, J. Phys. A **44**, 252002 (2011)

[61] S. Luo, *Wigner-Yanase skew information and uncertainty relations*, Phys. Rev. Lett. **91**, 180403 (2003)

[62] E. P. Wigner and M. M. Yanase, *Information contents of distributions*, Proc. Nat. Acad. Sci. **49**, 910 (1963)

[63] S. L. Braunstein and C. M. Caves, *Statistical distance and the geometry of quantum states*, Phys. Rev. Lett. **72**, 3439 (1994)

[64] D. Mondal and A. K. Pati, *Quantum speed limit for mixed states using an experimentally realizable metric*, Phys. Lett. A **380**, 1395 (2016)

[65] S. Deffner and S. Campbell, *Quantum speed limits: from Heisenberg's uncertainty principle to optimal quantum control*, J. Phys. A **50**, 453001 (2017)

[66] D. C. Brody, *Geometry of the complex extension of Wigner's theorem*, J. Phys. A **46**, 395301 (2013)

[67] S. Alipour, M. Mehboudi and A. T. Rezakhani, *Quantum metrology in open systems: Dissipative Cramér-Rao bound*, Phys. Rev. Lett. **112**, 120405 (2014)

[68] K. Funo, N. Shiraishi and K. Saito, *Speed limit for open quantum systems*, New J. Phys. **21**, 013006 (2019)

[69] R. Uzdin and R. Kosloff, *Speed limits in Liouville space for open quantum systems*, Europhys. Lett. **115**, 40003 (2016)

[70] S. Deffner and E. Lutz, *Quantum speed limit for non-Markovian dynamics*, Phys. Rev. Lett. **111**, 010402 (2013)

[71] A. Uhlmann, *The 'transition probability' in the state space of algebra*, Rep. on Math. Phys. **9**, 273 (1976)

[72] R. Jozsa, *Fidelity for mixed quantum states*, J. Mod. Opt. **41**, 2315 (1994)

[73] M. M. Taddei, B. M. Escher, L. Davidovich and R. L. de Matos Filho, *Quantum speed limit for physical processes*, Phys. Rev. Lett. **110**, 050402 (2013)

[74] A. del Campo, I. L. Egusquiza, M. B. Plenio and S. F. Huelga, *Quantum speed limit in open system dynamics*, Phys. Rev. Lett. **110**, 050403 (2013)

[75] D. C. Brody and E. M. Graefe, *Mixed-state evolution in the presence of gain and loss*, Phys. Rev. Lett. **109**, 230405 (2012)

[76] F. Campaioli, F. A. Pollock and K. Modi, *Tight, robust, and feasible quantum speed limits for open dynamics*, arXiv preprint arXiv:1806.08742v4 (2019)

[77] D. C. Brody, G. W. Gibbons and D. M. Meier, *Time-optimal navigation through quantum wind*, New J. Phys. **17**, 033048 (2015)

[78] V. Mukherjee, A. Carlini, A. Mari, T. Caneva, S. Montangero, T. Calarco, R. Fazio and V. Giovannetti, *Speeding up and slowing down the relaxation of a qubit by optimal control*, Phys. Rev. A **88**, 062326 (2013)

[79] D. C. Brody and B. Longstaff, *Evolution speed of open quantum dynamics*, Phys. Rev. Research **1**, 033127 (2019)

[80] R. A. Bertlmann and P. Krammer, *Bloch vectors for qudits*, J. Phys. A **41**, 235303 (2008)

[81] F. Campaioli, F. A. Pollock, F. C. Binder and K. Modi, *Tightening quantum speed limits for almost all states*, Phys. Rev. Lett. **120**, 060409 (2018)

[82] E. Schrödinger, *Der stetige Übergang von der Mikro- zur Makrophysik*, Naturwissenschaften **14**, 664 (1926)

[83] P. A. M. Dirac, *The Principles of Quantum Mechanics*, Oxford University Press, Oxford, (1958)

[84] E. J. Heller, *Time-dependent approach to semiclassical dynamics*, J. Chem. Phys. **62**, 1544 (1975)

[85] K. Hepp, *The classical limit for quantum mechanical correlation functions*, Commun. Math. Phys. **35**, 265 (1974)

[86] R. G. Littlejohn, *The semiclassical evolution of wave packets*, Phys. Rep. **138**, 193 (1986)

[87] E. J. Heller, *Frozen Gaussians: A very simple semiclassical approximation*, J. Chem. Phys. **75**, 2923 (1981)

[88] D. Huber and E. J. Heller, *Hybrid mechanics: A combination of classical and quantum mechanics*, J. Chem. Phys. **89**, 4752 (1988)

[89] D. Huber, S. Ling, D.G. Imre and E. J. Heller, *Hybrid mechanics. II*, J. Chem. Phys. **90**, 7317 (1989)

[90] W. H. Miller, *An alternative derivation of the Herman-Kluk (coherent state) semiclassical initial value representation of the time evolution operator*, Mol. Phys. **100**, 397 (2002)

[91] M. Baranger, M. A. M. de Aguiar, F. Keck, H. J. Korsch and B. Schellhaaß, *Semiclassical approximations in phase space with coherent states*, J. Phys. A **34**, 7227 (2001)

[92] W. T. Strunz, *Path integral, semiclassical and stochastic propagators for Markovian open quantum systems*, J. Phys. A **30**, 4053 (1997)

[93] A. M. Ozorio de Almeida, P. de M. Rios and O. Brodier, *Semiclassical evolution of dissipative Markovian systems*, J. Phys. A **42**, 065306 (2009)

[94] O. Brodier and A.M. Ozorio de Almeida, *Markovian evolution of Gaussian states in the semiclassical limit*, Phys. Lett. A **374**, 2315 (2010)

[95] E. M. Graefe and R. Schubert, *Wave packet evolution in non-Hermitian quantum systems*, Phys. Rev. A **83**, 060101(R) (2011)

[96] E. M. Graefe and R. Schubert, *Complexified coherent states and quantum evolution with non-Hermitian Hamiltonians*, J. Phys. A **45**, 244033 (2012)

[97] E. M. Graefe, B. Longstaff, T. Plastow and R. Schubert, *Lindblad dynamics of Gaussian states and their superpositions in the semiclassical limit*, J. Phys. A: Math. Theor. **51**, 365203 (2018)

[98] C. Zachos, D. Fairlie and T. Curtright, *Quantum Mechanics in Phase Space*, World Scientific Series, Singapore, (2005)

[99] G. Adesso, S. Ragy and A. R. Lee, *Continuous Variable Quantum Information: Gaussian States and Beyond*, Open Syst. Inf. Dyn. **21**, 1440001 (2014)

[100] I. C. Percival, *Quantum State Diffusion*, Cambridge University Press, Cambridge, (1998)

[101] M. Grmela and H. C. Öttinger, *Dynamics and thermodynamics of complex fluids. I. Development of a general formalism*, Phys. Rev. E **56**, 6620 (1997)

[102] H. C. Öttinger and M. Grmela, *Dynamics and thermodynamics of complex fluids. II. Illustrations of a general formalism*, Phys. Rev. E **56**, 6633 (1997)

[103] W. P. Bowen and G. J. Milburn, *Quantum Optomechanics*, CRC Press, Boca Raton, FL, (2016)

[104] R. Schubert and R. Vallejos and F. Toscano, *How do wave packets spread? Time evolution on Ehrenfest time scales*, J. Phys. A **45**, 215307 (2012)

[105] A. Polkovnikov, *Phase space representation of quantum dynamics*, Ann. Phys. **325**, 1790 (2010)

[106] C. W. Gardiner and P. Zoller, *Quantum Noise*, Springer-Verlag, Berlin Heidelberg, (2004)

[107] J. J. Włodarz, *On quantum mechanical phase-space wave functions*, J. Chem. Phys. **100**, 7476 (1994)

[108] G. Torres-Vega and J. H. Frederick, *A quantum mechanical representation in phase space*, J. Chem. Phys. **98**, 3103 (1993)

[109] S. Koda, *Initial-value semiclassical propagators for the Wigner phase-space representation: Formulation based on the interpretation of the Moyal equation as a Schrödinger equation*, J. Chem. Phys. **143**, 244110 (2015)

[110] M. Schlosshauer, *Decoherence and the quantum-to-classical transition*, Springer-Verlag, Berlin Heidelberg, (2010)

[111] D. C. Brody and E. M. Graefe, *Information Geometry of Complex Hamiltonians and Exceptional Points*, Entropy **15**, 3361 (2013)

[112] H. Menke, M. Klett, H. Cartarius, J. Main and G. Wunner, *State flip at exceptional points in atomic spectra*, Phys. Rev. A **93**, 013401 (2016)

[113] R. Thomas, H. Li, F. M. Ellis and T. Kottos, *Giant nonreciprocity near exceptional-point degeneracies*, Phys. Rev. A **94**, 043829 (2016)

[114] W. Chen, Ş. K. Özdemir, G. Zhao, J. Wiersig and L. Yang, *Exceptional points enhance sensing in an optical microcavity*, Nature **548**, 192 (2017)

[115] H. Hodaei, A. U. Hassan, S. Wittek, H. Garcia-Gracia, R. El-Ganainy, D. N. Christodoulides and M. Khajavikhan, *Enhanced sensitivity at higher-order exceptional points*, Nature **548**, 187 (2017)

[116] A. Lupu, V. V. Konotop and H. Benisty, *Optimal $\mathcal{PT}$-symmetric switch features exceptional point*, Scientific Reports **7**, 13299 (2017)

[117] V. Achilleos, G. Theocharis, O. Richoux and V. Pagneux, *Non-Hermitian acoustic metamaterials: Role of exceptional points in sound absorption*, Phys. Rev. B **95**, 144303 (2017)

[118] T. Goldzak, A. A. Mailybaev and N. Moiseyev, *Light Stops at Exceptional Points*, Phys. Rev. Lett. **120**, 013901 (2018)

[119] S. Longhi, *Loschmidt echo and fidelity decay near an exceptional point*, arXiv preprint arXiv:1905.03553 (2019)

[120] J. Doppler, A. A. Mailybaev, J. Böhm, U. Kuhl, A. Girschik, F. Libisch, T. J. Milburn, P. Rabl, N. Moiseyev and S. Rotter, *Dynamically encircling an exceptional point for asymmetric mode switching*, Nature **537**, 76 (2016)

[121] H. Xu, D. Mason, L. Jiang and J. G. E. Harris, *Topological energy transfer in an optomechanical system with exceptional points*, Nature **537**, 80 (2016)

[122] A. U. Hassan, B. Zhen, M. Soljačić, M. Khajavikhan and D. N. Christodoulides, *Dynamically Encircling Exceptional Points: Exact Evolution and Polarization State Conversion*, Phys. Rev. Lett. **118**, 093002 (2017)

[123] X.-L. Zhang, S. Wang, B. Hou and C. T. Chan, *Dynamically Encircling Exceptional Points: In situ Control of Encircling Loops and the Role of the Starting Point*, Phys. Rev. X **8**, 021066 (2018)

[124] M. V. Berry and R. Uzdin, *Slow non-Hermitian cycling: exact solutions and the Stokes phenomenon*, J. Phys. A **44**, 435303 (2011)

[125] R. Uzdin, A. Mailybaev and N. Moiseyev, *On the observability and asymmetry of adiabatic state flips generated by exceptional points*, J. Phys. A **44**, 435302 (2011)

[126] E. M. Graefe, A. A. Mailybaev and N. Moiseyev, *Breakdown of adiabatic transfer of light in waveguides in the presence of absorption*, Physical review A **88**, 033842 (2013)

[127] T. J. Milburn, J. Doppler, C. A. Holmes, S. Portolan, S. Rotter and P. Rabl, *General description of quasiadiabatic dynamical phenomena near exceptional points*, Phys. Rev. A **92**, 052124 (2015)

[128] N. Bender, H. Li, F. M. Ellis and T. Kottos, *Wave-packet self-imaging and giant recombinations via stable Bloch-Zener oscillations in photonic lattices with local $\mathcal{PT}$ symmetry*, Phys. Rev. A **92**, 041803 (2015)

[129] M. Wimmer, M.-A. Miri, D. Christodoulides and U. Peschel, *Observation of Bloch oscillations in complex PT-symmetric photonic lattices*, Sci. Rep. **5**, 17760 (2015)

[130] B. Longstaff and E. M. Graefe, *Non-adiabatic transitions through exceptional points in the band structure of a PT-symmetric lattice*, Phys. Rev. A **100**, 052119 (2019)

[131] S. Longhi, D. Gatti, and G. Della Valle *Robust light transport in non-Hermitian photonic lattices*, Sci. Rep. **5**, 13376 (2015)

[132] A. Peres, *Stability of quantum motion in chaotic and regular systems*, Phys. Rev. A **30**, 1610 (1984)

[133] A. Goussev, R. A. Jalabert, H. M. Pastawski and D. A. Wisniacki, *Loschmidt echo and time reversal in complex systems*, Phil. Trans. R. Soc. A **374**, 20150383 (2016)

[134] C. Zener, *Non-Adiabatic Crossing of Energy Levels*, Proc. Roy. Soc. Lond. A **137**, 696 (1932)

[135] M. Abramowitz and I. A. Stegun, *Handbook of Mathematical Functions*, Dover Publications, Inc., New York, (1972)

[136] S. Longhi, *Bloch Oscillations in Complex Crystals with PT Symmetry*, Phys. Rev. Letters **103**, 123601 (2009)

[137] Z. Turker and C. Yuce, *Super Bloch oscillation in a PT symmetric system*, Phys. Lett. A **360**, 2260 (2016)

[138] Y.-L Xu, W. S. Fegadolli, L. Gan, M.-H. Lu, X.-P Liu, Z.-Y Li, A. Scherer, and Y.-F Chen, *Experimental realization of Bloch oscillations in a parity-time synthetic silicon photonic lattice*, Nature Communications **7**, 11319 (2016)

[139] S. Longhi, *Spectral singularities and Bragg scattering in complex crystals*, Phys. Rev. A **81**, 022102 (2010)

[140] T. Hartmann, F. Keck, H. J. Korsch and S. Mossmann, *Dynamics of Bloch oscillations*, New J. Phys. **6**, 2 (2004)

[141] F. Casas, A. Murua and M. Nadinic, *Efficient computation of the Zassenhaus formula*, Comp. Phys. Comm. **183**, 2386 (2012)

[142] S. Wimberger, R. Mannella, O. Morsch, E. Arimondo, A. R. Kolovky and A. Buchleitner, *Nonlinearity-induced destruction of resonant tunneling in the Wannier-Stark problem*, Phys. Rev. A **72**, 063610 (2005)

[143] A. Zenesini, C. Sias, H. Lignier, Y. Singh, D. Ciampini, O. Morsch, R. Mannella, E. Arimondo, A. Tomadin and S. Wimberger, *Resonant tunneling of Bose-Einstein condensates in optical lattices*, New J. Phys. **10**, 053038 (2008)

[144] A. R. Kolovsky, H. J. Korsch and E. M. Graefe, *Bloch oscillations of Bose-Einstein condensates: Quantum counterpart of dynamical instability*, Phys. Rev. A **80**, 023617 (2009)

[145] P. M. Preiss, R. Ma, M. Eric Tai, A. Lukin, M. Rispoli, P. Zupancic, Y. Lahini, R. Islam and M. Greiner, *Strongly correlated quantum walks in optical lattices*, Science **347**, 1229 (2015)

[146] D. Witthaut, M. Werder, S. Mossmann and H. J. Korsch, *Bloch oscillations of Bose-Einstein condensates: Breakdown and revival*, Phys. Rev. E **71**, 036625 (2005)

[147] E. M. Graefe, *Stationary states of a PT symmetric two-mode Bose-Einstein condensate*, J. Phys. A: Math. Theor. **45**, 444015 (2012)

[148] W. D. Heiss, H. Cartarius, G. Wunner and J. Main, *Spectral singularities in $\mathcal{PT}$-symmetric Bose-Einstein condensates*, J. Phys. A: Math. Theor. **46**, 275307 (2013)

[149] D. Dast, D. Haag, H. Cartarius, J. Main and G. Wunner, *Eigenvalue structure of a Bose-Einstein condensate in a $\mathcal{PT}$-symmetric double well*, J. Phys. A: Math. Theor. **46**, 375301 (2013)

[150] A. Cavaglia, A. Fring and B. Bagchi, *$\mathcal{PT}$-symmetry breaking in complex nonlinear wave equations and their deformations*, J. Phys. A: Math. Theor. **44**, 325201 (2011)

[151] Z. H. Musslimani, K. G. Makris, R. El-Ganainy and D. N. Christodoulides, *Optical Solitons in $\mathcal{PT}$ Periodic Potentials*, Phys. Rev. Lett. **100**, 030402 (2008)

[152] H. Ramezani, T. Kottos, R. El-Ganainy and D. N. Christodoulides, *Unidirectional nonlinear $\mathcal{PT}$-symmetric optical structures*, Phys. Rev. A **82**, 043803 (2010)

[153] B. M. Breid, D. Witthaut and H. J. Korsch, *Bloch-Zener oscillations*, New J. Phys. **8**, 110 (2006)

[154] B. Wu and Q. Niu, *Superfluidity of Bose-Einstein condensate in an optical lattice: Landau-Zener tunnelling and dynamical instability*, New J. Phys. **5**, 104 (2003)

[155] D. Witthaut, F. Trimborn, V. Kegel and H. J. Korsch, *Quantum dynamics of Bose-Einstein condensates in tilted and driven bichromatic optical lattices*, Phys. Rev. A **83**, 013609 (2011)

[156] D. Dizdarevic, D. Dast, D. Haag, J. Main, H. Cartarius and G. Wunner, *Cusp bifurcation in the eigenvalue spectrum of $\mathcal{PT}$-symmetric Bose-Einstein condensates*, Phys. Rev. A **91**, 033636 (2015)

[157] I. S. Gradshteyn and I. M. Ryzhik, *Table of Integrals, Series, and Products*, Eighth Edition, Academic Press, (2014)